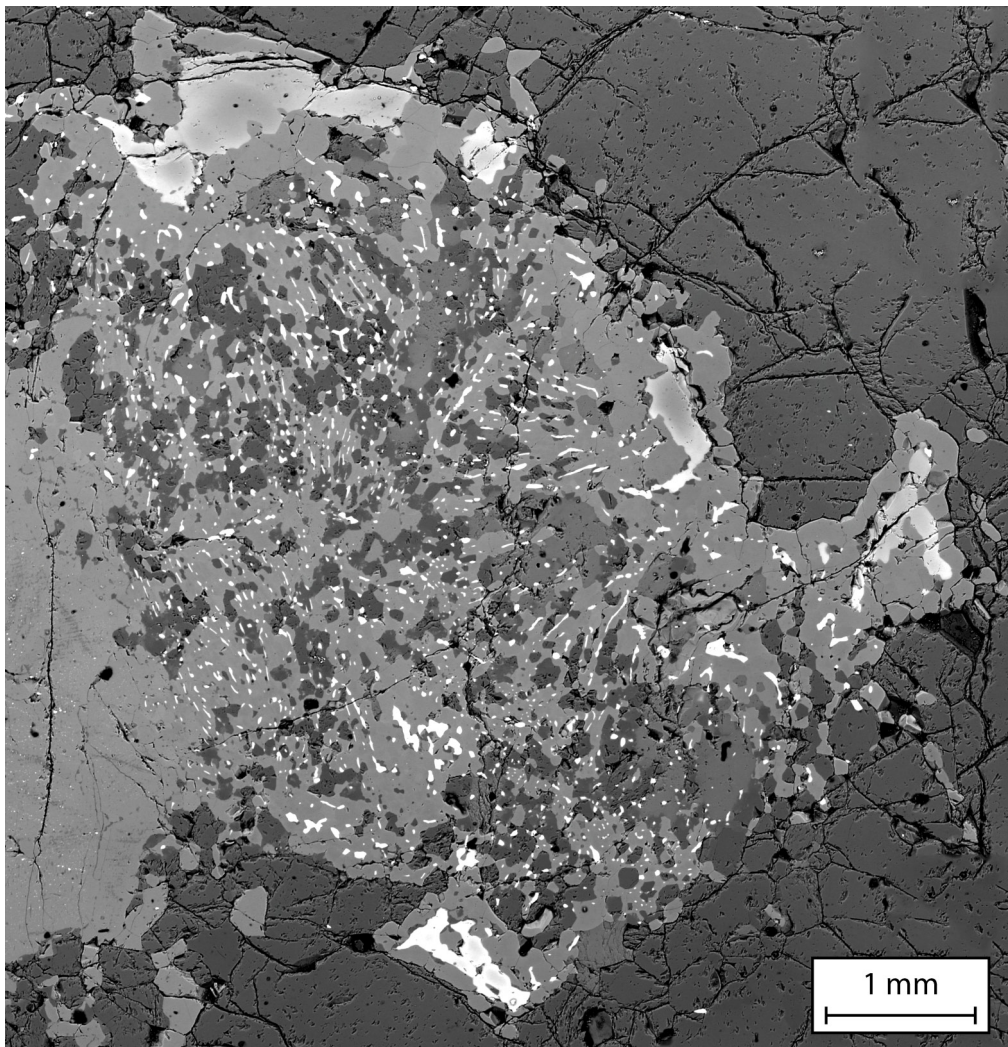




Universiteit Utrecht

THE FRININGEN GARNET PERIDOTITE (CENTRAL SCANDINAVIAN CALEDONIDES): A GOOD EXAMPLE OF THE CHARACTERISTIC MICROFABRIC AND P_{Tt} PATH OF A COLD MANTLE WEDGE GARNET PERIDOTITE



MSc student: Mattia Gilio
Supervisor: Dr. H.L.M. van Roermund

ABSTRACT

Orogenic peridotites from the Seve Nappe Complex (SNC), central Scandinavian Caledonides, were traditionally interpreted as fragments of sub-oceanic, Iapetus-related, lithosphere that became incorporated into the Scandian nappe pile during the Caledonian orogeny. The Friningen Garnet Peridotite (FGP) consists dominantly of dunite, garnet-bearing harzburgite and garnet lherzolite with minor internal eclogite- and/or garnet pyroxenite layers/dikes. The FGP shows evidence of an Archean to mid Proterozoic origin for the M1 mineral assemblage, including sulphides, as well as an early Caledonian age (~ 454 Ma) for the second mineral assemblage (M2) which is also characterised by a garnet-olivine HP mineral assemblage.

Pre-Caledonian HP-HT metamorphic conditions of 1200°C and $P \sim 2.0$ GPa are determined for the early M1a assemblage (ol+opx+cpx+grt). These physical conditions are followed by an inferred early Caledonian exhumation event down to 1050-1100°C and 1.5 GPa (M1b), followed by isobaric cooling down to 800°C (M1c). The latter is based on the break down of high-Cr M1a grt (uvt=6%) into opx+cpx+spl+parg symplectites (M1b) and the exsolution of garnet from Al-rich opx and cpx.

The early-Caledonian UHPM evidence (M2; $T=800^\circ\text{C}$ and $P=3.0$ GPa), discovered within an eclogitic dyke, is displayed in the FGP by low-Cr M2 grt (uvt=3%) replacing the M1b lower P symplectite assemblage and growth of M2 garnets around M1b spinels. Pl+di symplectites after omphacite in the internal eclogitic dyke and breakdown of kyanite to sapphirine and pl are indicative of isothermal decompression (M3a) down to 800°C and 1.0 GPa. This M3a phase has not been recognised in the mineral assemblage of the FGP, however, M2 mineral compositions of most grt₂, opx₂ and cpx₂ indicate a metamorphic overprint at $T=600^\circ\text{C}$ and $P=1.0$ GPa (M3b). An exception to this rule is formed by the Cr-content of M1a and M2 garnets.

The finding of the stable mineral assemblage dolomite+grt+ky+zoi±ph in the eclogitic dyke and of Sr-bearing carbonates in multiphase solid inclusions within M1a opx, cpx and ol indicates early (i.e. before crustal intrusion) metasomatism by slab-derived COH-bearing fluids.

Three olivine microstructures developed in response to different deformation events occurring at different PT conditions: Olivine M1 porphyroclasts were formed in the mantle at HT and low differential stress (1-3 MPa). The main mechanism involved was dislocation creep, producing a mixture of a- and b-type fabrics. These two fabrics are probably the result of two deformation phases, different in temperature and water content. Olivine M2 foam microstructure were formed during subduction, after crustal "intrusion" of the FGP. The main mechanism involved was dislocation creep, producing a-type fabrics. Olivine M3 foam microstructures were formed after strain localization along anastomosed shear zones at low T (650-700°C) and high differential stress (70-100 MPa). The main mechanism involved was grain size sensitive creep. However, dislocation creep was also involved producing a weak e-type olivine CPO.

The FGP can be interpreted as a mantle wedge garnet peridotite that originates from a cold and thick lithospheric mantle wedge, underneath either Laurentia or a micro-continent positioned between Baltica and Laurentia, that became incorporated into the subducting continental crust (SNC) during "early Caledonian" subduction (M2) down to UHPM conditions. In addition the M1a assemblage, including primary assemblages of the eclogitic dyke, are interpreted to be the result of Proterozoic (~1.5 Ga) refertilization of an Archean dunite body. Absolute timing of the M1b assemblage is uncertain but interpreted to be related to Iapetus formation. The multiphase solid-and fluid inclusions, present only in M1a-b mineral assemblages, are interpreted as evidence for an early Caledonian COH-bearing subduction zone fluid infiltration event. This newly documented PTt path of the FGP, except for the M2 subduction age, resembles that of cold mantle wedge garnet peridotites from the Western Gneiss Complex. As such the PTt path of the FGP gives important information about the role of the SNC during early Caledonian and Scandian collisions between Baltica and Laurentia.

INDEX	Page
1 - INTRODUCTION	1
2 - GEOLOGICAL SETTING	4
2.1 History of Baltica	4
2.2 The Scandinavian Caledonides	5
2.3 The Seve Nappe Complex	6
2.4 The Friningen Garnet Peridotite	8
2.5 Geodynamic model	9
2.6 Peridotite classification system	11
2.6.1 Lithospheric mantle	11
2.6.2 Classification of mantle peridotites	12
2.6.3 Mantle Wedge Garnet Peridotites (MWGP)	14
2.6.4 Mechanisms of emplacement	16
3 - METHODS	17
4 - FRININGEN GARNET PERIDOTITE	19
4.1 Lithologies	20
4.2 Structures	20
4.3 - Metamorphism	21
4.3.1 Garnet peridotite	21
4.3.2 Eclogite/garnet pyroxenite	26
4.3.3 Relationship between deformation and metamorphism indifferent lithologies	28
5 - MINERAL CHEMISTRY	30
5.1 Garnet/spinel peridotite	32
5.2 Eclogite	37
5.3 Geothermobarometry	39
5.3.1 The defocussed beam EMP mapping	39
5.3.2 Results	40
5.3.3 Discussion	45
5.4 Bulk rock chemical composition of the FGP	47
5.5 Pseudosection	48
7 - OLIVINE FABRIC ANALYSIS	50
6.1 Introduction	50
6.2 Olivine	51
6.3 Deformation-induced olivine microstructures	51
6.4 Dislocation substructures	54
6.4.1 Introduction	54
6.4.2 Optical observations	55
6.4.3 Discussion	56
6.5 Crystal preferred orientation (CPO)	57
6.5.1 Discussion	60
6.6 Paleopiezometry	61

	INDEX	v
7 - DISCUSSION		64
7.1 Protolith origin		64
7.2 Estimation of a PTt path		65
7.3 Slip systems and origin of water		68
7.4 Geodynamic interpretation		69
8 - CONCLUSION		72
9 - FUTURE WORKS		73
10 - ACKNOWLEDGMENTS		73
11 - REFERENCES		74
APPENDIX 1 - MINERAL CHEMISTRY		80
APPENDIX 2 - OLIVINE CPO		95

Cover: Backscattered electron micrograph of M1a garnet fully replaced by spinel + orthopyroxene + pargasite (M1b). Most of the M1b opx, as well as the rims of the large and zoned M1b spinels, is replaced by a second generation of garnet (M2). Grey scale refers to mass difference: from dark to light grey: pargasite, enstatite, garnet 2 and spinel. The surrounding phase is olivine. M1a orthopyroxene to the left of the picture, in contact with garnet 1 symplectite. (fig. 4.3)

1 - INTRODUCTION

The Scandinavian Caledonides are a deeply eroded Alpine-type orogenic belt that formed after the closure of the Iapetus Ocean and the collision between Baltica and Laurentia (400-430 Ma; Hartz & Torsvik, 2002; Roberts & Gee, 1985). Baltica underthrust Laurentia and the nappes were thrust to the East over the Baltoscandian basement and the autochthonous sedimentary cover. The Baltic shield, exposed within tectonic windows below the nappes, consists of high-grade gneiss and supracrustal rocks. In one of these complexes, the Western Gneiss Region (WGR), mantle derived orogenic peridotite bodies (Medaris & Carswell, 1990; Van Roermund & Drury, 1998; Spengler, 2006) and coesite and microdiamonds, indicating UHP (Van Roermund *et al.*, 2002), have been found locally within eclogite-facies rocks. The allochthons are divided into the lower, middle, upper and uppermost allochthons. The lower and the middle allochthon represent the precollisional continental margin of Baltica. The uppermost allochthon is composed of pre-Paleozoic thick carbonate complexes and crystalline basement interpreted to have Laurentian affinity. The upper allochthon consists of sedimentary and igneous rocks belonging to the Iapetus ocean, including ophiolites and island-arc complexes. The latter allochthon used to include, before a recent re-evaluation made by Gee *et al.* (2008), the Seve Nappe Complex (SNC) that, because of a greater lithological affinity, is now part of the middle allochthon. The SNC is composed of medium and high grade metapelites, metapsammites and amphibolites and is interpreted to be an ocean-continent transition zone (OCT) between Baltica and the Iapetus Ocean. It consists of a series of tectonic lenses (Ertsekey, Tjeliken, Vaimok and Tsäkkok lens) that underwent different types of metamorphism. Isolated ultramafic bodies of different dimensions (from km- to cm-scale), composition and metamorphic grade occur in every unit of the SNC. This study is mainly focused on one ultramafic body belonging to the Ertsekey lens. It is called the Friningen garnet peridotite body (Van Roermund & Bakker, 1983; Van Roermund, 1989; Verbaas & Van Roermund, 2012).

Early ideas sustained the passive character of the Caledonides (Gee, 1975). These models theorized the orogen to be formed by a series of nappes overthrust over a westward-dipping rigid basement. More recent observations on eclogites (Van Roermund, 1985) and peridotites (Brueckner & Van Roermund, 2007) brought to the formulation of a new model called *dunk tectonics* (Brueckner & Van Roermund, 2004). This model theorized that the subduction of the crustal slabs into the mantle is followed, in a relatively short period of time, by an exhumation due to buoyancy forces. The subduction of the silicic and less dense crustal terranes might be possible through the pull of the oceanic slab previously subducted into the oceanic lithosphere. The subduction continues until the negative buoyancy of the oceanic slab balances the positive buoyancy of the subducted continental crust. However, this pull should be sufficient to allow the more external terranes of the downgoing plate to reach, for a short period of time, UHP conditions in the subducted slab. Ultimately, in case of "slab break-off" (Von Blanckenburg & Davies, 1995), the negative buoyancy would cease and this would allow the previously subducted continental plate to move back towards the surface following approximately the same path (Ernst *et al.*, 1997). During the descent as well as the re-climbing, the friction between the subducted plate and the overlying lithospheric mantle wedge would allow to trap slices of garnet peridotite from the hanging wall (i.e. mantle) into the subducting crust. These mantle fragments would then ascend to the surface as part of the subducted plate. This type of garnet-bearing orogenic peridotite is called mantle-wedge garnet peridotite (Van Roermund, 2009a). However, since it has been

demonstrated that continental subduction in the Caledonides overtook the spinel-garnet phase transition it is possible to infer that garnet peridotite could have been formed also through prograde metamorphism of lower pressure protoliths (serpentinites and plagioclase/spinel peridotites). This latter type of peridotite is called subduction-zone peridotite (Van Roermund, 2009a; 2009b). This new classification replaces older terminology such as Alpine-type, Root-Zone peridotites or Relic type (Brueckner & Medaris, 2000), alternatively it is re-equilibrated to garnet-bearing peridotite.

Orogenic peridotites from the Seve Nappe Complex (SNC), central Scandinavian Caledonides, were traditionally interpreted as fragments of sub-oceanic, Iapetus-related, lithosphere that became incorporated into the Scandian nappe pile during the Caledonian orogeny (Zwart 1974; Qvale & Stigh, 1985). This interpretation was first challenged by Van Roermund (1989) who described for the first time the occurrence and petrogenesis of garnet-bearing peridotites from an area around lake Friningen, northern Jämtland, central Sweden.

The Friningen garnet peridotite is 30x300m wide and is the largest garnet peridotite body exposed in the area around Lake Friningen (Du Rietz, 1935). This body was first described in detail by Van Roermund (1989) but recently, UHP metamorphic conditions have been demonstrated for the mineral assemblage that occur exclusively within mafic dikes of the FGP (Janàk *et al.*, 2013; Gee *et al.*, 2013). These UHP metamorphic conditions have been interpreted to be due to Caledonian collisions (late Ordovician) related to prograde subduction of the Baltoscandian margin deep into the coesite stability field (3.0 GPa/800 °C). Within this FGP body, three main microstructures have been recognized (Verbaas & Van Roermund, 2012). According to early PT estimations, Pre-Caledonian lithosphere conditions are represented by a coarse grained ol+grt+opx±cpx mineral assemblage that was formed around 1.5 GPa/750- 800 °C (Verbaas & Van Roermund, 2012). This assemblage has been called the M1 assemblage (Van Roermund, 1989; Verbaas & Van Roermund, 2012). During the late Ordovician, the M1 assemblage of the FGP has been overprinted by a second (called M2; Van Roermund, 1989; Verbaas & Van Roermund, 2012), much finer grained, garnet-olivine assemblage. The M2 assemblage is defined by a characteristic (annealed) olivine microstructure containing well defined strain-free grains with straight (olivine) grain boundaries meeting at triple point junctions. This olivine microstructure resembles the olivine foam texture of Calon (1979). However, in the Friningen garnet peridotite it can clearly be demonstrated that the M2 olivine foam was formed during prograde subduction into the coesite facies field in contrast to the retrograde metamorphic conditions developed during exhumation/exhumation as proposed by Calon (1979).

A third olivine microstructure (M3) (the olivine mortar texture) was described by Calon (1979) in the Kittelfjäll Spinel Peridotite body (KSP). This latter microstructure has not been recognized within the Friningen garnet peridotite. However, a late, fine grained, M3 olivine "foam" microstructure is present within D3 shear zones, as described by Van Roermund (1989).

Upper mantle olivine grains are commonly characterized by a strong crystallographic preferred orientation (CPO). This CPO is believed to be the result of solid-state convective motion in the sub-continental lithospheric and/or asthenospheric mantle. These motions induce different creep mechanisms believed to be the cause of the rotation of the crystallographic axes according to the mantle flow directions. The iso-orientation of the a-axis in olivine crystals within the lithospheric mantle can be seismically detected because of the greater velocities of seismic waves along this axis with respect to b- and c-axes. Early

works (Carter & Avé Lallement, 1970; Avé Lallemant & Carter, 1970; Poirier, 1975) believed that dislocation creep was the main mechanism that controls the orientation of olivine crystals (Raterron *et al.*, 2007) and that the a-axis of olivine is always disposed parallel to the flow direction. More recent works (Jung & Karato, 2001; Katayama *et al.*, 2004; Katayama & Karato, 2006) demonstrate that the a-axis orientation is also influenced by the water contents as well as many other mechanisms like nucleation, sub-grain rotation re-crystallization and grain boundary migration (GBM). These mechanisms can, in fact, significantly modify the CPO, by strengthening, weakening or changing the symmetry of the dominant slip system(s) with respect to the imposed shear (Karato, 1988; Zhang & Karato, 1995; Bystricky *et al.*, 2000). Thus, the final CPO of olivine depends primarily on factors such as temperature, deviatoric stress and presence of fluid (Jung & Karato, 2001; Jung *et al.*, 2006; Raterron *et al.*, 2007).

In all studies of the FGP reported above, the metamorphic conditions with the pre-Caledonian lithospheric mantle have never been constrained adequately. This MSc thesis is constrained to the study of the early M1a-b and M2 assemblages, both from a petrological and micro-structural point of view. First of all, metamorphic conditions and a new PTt path for the early M1-M2 assemblages of the FGP have been produced with the aid of both geothermobarometry and thermodynamic calculations (pseudosections). Secondly, a detailed study of the crystallographic fabrics (CPO) and related deformation mechanisms that produced the olivine foam (M2) and mortar (M3) microstructures, within the Friningen garnet peridotite has been carried out. In particular olivine CPO is measured in order to find out what kind of olivine deformation mechanisms were involved in the formation of the coesite stable UHP olivine foam fabric. In addition, the staining method of Kohlstedt *et al.* (1976) is used to obtain information about the dislocation substructure present within M1 olivine porphyroclasts and M2 olivine grains. Furthermore, results from both petrologic and microstructural investigations have been combined in order to produce a PTt-d diagram

2 - GEOLOGICAL SETTING

2.1 History of Baltica

Baltica is here defined as a craton that existed during the geological time period between the break-up of Rhodinia and the assembly of Pangea (800-400 Ma). During the late Precambrian, Baltica consisted of three major terranes: Fennoscandia to the North, Sarmatia to the South and Volgo-Uralia to the East. These terranes joined together during the Svecofennian Orogeny (1.9 Ga) to form a larger terrane called Protobaltica (Bogdanova *et al.*, 2001). Protobaltica consolidated at about 1.1-1.0 Ga with Laurentia, Siberia, NW Africa and Amazonia to form the supercontinent Rhodinia (Meert & Torsvik, 2003). Torsvik (2003) dated the break-up of Rhodinia at about 800-750 Ma. This rifting event started the formation of a series of terranes (Laurentia-Protobaltica to the East and Australia and East Antarctica to the West) separated by spreading oceans. The separation of South America from Laurentia is related to an early opening of the Iapetus Ocean at about 580 Ma (Hartz & Torsvik, 2002). At ~570 Ma this rift migrated northwards and Baltica started to separate from Laurentia, at ~550 Ma Baltica became independent. At about the same time (mid-late Vendian), the northern part of Baltica (according to the geographical coordinates at that time; Fig. 2.1) switched from an extensional tectonic regime to an active margin. During the Late Silurian-Early Devonian (430-400 Ma) the Iapetus Ocean finally closed and Baltica was sutured with

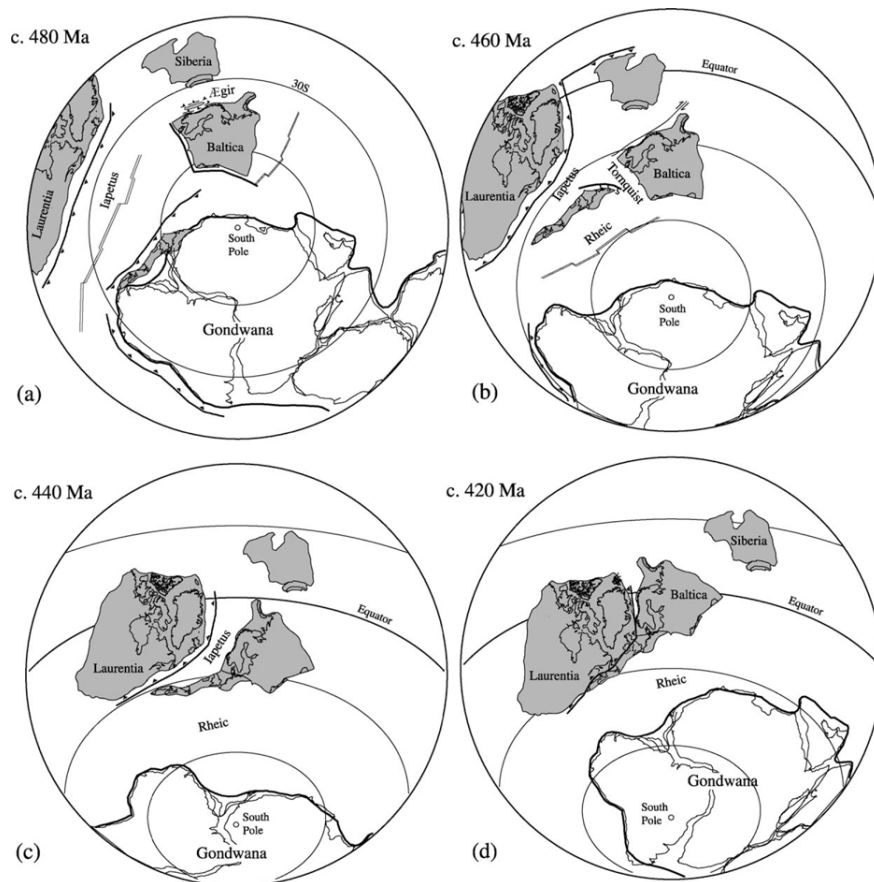


Fig. 2.1 - Simplified palaeomagnetic reconstructions from Early Ordovician to Late Silurian time (modified after Roberts, 2003)

Laurentia and Avalonia to form the continent Laurussia. This resulted in the formation of the Caledonian mountain chain. At about 270 Ma almost all large terranes were sutured together again to form the supercontinent Pangea. A simplified model of the plate movements during the Caledonian orogeny is shown in Fig. 2.1 (Roberts, 2003). After the break-up of Pangea during the Mesozoic, the Caledonides became fragmented into the Appalachians in North America, the Greenland Caledonides, the British Caledonides in Scotland and the Scandinavian Caledonides in Norway and Sweden.

2.2 The Scandinavian Caledonides

The Scandinavian Caledonides (SC) are a 2000 km long, deeply eroded remnant of an ancient mountain belt formed during the early-middle Paleozoic (Fig. 2.2). They consist of a series of nappes thrust onto Baltica (Gee *et al.*, 2008) in between 500 and 400 Ma after multiple compressional (HP and UHP) and extensional events (Brueckner & Van Roermund, 2004). The Baltic Shield was formed after several crustal accretion phases during Precambrian times (>3.1-1.5 Ma; Gorbatshev, 1985). It is exposed in tectonic windows below the allochthons and consists of high-grade gneisses and supra-crustal rocks. Although most of these rocks give Precambrian crystallization ages, some, especially in the western part of the orogen, shows a strong Caledonian overprint. They represent the external part of the basement involved in the Caledonian orogenic event (Bryhni & Grimstad, 1970; Brueckner, 1972). One of these "Caledonized" complexes is the Western Gneiss Region (WGR). The WGR is the largest exposure of parautochthonous basement of the SC. It records a Scandian (430-390 Ma) overprint in amphibolite, granulite and eclogite facies over Proterozoic igneous and metamorphic rocks. Several lenses of HP and UHP eclogite and garnet peridotite occur at different levels of the tectono-stratigraphy. Furthermore, recently discovered majoritic garnet (Van Roermund & Drury, 1998) and micro-diamonds of Scandian age (Dobrzhinetskaya *et al.*, 1995; Van Roermund *et al.*, 2002; Vrijmoed *et al.*, 2006) indicate a very deep subduction (>200 km) of the WGR (Spengler *et al.*, 2009). The WGR mainly shows three age clusters. Older ages (about 1.5 Ga) represent an older metamorphic event related to the formation of Baltica (Krogh *et al.*, 2003). Plutonic intrusions and dike swarms, record a thermal anomaly dated around 1.0 Ga (Robinson, 2003). Late ages, between 450-400 Ma, represent the Scandian metamorphic overprint (Spengler 2006; Van Roermund, 2009a).

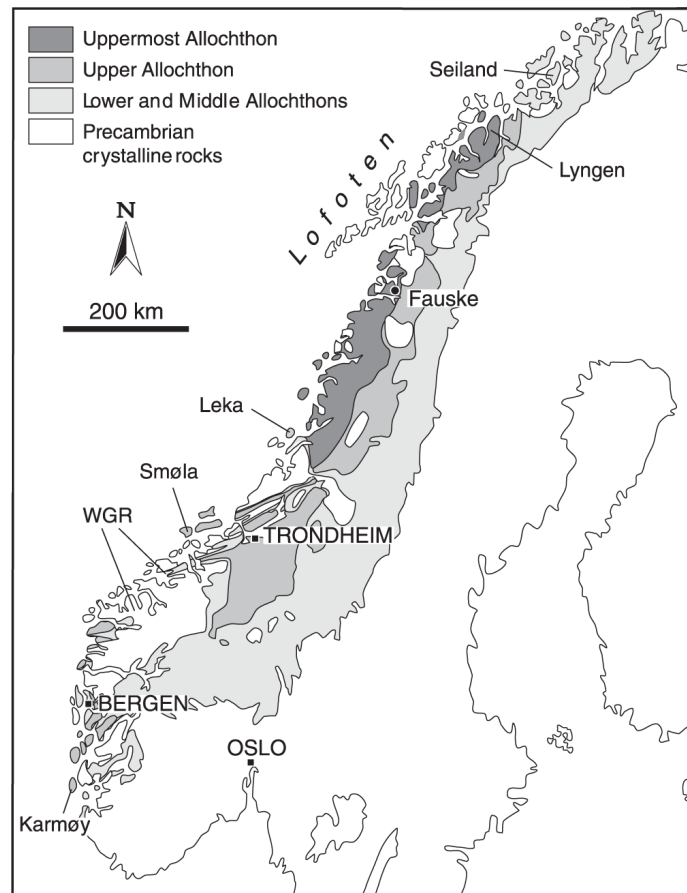


Fig. 2.2 - Simplified tectonostratigraphical subdivisions of the Scandinavian Caledonides (modified after Roberts, 2003).

The nappes stacked over Baltica are usually subdivided into: Lower, Middle, Upper and Uppermost Allochthon (Roberts & Gee, 1985; Gee *et al.*, 2008).

- The **Lower Allochthon** represent the thrust and deformed precollisional margin of Baltica (Gee *et al.*, 2008; 2013). They consist of slices of basement with their sedimentary cover. Metamorphic grade increase to the west from lower to high greenschist facies (Roberts & Gee, 1985).
- The **Middle Allochthon** consists of sheets of basement and Late Proterozoic sandstone. Two metamorphic gradients have been found in this Allochthon. One gradient ranges, from the lower to the upper part of the nappes, from greenschist to amphibolite, granulite and locally eclogite facies. The second gradient is characterised by a westward increase of metamorphic grade from lower greenschist facies near the border between Norway and Sweden to amphibolite facies in the hinterland (Bryhni & Andréasson, 1985; Roberts & Gee, 1985).
- The **Upper Allochthon** (in Sweden) was originally divided into Seve and Köli nappes. Due to their discrepancy, the Seve nappes in Sweden were recently relocated into the middle allochthon (Gee *et al.*, 2008; 2013). The Köli nappes consists of igneous rocks and sedimentary covers that belong to the lapetus Ocean, including island arcs and ophiolites (Stephens, 1988). They show a metamorphic overprint in greenschist-facies (Roberts & Gee, 1985).
- The **Uppermost Allochthon** is interpreted to be the remnants of the Laurentian precollisional margin (Stephens & Gee, 1985; Roberts *et al.*, 2001; Gee *et al.*, 2008). It mainly consists of high grade metasediments, migmatitic paragneisses, marbles and ophiolites (Roberts & Gee, 1985).

2.3 The Seve Nappe Complex

The 800-km-long Seve Nappe Complex (SNC) belongs to the upper part of the Middle Allochthon and it is directly overlain to the west by the Köli nappes (Zarichsonn, 1973; Gee *et al.*, 2013). It consists of thrust sheets of heterogeneous lithological composition and different metamorphic histories. In Northern Jämtland area (Fig. 2.3), it overlies the low-grade Särvi nappe of the Upper Allochthon and is divided in three main belts (from top to bottom, the western, central and eastern belt; Zwart, 1974) on the base of different lithologies and metamorphic gradient. These belts are now upgraded by the Swedish Geological Survey (SGU) in upper, middle and lower Seve Nappe (Janàk *et al.*, 2013; Gee *et al.*, 2013).

- The **upper Seve Nappe (western belt)** consists of garnet bearing quartz-micaschists (the Svärtsjöbacken schist) with local lenses of amphibolite and/or serpentinite.
- The **middle Seve Nappe (central belt)** is formed by several lenses divided by tectonic contacts consisting of kyanite-sillimanite gneiss, quartz-feldspar gneiss and amphibolite. In one of these lenses, the Ertsekey lens, eclogites have been found with a metamorphic peak of 1.8-2.4 GPa - 780°C (Van Roermund & Bakker, 1983; van Roermund, 1985; 1989). Despite all rock units (especially pelitic gneisses) show various degrees of partial melting, the original foliation is generally still preserved (Van Roermund & Bakker, 1983). Several

foliated, lens-shaped ultramaphic bodies occur, usually, at the contact between the various rock units (Bucher, 1991).

- The **lower Seve Nappe (Eastern Belt)** consists of garnet bearing micaschist, kyanite-staurolite bearing schist, quartzo-feldspathic gneiss, amphibolite, quartzite and garnet-biotite rocks. These rocks do not show any evidence of partial melting. Eclogites, found within the Tjeliken lens (Van Roermund, 1985; 1989), show a metamorphic peak of 3.0 GPa - 800°C (Janàk *et al.*, 2013). Ultramafic bodies were found near tectonic contacts between the various lenses.

The Seve Nappe Complex shows an inverted metamorphic grade, with granulite to eclogite facies in the Central Belt and low/middle amphibolite facies in the adjacent Eastern and Western Belts. The metamorphic pressure of the Central Belt differs parallel to the axis of the Caledonian orogen (Van Roermund & Bakker, 1983; Hogerwerf, 2010; Gademan, 2011). The highest pressures are in the Avarö gneiss > 1.8 , medium pressures are found in the Marsfjället gneiss 1.25-1.8 GPa and the lowest pressures occur in the Lillfjället gneiss < 1.25 GPa (Fig. 2.3).

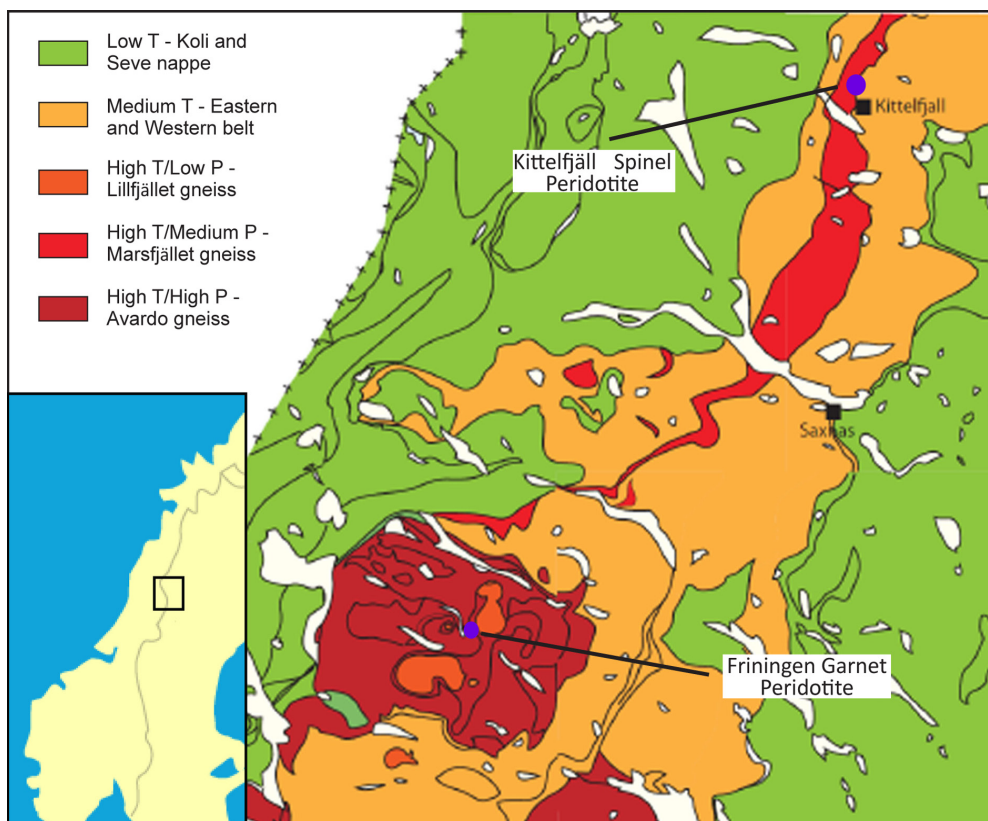


Fig. 2.3 - Geological map of the Seve-Köli Nappe Complex in N Jämtland-S Västerbotten, central Sweden. The Central/Middle Seve Belt is illustrated in various shades of red illustrating the inferred pressure gradient described in the text. (Zwart, 1974; Williams & Zwart, 1977; Van Roermund & Bakker, 1983; Van Roermund, 1985; 1989)

Several studies have attempted to date the peak metamorphism in the SNC, including gneisses, eclogites and ultramafic bodies (Tab. 2.1). Early Sm-Nd ages by Mørk *et al.* (1988) from the Tsäkkok and the Vaimok lens in the North of the SNC gave results of 505 ± 18 Ma and 503 ± 14 Ma respectively. More recent studies by Root & Corfù (2012) gave, for the same lenses, zircon ages of 482 ± 1 Ma for the Tsäkkok lens and 483 ± 1 Ma for the Vaimok lens. Furthermore, Root & Corfù (2012) interpreted an U-Pb age of 602 ± 2 Ma within a metagabbro as the age of an early igneous event (i.e. related to the formation of the Iapetus Ocean). Monazite ages found by Hogerwerf (2010) and Gademan (2011) gave concordant age of 497.9 ± 20 Ma, 502 ± 20 Ma and 491.2 ± 22 Ma for the Lillfjället gneiss, Avardo gneiss and Svartsjöbäcken schist respectively. The southern part of the SNC, in N-Jämtland, shows much younger metamorphic peak ages with respect to the northern part of the complex. Brueckner *et al.* (2004) found ages of 452.1 ± 7.5 Ma, 448 ± 13 Ma and 451 ± 43 Ma (Sm-Nd in grt and opx) from three garnet pyroxenites belonging to the Friningen garnet peridotite. Concordant U-Pb zircon ages (446 ± 1 Ma) were found in the eclogites from the Tjeliken lens (Root & Corfù, 2012). The relation between these two age clusters (Cambrian in the North and Upper Ordovician in the South) has not been found yet. Furthermore, these ages are generally older than the main Scandian phase (420-400 Ma), recorded in the (U)HP units of the WGR (Carswell *et al.*, 2003; Krogh *et al.*, 2011). The debate about the origin of these two age clusters and the younger peak ages in the WGR (Brueckner & Van Roermund, 2007; Root & Corfù, 2012) is beyond the aim of this thesis.

Tab. 2.1. Constrained Early Caledonian ages of the metamorphic peaks in different lithologies and localities of the SNC.

Technique	Age	Lithology	Locality	Reference
Sm-Nd	505 ± 18 Ma	Eclogite	Tsäkkok lens	Mørk <i>et al.</i> (1988)
Sm-Nd	503 ± 14 Ma	Eclogite	Vaimok lens	Mørk <i>et al.</i> (1988)
Sm-Nd	452.1 ± 7.5 Ma	Garnet pyroxenite	Friningen	Brueckner <i>et al.</i> (2004)
Sm-Nd	448 ± 13 Ma	Garnet pyroxenite	Friningen	Brueckner <i>et al.</i> (2004)
Sm-Nd	451 ± 43 Ma	Garnet pyroxenite	Friningen	Brueckner <i>et al.</i> (2004)
Th/U-Pb	497.9 ± 20 Ma	Monazite	Lillfjället gneiss	Gademan (2011)
Th/U-Pb	502 ± 20 Ma	Monazite	Avardo gneiss	Gademan (2011)
Th/U-Pb	491.2 ± 22 Ma	Monazite	Svartsjöbäcken schist	Gademan (2011)
U-Pb	482 ± 1 Ma	Eclogite	Tsäkkok lens	Root&Corfu (2012)
U-Pb	483 ± 1 Ma	Eclogite	Vaimok lens	Root&Corfu (2012)
U-Pb	602 ± 2 Ma	Metagabbro	Vaimok lens	Root&Corfu (2012)
U-Pb	446 ± 1 Ma	Eclogite	Tjeliken Lens	Root&Corfu (2012)

2.4 The Friningen Garnet Peridotite

The Friningen Garnet Peridotite (FGP) occurs in the Ertsekey Lens of the Central Belt (Fig.2.3). The size of the FGP is 200m x 30m. This ultramafic body is found at the structural base of the eclogite-bearing migmatitic ky-sil-Kfs gneiss (Ertsekey lens) near Lake Friningen. This body, first described by Van Roermund (1989), consists of layers of different compositions (poor-Al dunites, garnet harzburgites, garnet lherzolite) locally intercalated with eclogitic and/or garnet pyroxenite layers.

The older mineral assemblage (M1a) of the peridotite consists of coarse-grained $ol \pm opx \pm cpx \pm grt$ (\pm sulfides of Archean age). The M1a garnet usually breaks down into $cpx/am + opx + spl$ (M1b). A second assemblage (M2) consists of $ol(2) \pm opx(2) \pm cpx/am(2) \pm grt(2) \pm spl(2)$. Preliminary PT estimates indicate that the M1a assemblage was formed

at 2.3 GPa - 840°C and the M1b around 1.8 GPa - 840°C (Verbaas & Van Roermund, 2012). PT estimates of the M2 assemblage was not precisely determined; however, Janàk *et al.* (2013) found UHP (3.0 GPa – 800°C) for the M2 assemblage of an eclogitic dike hosted by the FGP.

The main foliation (S1) of the garnet peridotite is defined by the relative modal variation of the main minerals (ol±opx±cpx±gr). This results in a compositional layering of Al-poor dunite and garnet bearing dunite, harzburgite, lherzolite and pyroxenite. However, this compositional layering (S1) is hard to detect in the field since the chemical variations are progressive in nature rather than sharp. In most cases, the S1 foliation is defined by the iso-orientation of coarse-grained (≤ 2 cm), stretched and heavily deformed porphyroclasts of M1 grt, opx, cpx and ol. The eclogitic dyke and the pyroxenite layers are generally parallel to S1. The eclogitic dyke is folded in tight to isoclinal folds and a second, very pervasive foliation (S2) is found along the axial plane of these folds. The S2 foliation is generally subparallel with S1 but, locally, an angle with S1 of about 30° is observed.

In the FGP, three age clusters have been reported by Brueckner *et al.*, (2004). Re-Os analyses on sulfide (Pentlandite) gave Archean ages. This age is related to multiple events of partial melting and Archean mantle depletion. Sm-Nd clinopyroxene model ages from the garnet peridotite and the eclogitic dyke gave Proterozoic ages (1.1 - 1.2 Ga). This age indicate that at least one refertilization event, coupled to the intrusion of a dyke swarm, occurred during the Proterozoic. Furthermore, Sm-Nd mineral ages (cpx, grt) are 452.1 ± 7.5 , 448 ± 13 and 451 ± 43 Ma (Early-Proterozoic; Brueckner *et al.*, 2004; Brueckner & Van Roermund, 2007).

The aim of the present MSc thesis is to re-estimate the pre-Caledonian PTt path prior to the UHP event (M2), with special attention to the role of deformation along this path.

2.5 Geodynamic model

The Caledonian orogeny was the result of a long and complex history including multiple phases of plate collisions. According to the model by Brueckner & Van Roermund (2004), the orogen was formed in three main phases (Finnmarkian, Jämtlandian and Scandian), representing three separated (U)HP events (Fig. 2.4).

1. **Finnmarkian phase** (480-500 Ma): it involves the accretion of an island arc in the Ægir sea (the Virisen arc) onto the northern Baltoscandian margin (Seve and Kalac NC) with the emplacement of mantle peridotite of oceanic affinity from the Virisen mantle wedge (Spengler, 2006). The resulting terrane is termed Virisen-Norbotten-Composite-Terrane (VNCT).
2. **Jämtlandian phase** (~450 Ma): the SNC in northern Jämtland/southern Västerbotten subducted below the VNCT. This phase resulted in the emplacement of mantle wedge peridotites and in the strong metamorphic overprint in eclogitic facies (Brueckner *et al.*, 2004).
3. **Scandian phase** (420-400 Ma): this final phase represents the final collision between Baltica and Laurentia, resulting in the very deep subduction (>150 km) of the external border of Baltica (Spengler, 2006). Furthermore, Early Caledonian nappes were transported eastward (Gee *et al.*, 2013)

The late- and post-Scandian phase is characterised by orogenic collapse. During this phase, the nappes in Sweden were transported further east resulting in the current geometry.

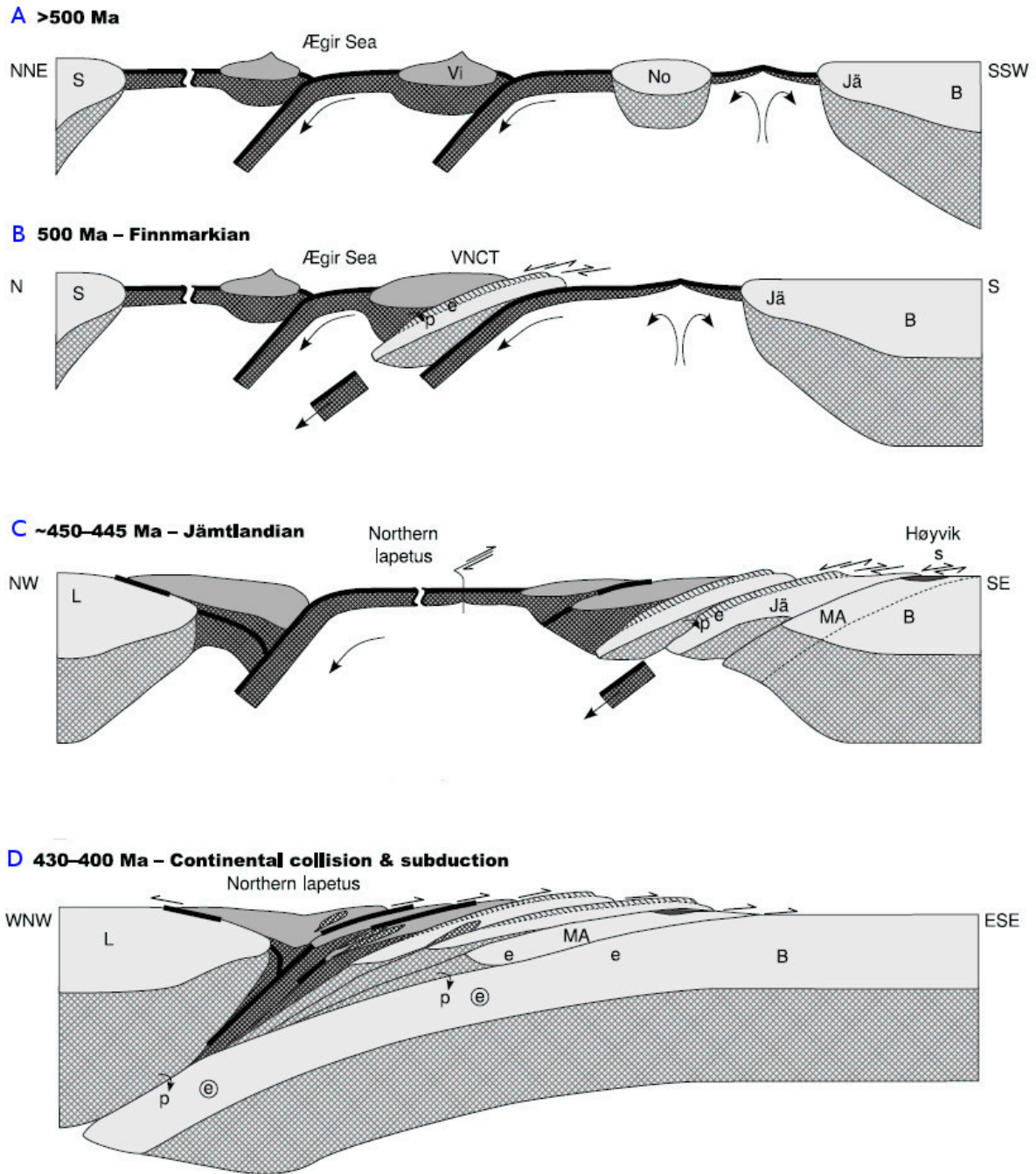


Fig. 2.4 - Simplified cartoon showing a proposed model for the evolution of the Northern Caledonides. A) Initial plate configuration. Baltica and Laurentia are far apart, separated by multiple configuration of spreading oceans and compressive oceanic arcs. Micro-continents (like Norbotten "No") are located in between the two major plates. B) The No micro-continent subducts under an oceanic arc (Virisen). The following eduction resulted in the NVCT. C) The continental margin of Baltica, moving towards Laurentia, subduct underneath the VNCT and island arcs in between. This phase is dated 465 Ma and it is related to the emplacement of the mantle wedge peridotites (among which the FGP) and to the eclogite facies metamorphism (3.0 GPa, 800°C; Janàk *et al.*, 2013) D) Continental collision between Baltica and Laurentia. The burying of Baltica at exceptional depth (> 150 km) is witnessed by the several UHP terranes in the WGR. Abbreviations: Laurentia (L), Baltica (B), Siberia (S), Virisen arc (Vi), Norrbotten micro-continent (No), Jämtland continental margin (Ja), Middle allochthon (Ma), sediment (s), peridotite (p), HP eclogite (e), UHP eclogites (circled e) (after Spengler, 2006).

2.6 Peridotite classification system

2.6.1 Lithospheric mantle

The great majority of information about the composition of the upper mantle is derived from xenoliths and mantle fragments found within crustal terranes. The lithosphere is formed as a consequence of geochemical differentiation driven by partial melting. Lighter elements (K, Na, Ca, Al, Si, etc.) have greater affinity with silicate melts and accumulated in the crust. The lithospheric part of the Upper Mantle and the Asthenosphere can therefore be highly depleted in those elements and mainly consists of refractory elements (Mg, Cr). Therefore, the most common phases in the Upper Mantle are, in order of relative amount, olivine, orthopyroxene, clinopyroxene and an Al-bearing phase which changes with decreasing pressure from garnet to spinel to plagioclase (Fig. 2.5).

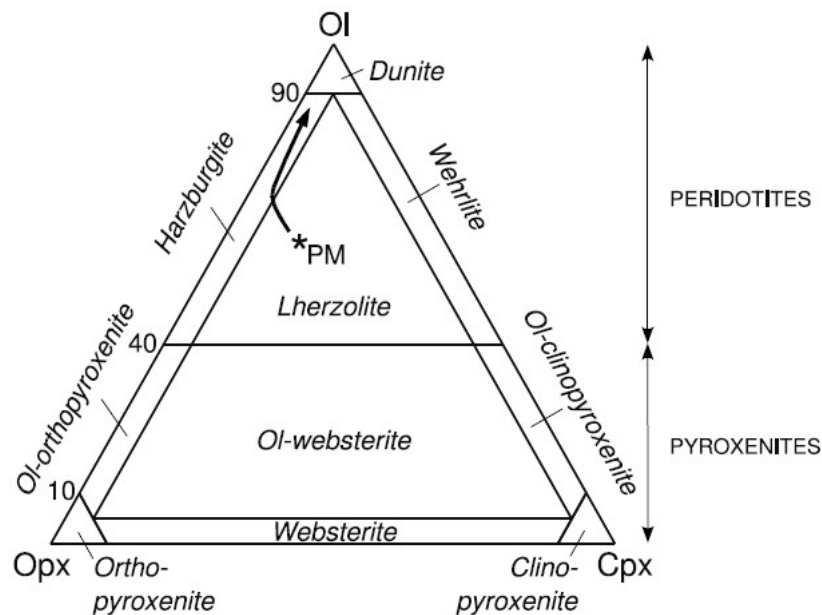


Fig. 2.5 - Classification of ultramafic rocks based on mineral modes (ol-opx-cpx). The black line indicates the usual depletion trend during increasing amounts of partial melting. An original (fertile) ultramafic rock of lherzolitic composition (i.e. primitive mantle; PM) is firstly depleted in its cpx component and then by its opx component, leaving the more refractory dunite as restite.

The lithospheric part of the upper mantle (i.e. the asthenosphere cooled down below ~ 1200°C) can be subdivided, according to this genesis, in sub-oceanic (SOLM) and old and young sub-continental (lithospheric) mantle (SCLM). SOLM occurs below oceanic crust and is related to the young age of partial melting, producing the oceanic crust. In contrast, (old) SCLM occurs below continents and can be related to Archean (up to 3.8 Ga) episodes of partial melting. This Archean SCLM represents the ultra-depleted, refractory residue after several melting events, related to the early extraction of komatitic melts ($T > 1800^{\circ}\text{C}$; $P = 3-7$ GPa). The degree of partial melting related to these conditions is very high ($>40\%$; Herzberg, 2004). This implies very high heat flow in the mantle in Archean times (Walter, 1998). The progressive decrease of heat flow with time in the Earth mantle brought to different and less pronounced depletion trends during Proterozoic and Phanerozoic. This gradual cooling of the Earth's Upper Mantle resulted in less depleted younger SCLM. The melt extraction

volume is believed to have decreased from 30% during Proterozoic to 10-20% in recent times (Walter, 1998).

As a consequence of ocean spreading, hot asthenosphere rises underneath Mid Oceanic Ridges forming SOLM. This isothermal adiabatic upwelling results in partial melting and the most refractory part (usually dunite) forms the lithospheric mantle. For its close relation to ocean spreading, the age of SOLM cannot be older than 200 Ma prior to the orogenic collision event (Condie, 1997). In contrast, SCLM fragments may have formed by processes completely unrelated to Mid Oceanic Ridges and can be up to 2.0-3.0 Ga older than the age for their crustal emplacement.

2.6.2 Classification of mantle peridotites

An early attempt to classify from a geodynamic point of view the ultramafic bodies throughout the world was carried out by Den Tex (1969). He subdivided peridotites into two main classes: (1) "non-orogenic" or "stratiform" type (i.e. Cumulate peridotite formed at the base of layered gabbroic complexes like Skaergaard, Bushveld or Stillwater) and (2) "Orogenic" or "Alpine type" (i.e. Peridotites exposed within mountain belts whose emplacement into the continental crust was related to tectonic processes). This last type was further divided into (a) "Ophiolitic" or "Alpine type s.s." (i.e. Peridotites of oceanic origin associated with pillow lavas and usually enclosed within low grade or non-metamorphic complexes) and (b) "root-zone" (i.e. occurring as tectonic lenses within high grade metamorphic rocks).

With the fast development of plate tectonic theory and with the discovery of UHP metamorphism (Chopin, 1984), this classification system, based on the paragenesis of the peridotite and its host rock was not sufficient anymore. In particular, the crust emplacement of root zone peridotites (including garnet and/or spinel peridotites) could no longer be explained.

The emplacement mechanism of mantle-derived peridotites into continental crust has been described traditionally by deep-level ductile imbrication of the lower part of the continental crust (Cuthbert & Carswell, 1990; Medaris & Carswell, 1990). Though, this mechanism can explain the crustal "intrusion" of mantle-derived spinel peridotites, it cannot explain how garnet peridotites "intruded" into the continental crust. This is due to the presence of a thick (~15 km) layer of spinel-bearing peridotite at the bottom of the continental crust. Garnet-bearing peridotite bodies are widely found within (U)HP metamorphic terrains throughout the world. These bodies outcrop as lensoid masses with sizes ranging from a few cm² to several km². They may carry structures, composition and PT evolutions concordant with the host rock but discordant bodies are also widely found. The peridotites are interpreted to be the highly refractory restite (locally refertilized) after the extraction of basaltic melts (in some cases even komatitic/picritic melts; Brueckner & Medaris, 1998). Eclogite and pyroxenite dikes are sometimes found within garnet-bearing peridotite and are interpreted to be related to intrusions that occurred while the peridotite was still deep in the lithospheric mantle.

Brueckner & Medaris (2000) divided orogenic peridotites into "crustal", if they resided in the shallow crust as cumulates or serpentinites before subduction, and "mantle-type", if they intruded from the mantle into the continental crust. "Mantle" peridotites are further divided into "subduction zone peridotite", i.e. they come from the oceanic subduction zone and "relic" if they come from an old subcontinental lithosphere. "Subduction zone peridotites"

are divided into three sub-categories: “prograde type”, “HP-HT type” and “UHT-type”. The “prograde subduction zone peridotites” are incorporated as serpentinites, spinel or plagioclase peridotites into the downgoing plate at shallow to intermediate depths (20-50 km). These bodies would then follow the subducting host rock and they would contain, up to a certain extent, a subduction fabric overprint. Sm-Nd cpx-grt mineral ages would be the same as in the eclogites included in to subducting continental crust.

“HP-HT subduction zone peridotites” intruded in the crustal slab at deeper levels (>50 km) already contained (U)HT stable garnet assemblages at the moment of “intrusion”. In this case the age of the garnet-olivine-bearing assemblage could also be different (older) from the age of the eclogites in the host rock, but not more than 250 Ma (cooling age).

“(U)HT type subduction peridotite” formed from a high temperature spinel peridotite. In this case, garnet may grow by cooling during mantle upwelling.

The “relict peridotites” are interpreted to intrude in the crustal slab away from the mantle wedge. They probably come from the cold, ancient and static mantle below the continental shield. In this case, the age of the older assemblage is much older than the subduction event and could be related to the partial melting processes involving the early formation of the continental crust. This classification system is summarised in Tab. 2.2.

Tab. 2.2. Garnet peridotite classification system (modified after Brueckner & Medaris, 2000)

CRUSTAL PERIDOTITE		Present in crust prior to subduction of crust.	
MANTLE PERIDOTITE “Intrudes” laterally or downward either through crustal imbrication or from mantle wedge into underthrust continental crust during subduction.	Subduction zone peridotite Mantle wedge existed above oceanic subduction zone prior to subduction of continental crust.	Prograde type	Intrudes from wedge at shallow to intermediate depths (20–50 km) and acquires garnet-bearing assemblages through prograde metamorphism of LP protoliths (serpentinites, spinel peridotites, plagioclase peridotites) as host crustal terrane continues to subduct.
		UP–HT type	Intrudes from mantle wedge at deep levels (>50 km) and contains mantle garnet-bearing assemblages at time of intrusion.
		UHT-type	Spinel to garnet transition occurs at high temperature (c. 1200 °C), possibly during upwelling of asthenosphere.
	Relict peridotite	Mantle wedge composed of old subcontinental lithosphere. Garnet-bearing assemblages form well before subduction of continental crust.	

The work of Brueckner & Medaris (2000) represents a first attempt to classify geodynamically garnet peridotites. Above all, the age of the older garnet-olivine assemblage with respect to the collision age and the presence/absence of subduction-zone metasomatism are the main criteria used to infer the origin of the protolith. It turns out that only these criteria are not enough to infer the origin and the geodynamical setting. As an example, the garnet peridotite of Cima di Gagnone and Monte Duria in the Lepontine Alps are interpreted to originate from a partially serpentinitized peridotite (Evans & Trommsdorf, 1978). These may be prograde subduction zone peridotite if the protolith was placed in the mantle wedge before intrusion. However, if they resided in the crust before subduction (Evans & Trommsdorf, 1978), they would be crustal peridotite.

2.6.3 Mantle Wedge Garnet Peridotites (MWGP)

Following Brueckner (1998), Van Roermund (2009b) restricted the geodynamic environment during crustal emplacement of garnet peridotite to the interface between the hanging wall mantle and the subducting continental crust. Leaving space for mantle wedge and subduction zone types. These MWGP might come (1) from the subcontinental lithospheric mantle or (2) from the asthenosphere below the continents. In the first case (1), the original garnet assemblage would have an age \gg subduction ("relic" peridotite of Brueckner & Medaris, 2000). However, if the MWGP are incorporated into the subducting crust from the asthenosphere (in case of very deep subduction and/or "thin" subcontinental lithospheric mantle) the temperature would be too high to preserve ages $>$ subduction.

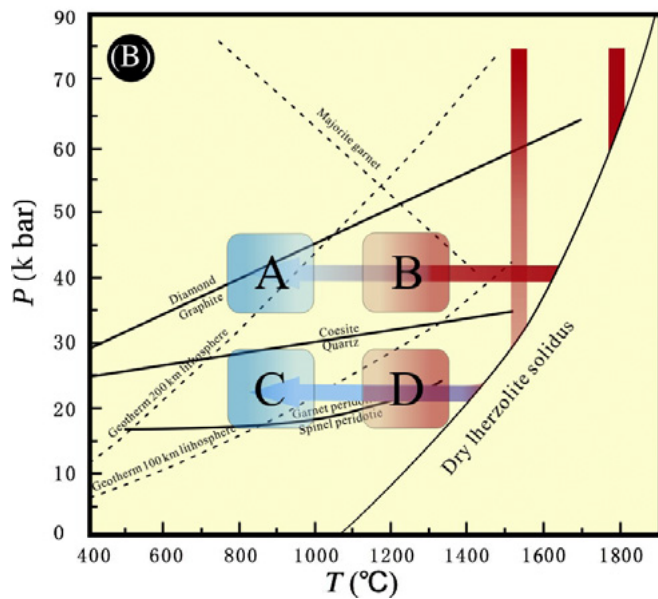


Fig. 2.6 - Range of PT conditions in which the metamorphic garnet-olivine mineral assemblage of a mantle wedge garnet peridotite is formed. The boxes indicate four different geodynamic settings: (A) cold and thick, (B) hot and thick, (C) cold and thin, (D) hot and thin. (modified after Zhang *et al.*, 2011)

Zhang *et al.* (2011) elaborated on the Van Roermund (2009b) model by subdividing in MWGP sub-types. In particular, the authors differentiate the mantle wedge garnet peridotite (MWGP) sub-type according to the characteristics of the SCLM. The SCLM can be differentiated according to the age of formation (old VS young), to its thickness (thick VS thin) and to its temperature (hot VS cold). In Fig. 2.6, four different possible metamorphic conditions for the formation of a stable grt+ol mineral assemblage are illustrated.

During continental collision, different combinations of SCLM are possible between the two plates. Each combination has its own characteristic evolution. Four environments have been analysed, Type A, B, C and D.

Type A refers to an old and static and type B to an active mantle wedge. The term active indicates that there is substantial flow and upwelling in that part of the mantle wedge. Type C and D are young mantle wedges, type C being static and type D being active.

This classification system allows to geodynamically interpret thermobarometric data resulted from EMP mineral chemistries of garnet peridotites. The conceptual geodynamic collisions illustrated in Fig. 2.7 A-D have PT conditions of the SCLM which are illustrated in the boxes in Fig. 2.6. Furthermore, single minerals as well as mineral assemblages might be dated, giving important constrains on the evolution of the SCLM prior and during the collision event.

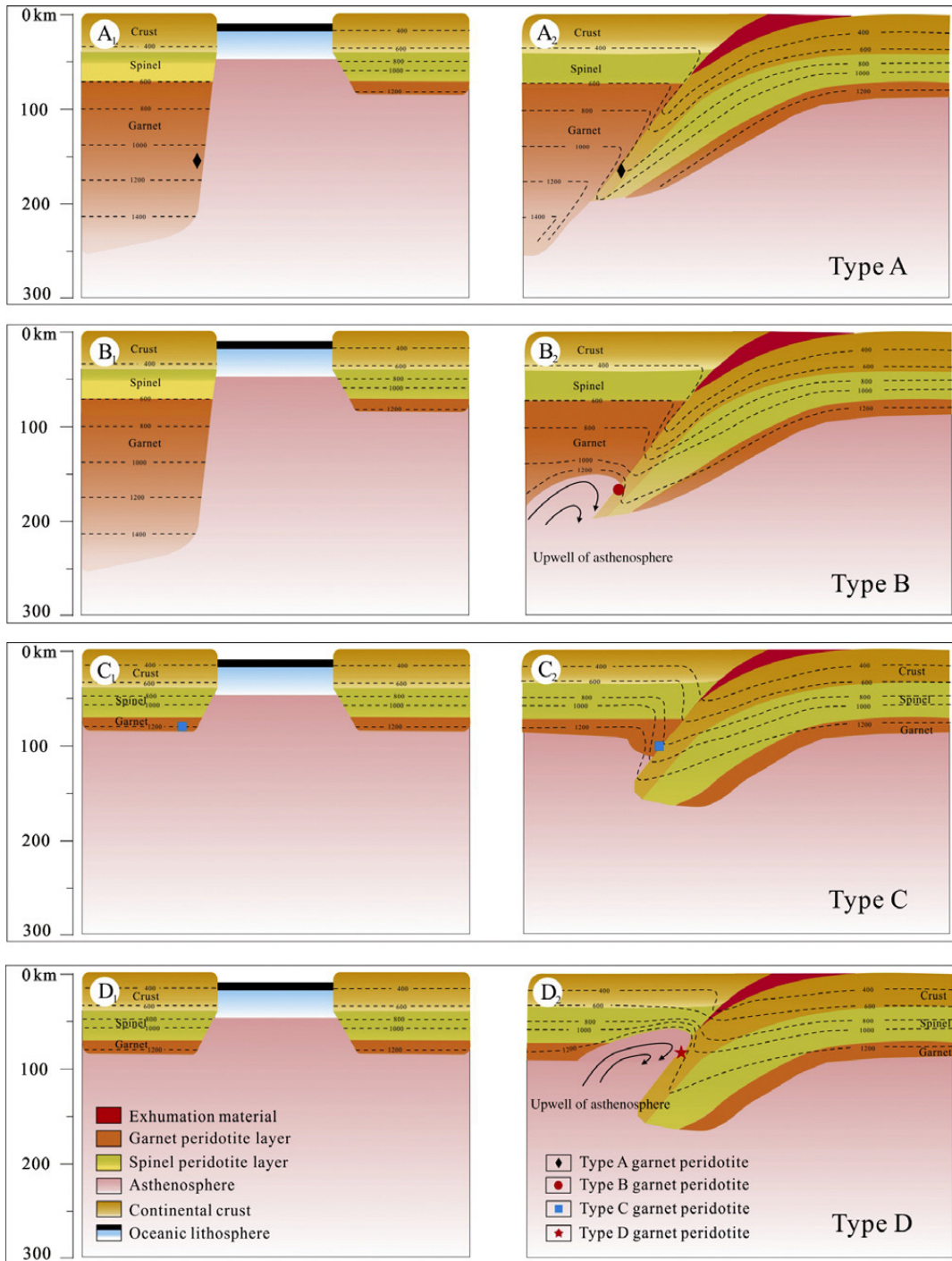


Fig. 2.7 - Simplified cartoon illustrating four different mechanisms for formation and crustal incorporation of mantle wedge garnet peridotites. The symbols A, B, C, and D correspond to boxes A, B, C, and D illustrated in Fig. 2.7. The diagrams to the left (A1, B1, C1, and D1) illustrate possible event(s) responsible for the formation of the SCLM. The diagrams to the right (A2, B2, C2, and D2) illustrate hypothetical continental collision events and possible mechanisms of crustal incorporation of garnet peridotites. (A) Old, cold and thick mantle wedge (cratonic) type collides with "normal" continental crust. Garnet peridotite older (>250 Ma) than the collision event. (B) Young, hot and thick mantle wedge collides with "normal" continental crust. Garnet peridotite have roughly the same age (<250 Ma) as the collision event. (C) Old, cold and thin mantle wedge (continental) type collides with "normal" continental crust. Garnet peridotite older (>250 Ma) than the collision event. (D) Young, hot and thin mantle wedge collides with "normal" continental crust. Garnet peridotites have roughly the same age (<250 Ma) than as the collision event. (modified after Zhang *et al.*, 2011).

2.6.4 Mechanisms of emplacement

Garnet-peridotite-bearing UHP terrains usually have pressure peaks in between 2.5-4.0 GPa. These extremely high pressures cannot be achieved simply by crustal stacking. Instead, the crust must subduct to about 100-140 km into the upper mantle (up to 200 km according to Spengler *et al.* (2009). Brueckner (1998) and Brueckner & Van Roermund (2004), trying to explain the occurrence of these UHP ultramafic bodies within gneissic terrains, formulate the Dunk Tectonics model. This model implies the presence of a wedge of mantle rocks directly above crustal rocks (Fig. 2.8). While the crustal terrane is subducting, slices of mantle material may be incorporated from the mantle wedge directly above the downgoing plate and carried along. Once the subduction forces are compensated by the buoyancy forces, the lighter crustal terrain will reside for a relative brief period of time at UHP depths. This would allow low pressure mafic and ultramafic bodies already present in the crustal terrain to reequilibrate in UHP eclogites and garnet peridotite respectively. When the condition that forced the crust to subduct into the mantle ceases (probably after slab break off), it will return towards the surface (eduction), probably along detachment surfaces, carrying the previously incorporated ultramafic bodies.

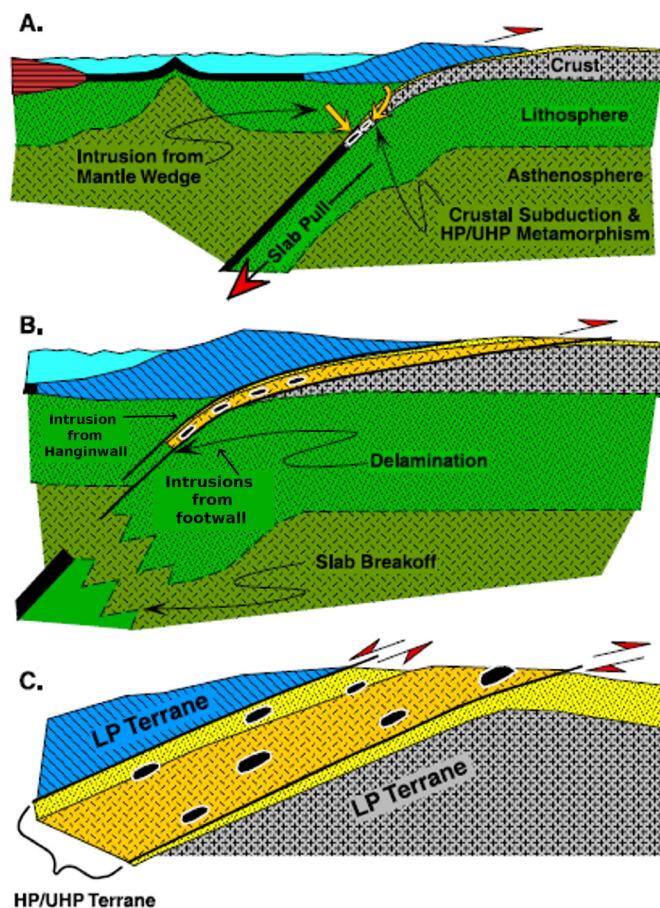


Fig. 2.8 - Simplified cartoon illustrating "dunk tectonics" model. A) Subduction of continental crust into the mantle. The slab pull is responsible for subducting part of the crust to deep levels. MWGP intrude into the subducted crust. B) Slab break off causes rapid eduction of the crust through detachment surfaces. This eduction is driven by buoyancy forces. During retrograde path, mantle fragments might intrude both from hangingwall and footwall. C) Eduction/Exhumation occur along detachment surfaces and provoke the juxtaposition of HP/UHP rocks within lower pressure rock. Peridotite bodies are shown as black lenses. (Modified after Brueckner & Van Roermund, 2004)

3 - METHODS

Field sampling

Seven oriented samples were collected from different locations in the FGP. The sample locations are shown in Fig. 4.1. In Tab. 4.1 samples are divided by lithology, mineral assemblage and GPS coordinate.

Optical microscopy

For each sample, thin sections were produced for optical investigation techniques. Thin sections for olivine fabric analysis were cut parallel to the lineation and perpendicular to the foliation. Crystallographic orientation of olivine was measured using a four axis Universal Stage (U-stage) applied to an optical microscope. The U-stage allows "precise" measurements ($\pm 5^\circ$ error) of planar and linear features within a thin section.

Electron microprobe analysis (EMP)

Mineral major element oxides compositions were determined by EMPA at the Utrecht University using a JEOL JXA8600N super probe. Equipped with five wavelength dispersive spectrometers, acceleration voltage of 15 kV and a beam current of 20 nA. Carbon coated thin sections were initially analysed with Energy Dispersive Spectrometry (ED) for quick identification of minerals and Wavelength Dispersive Spectrometry (WD) for high resolution mineral chemical analyses. Every major element analysis has a precision of $\pm 2.5\%$.

Fe^{3+} is calculated based on charge balance for anhydrous minerals (olivine, orthopyroxene, spinel) and with specific techniques for amphibole. For amphiboles, cations calculation is on the basis of an anhydrous formula with 23 oxygen rather than 24 (Leake *et al*, 1997). The ideal cation-sums in amphibole formulae are not fixed, but can vary between 15 and 16 cations (per 23 oxygen). $\text{Fe}^{3+}/\text{Fe}^{2+}$ ratio can be inferred adjusting the sum ($\text{Si} + \text{Al} + \text{Cr} + \text{Ti} + \text{Fe} + \text{Mg} + \text{Mn}$) to 13 (Leake *et al*, 1997).

Electron back-scattering diffraction (EBSD)

In one case (sample F10), the olivine grains were too small for effective use of U-Stage. In this case, Electron back-scattering diffraction (EBSD) technique was used. The sample was polished using colloidal silica for about one hour. The sample was then coated with a thin carbon layer to avoid electrostatic charge during analysis. Electron back-scatter diffraction (EBSD) patterns were collected using a FEI XL30 Field-emission (FEG) SEM at Utrecht University. Operating conditions were 15 KV acceleration voltage, 15 mm working distance and 70° sample tilt.

X-Ray Fluorescence (XRF)

Representative bulk rock compositions for both peridotite and eclogite were obtained through XRF analysis. Small fragments were initially crushed and the resulting powder ($< 73 \mu\text{m}$) was used on a sequential ARL 9400 WD-XRF at Utrecht University.

Thermodynamic calculations

Pseudosection of selected bulk rock compositions were produced with the software PerpleX 6.6.6 (Connolly, 2009; <http://www.perplex.ethz.ch/>). The software uses Gibbs Free Energy minimization to compute pseudosections under the assumption of chemical equilibrium throughout a certain bulk rock volume. Links to the software web page, as well as to the file and description of the used databases are listed in Tab. 3.1.

Tab. 3.1 - Links to the thermodynamic software PerpleX 6.6.6.

Name	Description	Reference	Link
PerpleX 6.6.6	Software	Connolly (2009)	http://www.perplex.ethz.ch/
cr_hp02ver.dat	database with Cr phases	Holland & Powell (1998)	http://www.perplex.ethz.ch/perplex/datafiles/cr_hp02ver.dat
solution_model.dat	Solid solutions database		http://www.perplex.ethz.ch/perplex/datafiles/solution_model.dat

Thin section decoration

Dislocations are too small to be observable in a thin section but the staining method of olivine described by Kohlstedt *et al.* (1976) provides a valid alternative to TEM techniques. Dunitite and garnet peridotite samples were heated to the temperature of 1000°C for one hour, allowing the oxygen to rapidly diffuse along dislocation, reacting with the Fe²⁺ present in the lattice and precipitate as Fe-oxides (mostly hematite). As such, dislocations are revealed as thin lines of reddish colour, visible at moderate magnification (x20-x50) with the OM.

4 - FRININGEN GARNET PERIDOTITE

Located in N-Jämtland (Sweden) near lake Friningen (GPS: 64°44'430" N, 014°33'444' E), the Friningen Garnet Peridotite (FGP) is the largest (30x300 m large) and best preserved garnet peridotite body outcropping in the Central Belt of the SNC. It was first described by Van

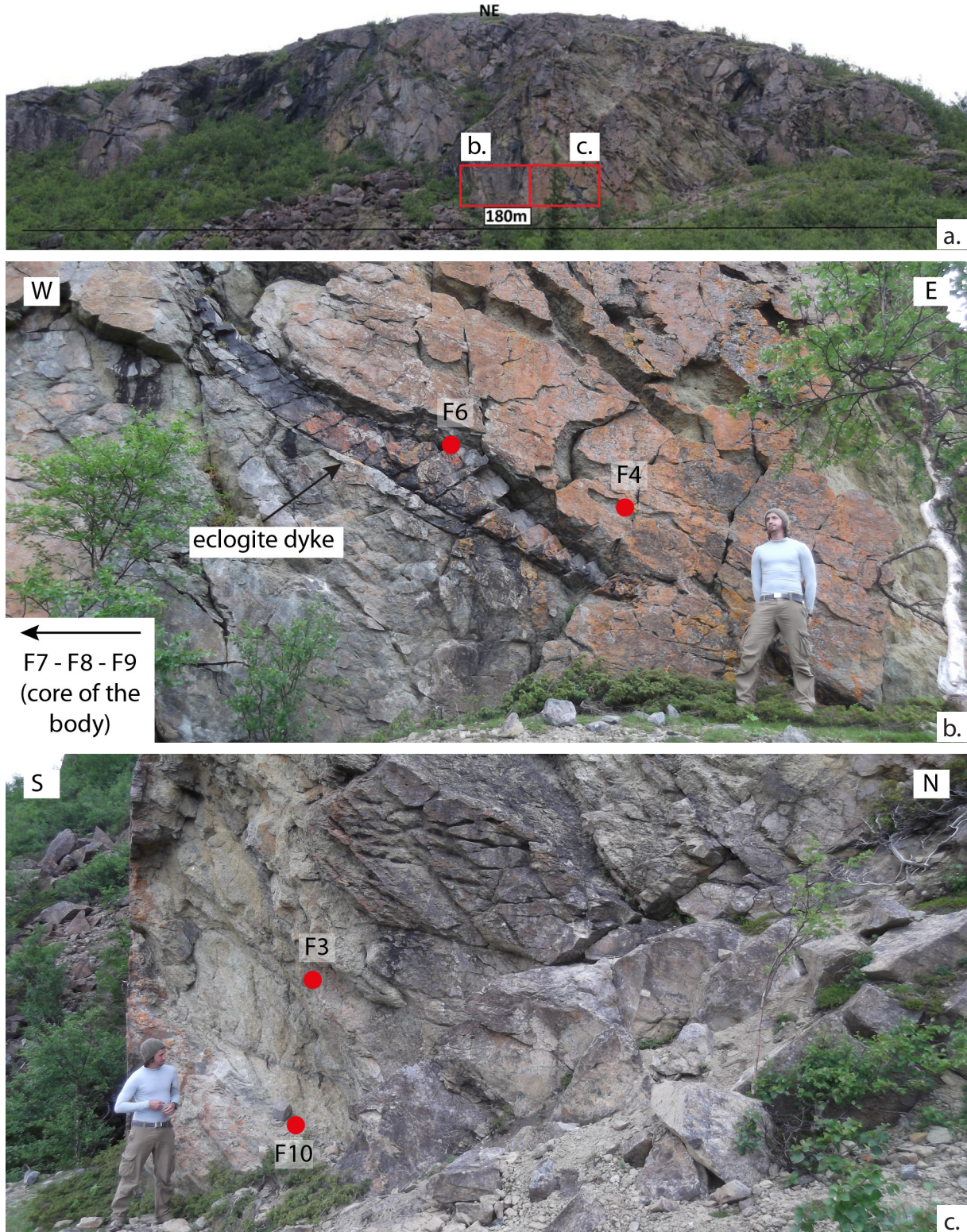


Fig. 4.1 - (a) Overview of the FGP body. (b) note in the eclogitic dyke (centre of the image) Janak *et al.* (2013) discovered the UHP mineral assemblage. (c) note the anastomosed shear zone to the left of the image. (RT90: X7182375 - Y1440591).

Roermund (1989) and, more recently, Verbaas & Van Roermund (2012) did some detailed mapping. A brief summary of lithologies, structures and metamorphism is now presented, for more detailed information, the reader is referred to Verbaas & Van Roermund (2012). Several new samples were collected for this study (Tab. 4.1). Fig. 4.1 shows a section of the FGP; red dots indicate the sample locations.

Table 4.1. Collected samples

Sample Name	Rock Name	Location	GPS coordinate (RT90)
F3	Harzburgite	Near shear zone	X 7182375 - Y 1440591
F4	Harzburgite	Near shear zone	X 7182375 - Y 1440591
F6	Eclogite	Dyke	X 7182375 - Y 1440591
F7	Spl dunite	Core of the body	X 7182493 - Y 1440561
F8	Grt lherzolite	Core of the body	X 7182452 - Y 1440572
F9	Grt dunite	Core of the body	X 7182444 - Y 1440595
F10	Harzburgite	Anastomosed SZ	X 7182375 - Y 1440591

4.1 Lithologies

The FGP consists of a series of layers with different bulk rock compositions, ranging from almost pure dunite to garnet-lherzolite. A 30 cm wide boudinaged dike runs through the outcrop (Fig.4.1b). This dike consists mainly of garnet pyroxenite but, locally, its composition varies to ky bearing eclogite. All lithologies are substantially unweathered. Rare mm thick serpentine and talc veins are observed.

Dunites are almost pure in composition, with an opx content ranging from 5 – 10%. The transition between layers of different composition is usually characterised by a progressive variation of the relative amount of pyroxenes and/or garnet. The only exception is given by cm-thick orthopyroxene layers, characterized by a sharp contact with the other layers.

All lithology preserves HP-HT mineral assemblages. Serpentinization is rare and localized along late mm-sized veins.

4.2 Structures

Compositional layering (D1)

The S1 foliation is defined by the compositional banding in the peridotite, characterised by the variation of the relative amounts of the main minerals (ol, opx, cpx and grt). The thickness of these layers is highly variable and can vary from 5-10 cm in some garnet orthopyroxenite layers to several meters in some dunite layers. However, the contact between layers is often not sharp but characterised by a progressive change in mineral modes, making it difficult to infer their exact thickness. A 30 cm thick, boudinaged eclogite dike lies parallel to the compositional layers (Fig. 4.1b).

D2

The compositional layering S1 is folded in tight to isoclinal folds. These can be observed especially in the dike and in some orthopyroxene layers (F2). The S2 foliation is the axial plane foliation of the isoclinal folds, it is the main foliation in the outcrop and it dips around 160/30. Due to the granoblastic nature of the rock, S2 is only visible through deformed garnet clasts and/or stretched and elongated spinel-opx aggregates. This foliation is usually

sub-parallel with S1. However, in some cases, S2 forms an angle of about 25° - 30° with the S1 compositional layering.

D3

A third and weak foliation (S3) is present that forms an angle of about 60° with S2. S3 dips around 80/25 and is especially found within 10-30 cm thick anastomosing shear bands in the Central part of the outcrop (Fig. 4.1c).

4.3 Metamorphism

Verbaas & Van Roermund (2012) identified five different metamorphic events: M1, M2, M3, M4 and M5. However, the metamorphic events are here reduced to four as M3 and M4 are now considered to be the same event. The mineral assemblages, as well as the microstructures of these four phases in the different lithologies, garnet peridotite/dunite and garnet pyroxenite/eclogite, are described below in chronological order. Mineral abbreviations are after Siivola & Schmid (2007).

4.3.1 - Garnet peridotite

The FGP body is mainly composed of garnet-bearing lherzolites, harzburgites and dunites. However, the garnet is usually overprinted by lower grade phases and is preserved only locally. In Tab. 4.2 the paragenetic diagram of the FGP is illustrated. the diagram was produced after the analysis of several thin sections coming from different layers.

Table 4.2. Paragenetic diagram of the FGP. The colour indicates the occurrence of the same phase with a different microstructure. Red: first microstructure; blue: second microstructure; green: third microstructure. Dashed lines indicate uncertainties.

	D1		D2	D3/static	-
	M1a	M1b	M2	M3	M4
ol	Red	Red	Blue	Green	
opx	Red	Red	Blue	Green	
cpx	Red	Red	Blue		
grt	Red		Blue		
spl		Red	Blue	Blue dashed	
parg/tr		Red	Blue		
chl				Red	
mag					Red

M1a

The M1a assemblage consists of mm- to cm-sized relict clasts of ol+opx+cpx+grt (Fig. 4.2-4.3). All these clasts are heavily fractured and deformed. Olivines are usually mm-sized, although in areas of very low deformation they reach sizes up to 1 cm. Several olivine clasts show undulatory extinction and kink bands (Fig. 4.2c). These characteristics are examined in detail in chap. 4.7.

Orthopyroxene and clinopyroxene are often 0.5-0.8 cm large and show undulatory extinction. Both phases show exsolution lamellae of garnet (in cpx) and garnet and cpx (in opx). These exsolutions are related to M1b and M2 metamorphic events (Fig. 4.2b-4.3).

Grt1 is rarely preserved in the core of M1b symplectite. Assuming no change in volume

during the reaction, grt1 were originally about 0.5-1.5 cm in size. However, Van Roermund (1989) found rare poikiloblast of grt1 up to 5 cm in size, but widely recrystallized in grt2. M1a phases are often transected by trains of mono- or multiphase inclusions, usually consisting of Sr-bearing Mg-Fe-Ca carbonates, diopside, Fe-Ni sulfides and rutile (Fig 4.2c-d).

M1b

M1b is represented by the common break-down of grt1 in a characteristic “coarse grained” symplectite, consisting of $opx \pm cpx + spl + parg$ with relics of grt1 sometimes preserved in the core. A typical example of such M1b symplectite after grt1 (now partially overprinted by grt2) is shown in fig. 4.3. Note the two types of spinels in the picture: the large, globular and zoned spinels at the edge of the grt1 (now replaced by M1b symplectite) and the small and rounded spinels in the core of the symplectite assemblage, with a typical vermicular structure. Note that in fig. 4.3 the thickness of this structure is about 30-100 μm . Furthermore, exsolution lamellae of garnet and cpx were formed from the original high-Al cpx1 and opx1 respectively (Fig. 4.2a-b).

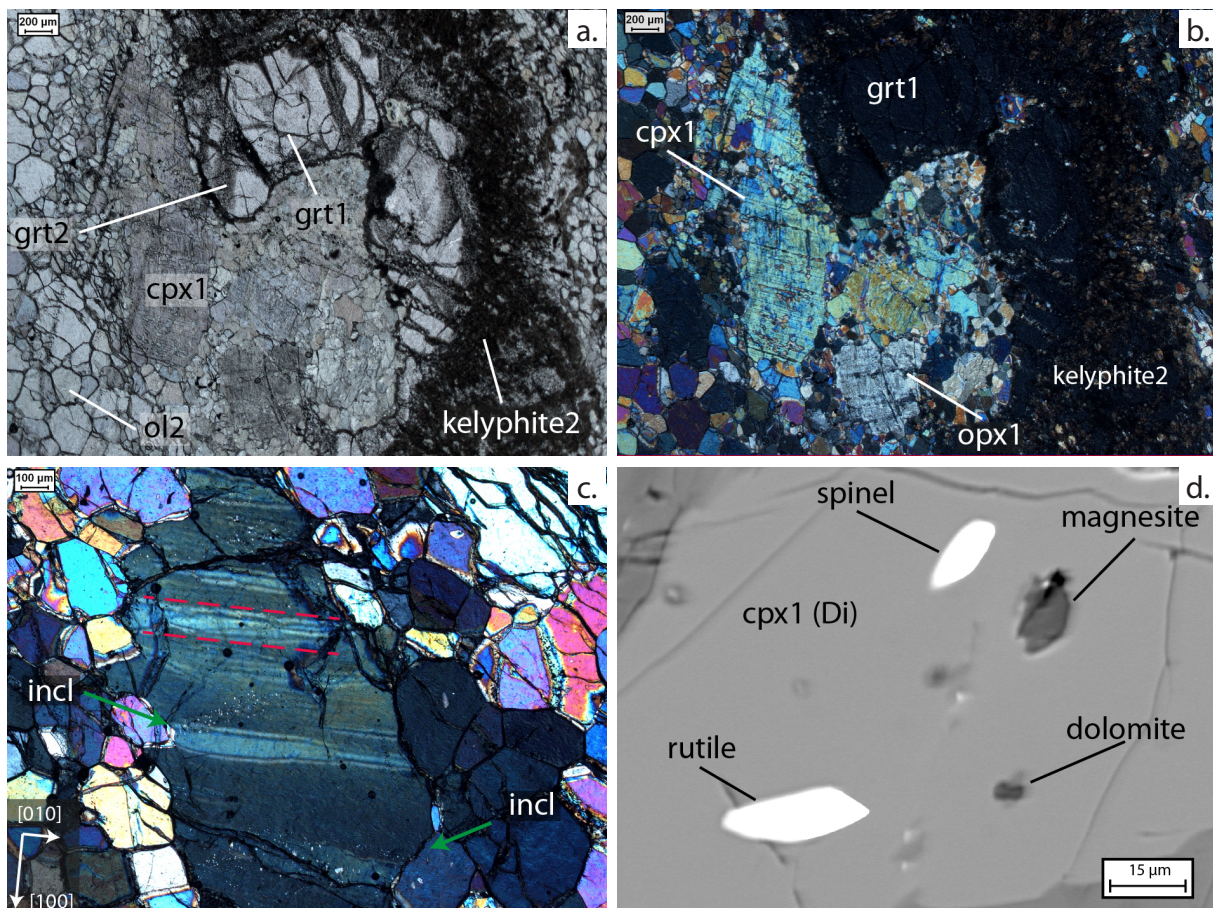


Fig. 4.2 - (a.) Photomicrograph in PPL of ol+grt+opx+cpx (Sample F8). Note the fractured grt1 with grt2 crystallized along fractures. Both grt's are surrounded by the M4 kelyphite. Note that the latter does not develop at the contact between grt1 and cpx1/opx1. (b.) Photomicrograph of (a.) in XPL. Note the large cpx1 and opx1 with exsolution lamellae of grt and/or cpx. (c.) Photomicrograph (XPL) of ol1 (in the centre) surrounded by smaller grains of ol2 “foam microstructure” (sample F8). The red dashed lines indicate the orientation of the kink bands. The crystallographic orientation of the grain is shown in the inset square in the bottom left side of the picture. Note the trains of fluid inclusions, sharply cut at the rim of the crystal (green arrows) (d.) BS image of inclusions of spinel, rutile, magnesite, and dolomite, within cpx1. The gray scale reflects the relative density of the minerals (the whiter the denser).

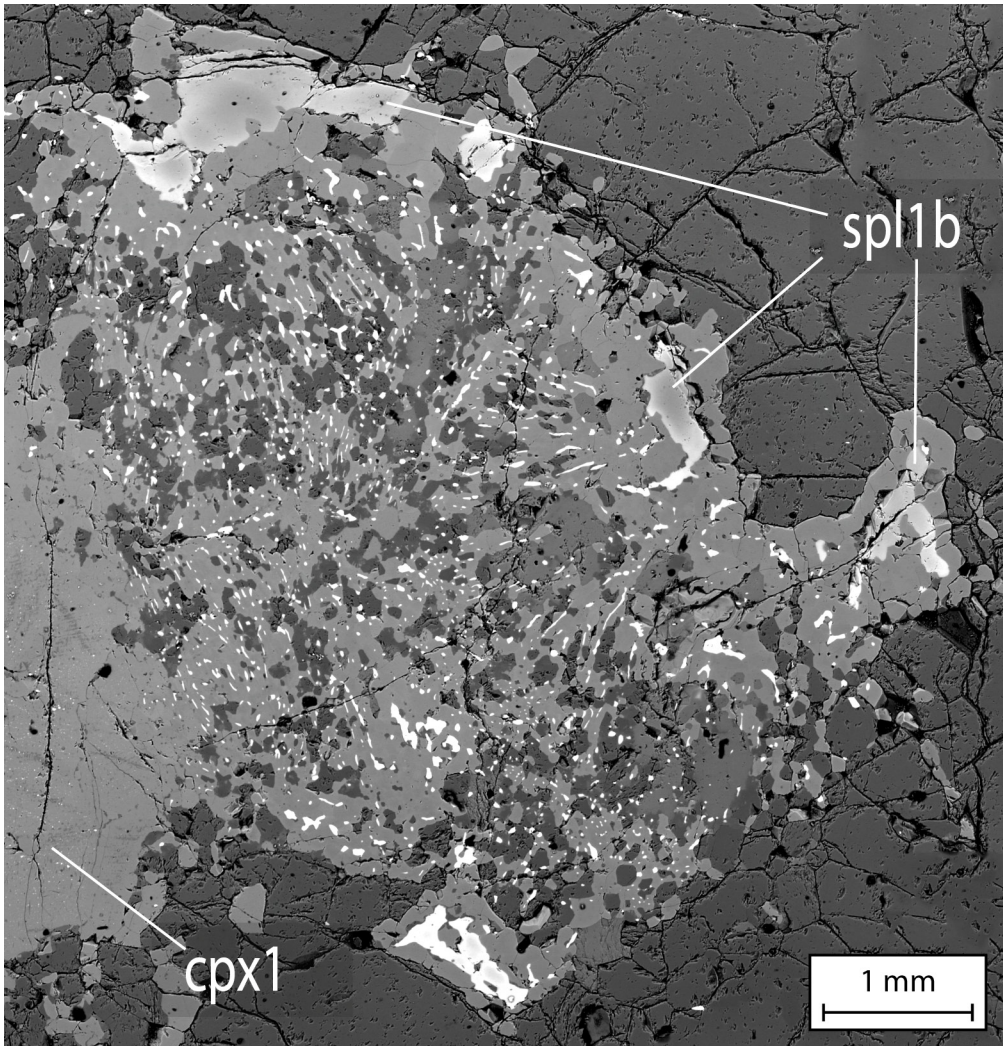


Fig. 4.3 - BS image of a pseudomorph after grt1 (M1b symplektite), partially replaced by grt2. The M1b symplektite consists of pargasite (dark gray), enstatite (lighter gray) and large globular spinels at the rims, progressively decreasing in size towards the core. The zoning, from core to rim, can be easily visualized by colour difference, darker in the core and brighter in the rims. Note the cpx1 to the left of the picture and the M2 olivine surrounding the pseudomorph. Note grt2 rims around the large globular spinels. The relative temporal relationships are the following: (1) large grt1 is stable with cpx1. (2) the grt1 break-down in parg+opx+spl symplektite. The size of the spinels increase towards the rims of the symplektite. (3) grt2 partially replaces the symplektite. This event is responsible for the zoning in spinels.

M2

The M2 phase consists of ol₂+opx₂+grt₂+spl₂±cpx₂±parg₂. Ol, opx, cpx and parg grains display an annealed texture (Fig. 4.2a-b and 4.4a), characterised by optically strain free grains having straight grain boundaries meeting in 120° triple point junctions (“foam microstructure”). The grain size appears variable and depends on the proximity with D3 shear zones and on the bulk rock chemistry. In garnet peridotite it is possible to see the transition between ol₁ and ol₂ grains (Fig. 4.2c). Spinel and garnet dunite, located far from D3 shear zones (sample F7-F9) have a grain size up to 500 µm (Fig. 4.4a). Garnet harzburgites/lherzolites (F8) typically show a finer grain size of about 50-200 µm. Grt₂ partially replaces the M1b symplectite, and grows as rims over the large globular spinels and/or as exsolved phase along lamellae parallel to opx₁ and cpx₁ cleavage planes. Fig 4.3 shows a typical example of symplectite after grt₁, partially replaced by grt₂. Note in Fig. 4.3 the chemical zoning within large globular spinels, darker in the core and brighter in the rims. Smaller spinels do not show such a zoning, however they display the same bright colour at the rims of larger spinels.

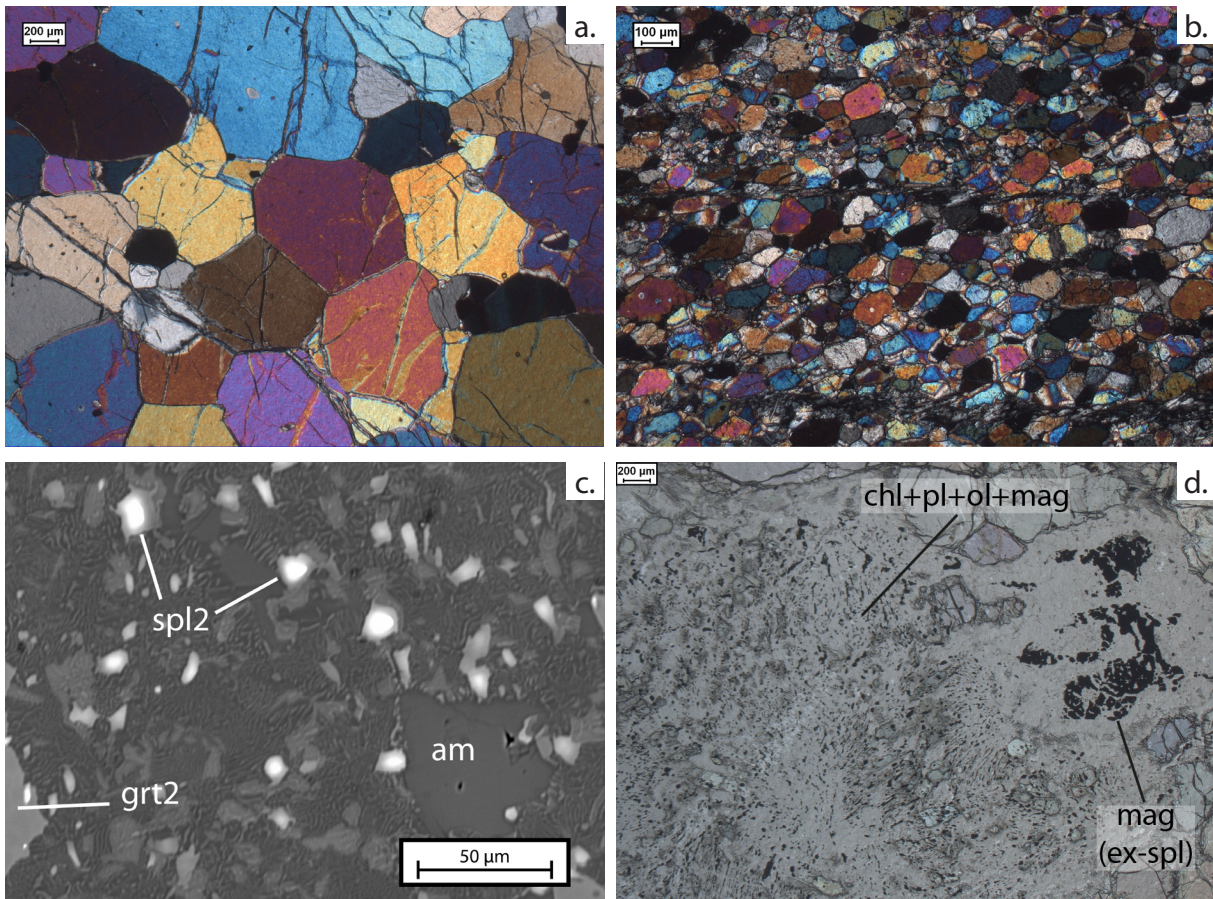


Fig. 4.4 - (a.) Photomicrograph in XPL of M2 olivine "foam microstructure" in dunite (Sample F7). Note the olivine grains with straight boundaries meeting in 120° triple point junctions. (b.) Photomicrograph in XPL of M3 olivine "foam microstructure" in deformed harzburgite (Sample F10). Note the much finer grain size with respect to the sample in fig. 4.4a, coming far from the shear zone. (c.) BS image of an M3 symplectite after grt2. Note the very thin (3-5 μm thick) vermicular structure (d.) Photomicrograph in PPL of a chl+pl+ol+mag pseudomorph replacing previous M1b/M3 symplectite. Note structure drawn by the magnetite, resembling the structure of the original symplectite after grt1. Furthermore, note the white halo around the globular magnetite crystal, representing its original grt2 rim.

M3

The M3 assemblage is defined by the stability of $\text{ol}+\text{opx}\pm\text{am}\pm\text{chl}$. This phase is often associated with the D3 deformation event and is typically found within the anatomised shear zones (Fig 4.4b). Along D3 shear zones, all M1 and M2 structures are obliterated. Grt1 and grt2, as well as cpx1 and opx1 are re-equilibrated in M3 $\text{opx}_3+\text{am}\pm\text{chl}$ in highly stretched and flattened domains, parallel to the S3 foliation. Note in fig. 4.4b the M3 olivine "foam microstructure". Despite its much finer grain size (20-80 μm), it resembles the M2 olivine microstructure.

In the inner portions of the body, unaffected by the D3 deformation phase, the M3 phase is expressed by the static overprint of M1 and M2 mineral assemblages (especially M1 and M2 garnets). Grt1 and grt2 are partially (along rims) or totally replaced by spl+opx+parag kelyphite (Fig. 4.2a-b; 4.4c). This reaction is observed only where grt2 is in direct contact with olivine and it appears at the OM (PPL) as a brownish rim around grt2. As it is shown in fig. 4.2a-b, this reaction does not take place at the contact between garnet and pyroxene. Furthermore, note from the scale difference between fig. 4.3 and fig 4.4c that the M3 kelyphite can be easily differentiated from the M1b symplectite due to its much finer vermicular structure (thickness < 10 μm).

M4

Since the peridotites are rather fresh and unaltered, it is beyond the purpose of this thesis to differentiate temporally metamorphic overprints after M4. The most noticeable event comprises the complete re-equilibration of grt2 in chl+plag+mt assemblages found in some thin sections (Fig. 4.4c-d) as well as the rare talc and serpentine veins.

Discussion

The oldest mineral assemblage (M1a) in the garnet peridotite, ol1+opx1+cpx1+grt1, represents the remnants of the original mantle texture. The partial or complete recrystallization of grt1 in opx+cpx/parg+spl (M1b) indicate that the rocks underwent a decompressional phase while still being in the mantle. However, in the FGP, this M1b kelyphite structure is always replaced, partially or totally, by metamorphic overprints (such as M2 and/or M3). Nevertheless, similar decompression structures are described from several other garnet peridotite bodies. Schmädicke *et al.* (2010) described a similar kelyphite from a garnet-bearing ultramafic rock

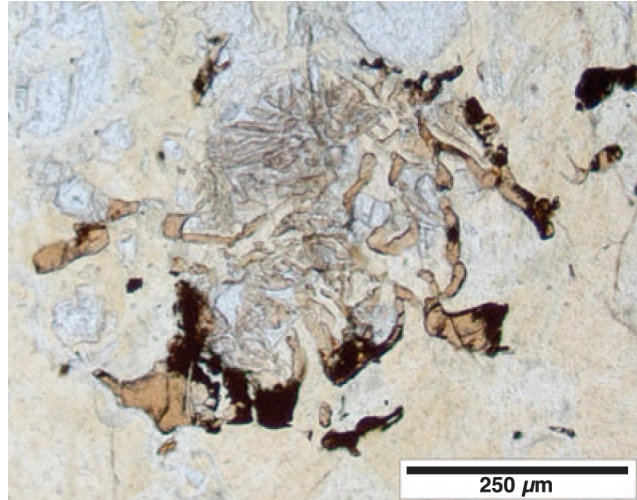


Fig. 4.5 - Kelyphite after garnet, Saxonian Granulitgebirge Core, Bohemian Massif. The garnet is completely replaced by spinel-bearing kelyphite. Note the characteristic structure consisting of vermicular-shaped spinels in the core and large and globular spinels in the rims. (Schmädicke *et al.*, 2010)

from the Saxonian Granulitgebirge Core, Bohemian Massif (Fig. 4.5). Note the similarity in structure and the scale difference between the garnet in fig. 4.3 and the kelyphite in Fig. 4.5 and the post-M2 kelyphite in Fig. 4.4c.

The presence of amphibole indicates the presence of water in the rock. As mantle rocks are generally believed to be dry, the provenance of this water is unclear. On the one hand, it could have been initially in solution in olivine and/or other M1a mineral and then released after decompression. In fact, the water solubility in olivine is strongly pressure dependent. However, water might have been introduced during a thinning (i.e. extending) phase related the opening of the lapetus Ocean. Alternatively, COH fluids may have been introduced during collision (subduction zone fluids). This event is recorded by several trains of Sr-bearing fluid inclusions (now mainly carbonates) exclusively present in M1a-b mineral assemblages. It is, however, difficult to clearly define which fluids were involved in the formation of the amphiboles. Opx1 and cpx1 contain high-Al phases (cpx and grt) in the exsolution lamellae. This may indicate that the M1a to M1b decompressional phase was accompanied by cooling. The Al solubility in pyroxene, in fact, is strongly temperature dependent.

The M2 garnet overgrows the lower pressure M1b kelyphite and grows over the large globular M1b spinels. The presence of spinel inclusions in Grt2, as well as grt2 rims around globular spinels, indicates that grt2 contains lower Cr content compared to grt1. The M2 phase records intense deformation (called D2 in section 4.1). This is reflected in a much smaller grain size of the M2 ol2+opx2+cpx2+grt2+parg2 with respect to the size of M1 clasts. The

D2 deformation phase was initially penetrative, involving the entire body. Later deformation, (D3) localized along anatomised shear zones at lower temperatures and pressures, within the stability field of the M3 mineral assemblages ol+opx+cpx+chl+am+spl. Late metamorphic events (M4) sometimes re-equilibrate grt1, the M1b symplectite, grt2 and the M3 kelyphite in chl+plag+mag. This reaction was probably assisted by an intense hydration of the rock. Furthermore, the much finer size lamellae of the M3 kelyphite compared to the M1b kelyphite indicate a lower temperature of formation.

4.3.2 - Eclogite/garnet pyroxenite

Eclogites are found only within the dike crosscutting the garnet peridotite (Fig 4.1a). This dike is, however, very wide in composition. Its mineral assemblage can vary from ky+dol-bearing eclogite to garnet pyroxenite. In this eclogite, the first evidence of UHP metamorphism (3.0 GPa - 800°C) in the SNC was found by Janàk *et al.* (2013). The paragenetic diagram of the eclogite is shown in Tab. 4.3.

Table 4.3. Paragenetic diagram of eclogitic dyke. The colour indicates the occurrence of the same phase with a different microstructure. Red: first microstructure; blue: second microstructure. Dashed lines indicate uncertainties.

	M1	M2	M3
grt	Red	Blue	
omph	Red	Blue	
ky		Red	
zoi		Red	
phen		Red	
dol		Red	
plag	- - - ??? - - -		Red
dio			Red
sapp			Red
calc			Red
bio			Red

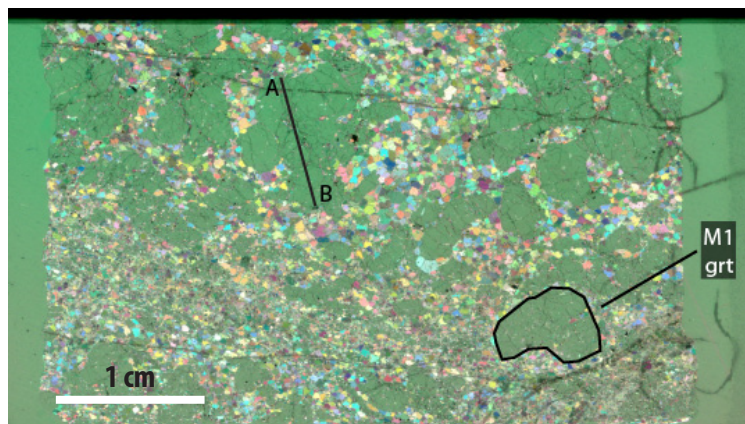


Fig. 4.6 - Scan of thin section F6 (eclogite). Note the cm-sized M1 garnets (outlined in black) and the small M2 omphacite (high pleochroism) in the matrix. The A-B linescan is shown in Fig. 5.8b.

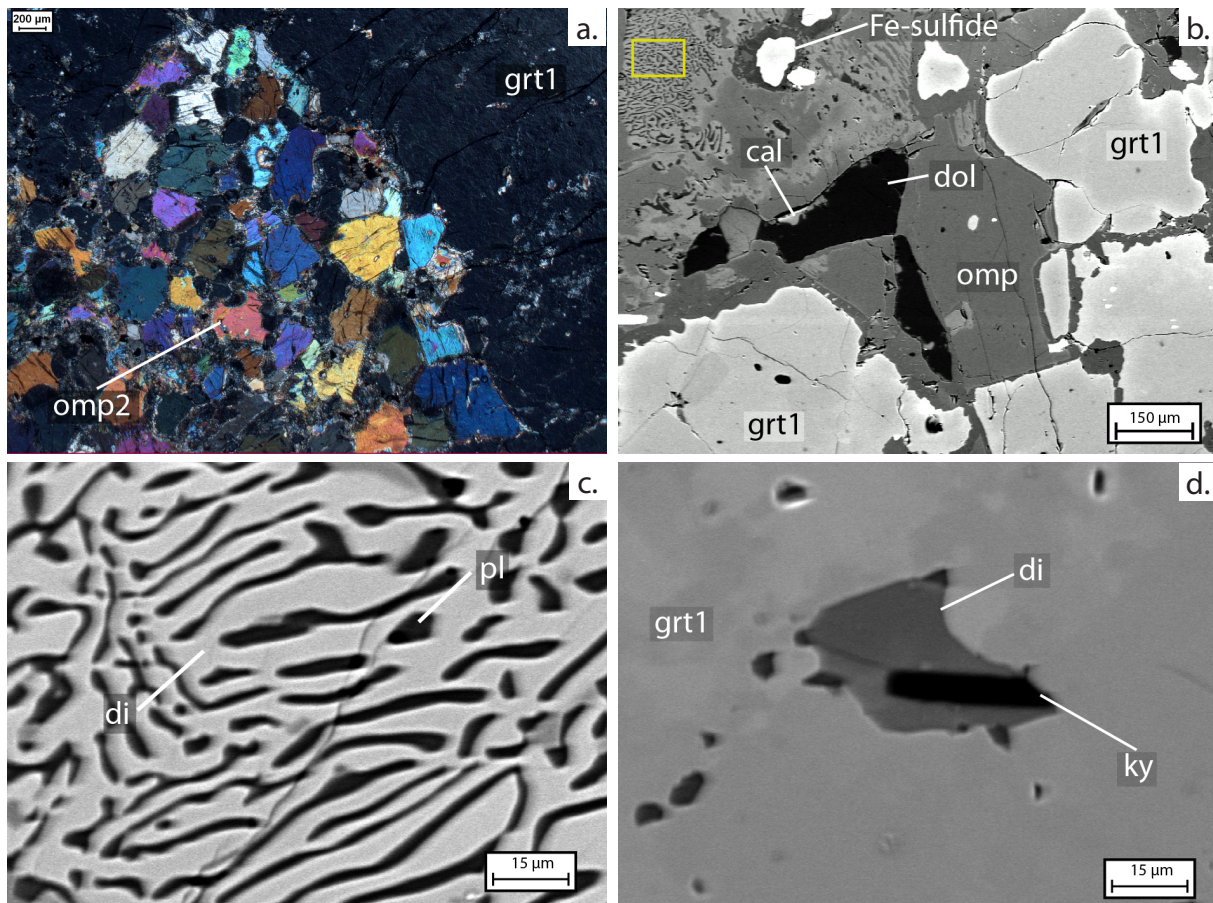


Fig. 4.7 - (a.) Photomicrograph in XPL of the eclogite (Sample F6). Note the large M1 garnets (grt1) and the smaller re-crystallized M2 omphacites (omp2) with pl+di symplectites at the rims. Furthermore, note the small grt2 surrounded by pyroxenes. (b.) BS image of the eclogite (sample F6). Note the large grt1, slightly zoned at the rims and the large black dolomite crystals with calcite in the rims. The Fe-sulfide (top to the left) is really bright because of its higher density with respect to the other phases. The area squared in yellow is a M3 pl+di symplectite after omp2. This area has been magnified further in (c). Note the typical vermicular structure of the post-omphacite symplectite. (d.) BS image of ky (black needle) and di (dark grey) inclusions in grt1. The grey-scale indicates the relative density of phases.

M1

The M1 assemblage consists of large megacrysts (up to 1 cm) of clinopyroxene and garnet. Grt1 is never preserved but can easily be recognized by the outer shape of recrystallized grt 2. The two generations of garnet can be differentiated only by size (Fig. 4.6) and/or by the shape of the garnet domain. The composition of clinopyroxene is highly variable in its Na content, shifting from diopside to omphacite. Several of these porphyroblasts contain opx and/or grt exsolution lamellae. Trains of fluid and/or solid inclusions crosscut the M1 phases. Furthermore, Verbaas & Van Roermund (2012) found a positive Eu anomaly in the bulk rock composition of this dyke. This has been interpreted as an indication for the presence of M1 plagioclase during this phase.

M2

The M2 assemblage consists of recrystallized grains of cpx/omph2+grt2 with occurrence of zoisite, dolomite, phengite and kyanite (Fig. 4.7). Cpx2 is generally smaller than cpx1 (100-200 μm in size) and often shows straight boundaries with 120° triple junctions, resembling the olivine "foam microstructure" found in peridotite (Fig 4.7a). This feature is especially seen in low-Na cpx. If the cpx is more Na-rich, late ab+di symplectites are formed at their rims (Fig 4.7a-c). M2 garnet occurs both in clusters, completely replacing grt1 or in smaller single

grains (50-100 μm in size) surrounded by pyroxenes (Fig. 4.7a). All recrystallized M2 garnets show a slight and narrow (5-10 μm thick) chemical zoning at the rim. This zoning is visible in BS images as a brighter halo at the rim of the crystals (Fig. 4.7b).

M3

The M3 assemblage is characterised by the partial or complete break down of the M2 mineral phases. Omphacite, kyanite and phengite are replaced by di+pl and/or spr+ab symplectites respectively. Note in fig. 4.5c the typical pl+di symplectite after omphacite. Dol grains often show partial rims of calcite (Fig. 4.5b). PT condition of 1.0 GPa - 800°C are reported by Janàk *et al.* (2013) for the M3 mineral assemblage.

Discussion

The dike shows high mineralogical variability, both in the chemical composition of the main minerals (diopside to omphacite) and the type of accessory minerals (kyanite, dolomite and phengite). The reasons for these sharp compositional changes is unknown. They might reflect initial magmatic layering, resulted from multiple magma injections of slightly different composition, then reworked during metamorphism. Conversely, they might be due to a kind of metamorphic layering.

The older assemblage (M1) in the dyke consists of large garnet crystals stable with large omphacite, in the eclogite sectors, or diopside in the garnet pyroxenite.

The M2 assemblage consists of grt₂+omp/di±ky±zo±phg±dol. The cpx microstructure resembles the olivine "foam microstructure" found in the garnet peridotite. Furthermore, the M2 assemblages in eclogite and peridotite have the same orientation, at least in the proximity of the eclogitic dyke. As such, the assemblages are interpreted to have formed under the same metamorphic event interpreted to have occurred at 3.0 GPa/800°C (Janàk *et al.*, 2013).

The M3 phase is recorded by the overprint of dio+spl+bio+pl around omph, ky or phen rims. PT conditions for this phase (1.0 GPa - 800°C) were determined by Janàk *et al.* (2013). This latter physical conditions (M3) are approximately similar to that determined by Van Roermund (1985) and Van Roermund & Bakker (1983) for retrograde conditions in external eclogites.

4.3.3 - Relationship between deformation and metamorphisms in different lithologies

The mutual relationship between deformation and metamorphism in eclogite and garnet peridotite is summarized in Tab. 4.4.

Table 4.4. Relationship between time, deformation and metamorphism in eclogite and garnet peridotite.

	Proterozoic		Caledonian		
	Mantle tectonite (D1)		D2	D3	Static overprint
Garnet peridotite	M1a	M1b	M2	M3	M4
Eclogite	M1		M2	M3	

It is unclear whether the M1a assemblage in peridotite was already present when the dyke was emplaced. This emplacement has been interpreted by Brueckner *et al.* (2004) to be related to a Proterozoic refertilization event. If this is the case, the M1 assemblage would have formed only after the intrusion of the dyke. The M1b event is present only in the garnet

peridotite. This implies that the rock was still within the stability field of grt+omp during this event.

The D3 event is a very localized deformation event, present only along shear zones; in peridotites, this deformation is associated with a metamorphic overprint (M3). However, M3 is present as a static microfabric only a few meters away from the D2 shear zones. The final metamorphic overprint (M4) is only observed in the peridotite. This event seems to be unrelated to any post-D2 deformation and is therefore called a static overprint.

Table 5.1. Continued (1)

Mineral	CLINOPYROXENE				GARNET									
Rock	GARNET PERIDOTITE (F8)				GARNET PERIDOTITE (F8)									
Mineral assemblage	M1 porphyroclasts		M2 "foam" microstructure		M1a		M2		M2 (in M1b spl rims)		M2 (opx exsol. lamellae)		M2 (cpx exsol. lamellae)	
N°	7	8	9	10	8	9	21	22	30	31	36	39	34	35
SiO2	53.59	53.05	54.25	54.20	41.48	41.45	41.65	42.03	41.41	40.79	42.01	41.21	41.45	41.74
TiO2	0.20	0.20	0.14	0.18	0.10	0.04	0.00	0.01	0.04	0.06	0.02	0.03	0.05	0.06
Al2O3	2.08	2.05	2.26	2.11	21.83	21.71	22.84	22.73	22.83	22.37	22.67	22.44	22.02	22.24
Cr2O3	1.05	1.03	0.70	0.81	2.14	2.14	0.85	0.90	1.01	1.01	1.09	1.11	1.38	1.32
FeO	1.63	1.63	1.69	1.74	10.56	10.54	10.15	10.44	9.30	9.70	10.81	10.94	12.04	11.81
MnO	0.08	0.05	0.07	0.03	0.50	0.49	0.43	0.43	0.54	0.59	0.59	0.68	0.81	0.90
MgO	16.33	16.19	16.40	16.25	18.37	18.27	18.76	18.60	19.36	18.68	18.62	18.54	16.97	16.74
NiO	0.04	0.03	-	-	0.01	0.00	0.00	0.02	0.02	0.06	0.00	0.00	0.04	0.00
CaO	22.87	22.77	22.55	22.79	4.91	5.12	4.35	4.42	4.81	4.66	4.44	4.09	5.24	5.34
Na2O	1.02	1.14	1.25	1.14	-	-	-	-	-	-	-	-	-	-
TOTAL	98.87	99.24	99.29	99.26	99.91	99.76	99.03	99.58	99.34	97.91	100.26	99.04	100.00	100.13
Mg#	0.992	0.983	0.967	0.951	0.756	0.771	0.767	0.761	0.788	0.775	0.755	0.757	0.716	0.716
Cr#	-	-	-	-	0.062	0.053	0.024	0.026	0.029	0.029	0.031	0.032	0.040	0.038

Table 5.1. Continued (2)

Mineral	SPINEL								Amphiboles			
Rock	DUNITE (F7)		GARNET PERIDOTITE (F8)						GARNET PERIDOTITE (F8)			
Mineral assemblage	M2		M1b (core)		M1b (rim)		M2		M1b/M2		M2	
N°	1	10	61	62	68	70	37	38	8	9	11	12
SiO2	0.01	0.02	0.01	0.02	0.02	0.04	0.94	0.27	43.69	43.14	44.34	44.34
TiO2	0.02	0.04	0.03	0.02	0.03	0.15	0.02	0.05	1.20	0.94	0.99	1.09
Al2O3	30.10	29.06	52.50	52.28	40.52	40.42	38.47	36.49	14.70	13.36	12.84	12.78
Cr2O3	38.03	39.30	16.96	16.88	28.46	28.59	29.73	32.01	1.92	1.50	1.75	1.75
FeO	16.16	16.23	9.32	9.52	12.67	12.11	12.73	13.51	2.17	3.44	2.78	2.90
MnO	0.58	0.61	0.25	0.25	0.40	0.42	0.40	0.42	0.00	0.09	0.00	0.05
MgO	14.40	14.23	20.70	20.61	17.63	17.55	17.79	16.54	16.98	17.05	18.35	18.22
NiO	0.03	0.09	0.24	0.25	0.20	0.12	0.06	0.03	-	-	-	-
CaO	-	-	-	-	-	-	-	-	11.90	12.19	12.06	12.13
Na2O	-	-	-	-	-	-	-	-	2.61	2.62	3.16	3.05
K2O	-	-	-	-	-	-	-	-	0.02	0.03	0.00	0.00
ZnO	0.26	0.28	0.33	0.38	0.26	0.31	0.16	0.24	-	-	-	-
VO	0.26	0.20	0.14	0.17	0.20	0.21	0.13	0.08	-	-	-	-
TOTAL	99.86	100.06	100.68	100.38	100.39	99.91	100.45	99.65	95.18	94.35	96.26	96.30
Mg#	0.65	0.62	0.823	0.823	0.748	0.745	0.733	0.711	0.933	0.919	0.955	0.978
Cr#	0.49	0.51	0.178	0.178	0.320	0.322	0.341	0.370				

5.1 Garnet/spinel peridotite

Olivine

Olivine appears in two different textures named olivine M1(a-b) porphyroclasts and olivine M2 foam microstructure (Tab. 5.1; Tab. A1.1). All olivines are forsterite in composition (Fig. 5.2) with a Mg# = 0.90-0.94.

Within garnet peridotite both M1 and M2 olivines can usually be found. They are characterised by a high Mg#, ranging from 0.905 to 0.925 (Fig. 5.1) and NiO (wt.%) content ranging from 0.33% to 0.46%. No sensible difference in composition is observed between the Mg# of M1 and M2 olivines. Within the spinel dunite, only the olivine M2 foam microstructure is found. This olivine is characterised by a very high Mg#, ranging between 0.925 and 0.935 (Fig. 5.1) and NiO (wt.%) content ranging from 0.38% to 0.45%.

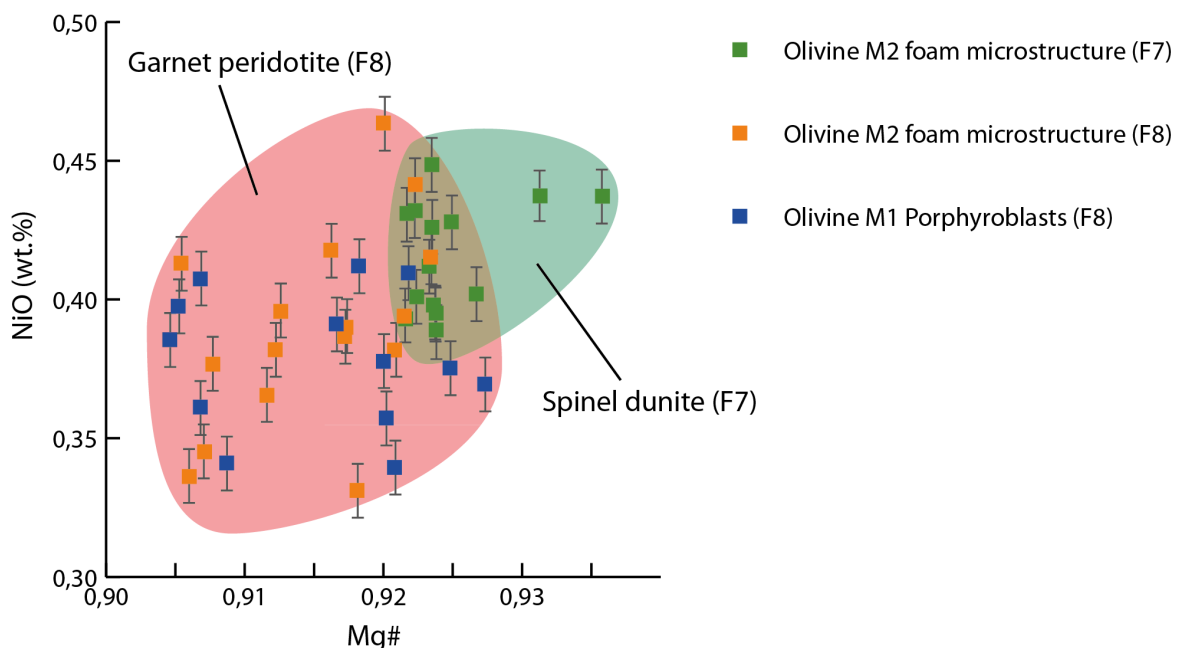


Fig. 5.1 - NiO (wt. %) VS Mg# for olivine in different textures and rock types. Note the higher Mg# and relatively high NiO content in the olivines from the dunite. Vertical bars represent the error ($\pm 5\%$) of the EMPA for NiO.

Orthopyroxene

Representative opx mineral compositions are given in Tab. 5.1. Within garnet peridotite (F8), three different opx are found. The M1a prophyroclasts, the M1b opx from the spl-opx-parg symplectite after grt1 and the M2 opx in equilibrium with the M2 olivine "foam" microstructure. Within dunite (F7), M2 opx is often associated with spl in clusters and is in equilibrium with the olivine foam microstructure. All opx are enstatite in composition (Fig. 5.2a) with a Mg# = 0.90-0.94.

The M1 and M2 opx composition in garnet peridotite (F8) is fairly monotonous and no significant chemical variation is noticed between the two generations (Fig. 5.2a). The Al content is constant (0.4-0.6 p.f.u.) between M1 and M2 opx in the garnet peridotite (F7) and M2 opx in the dunite (F7; Fig. 5.3). However, M1b opx shows a higher Al(p.f.u.) with respect to other opx generations (M1 and M2 in GP). Opx from dunite (F7) has a higher Mg# with respect to opx from the garnet peridotite (F8).

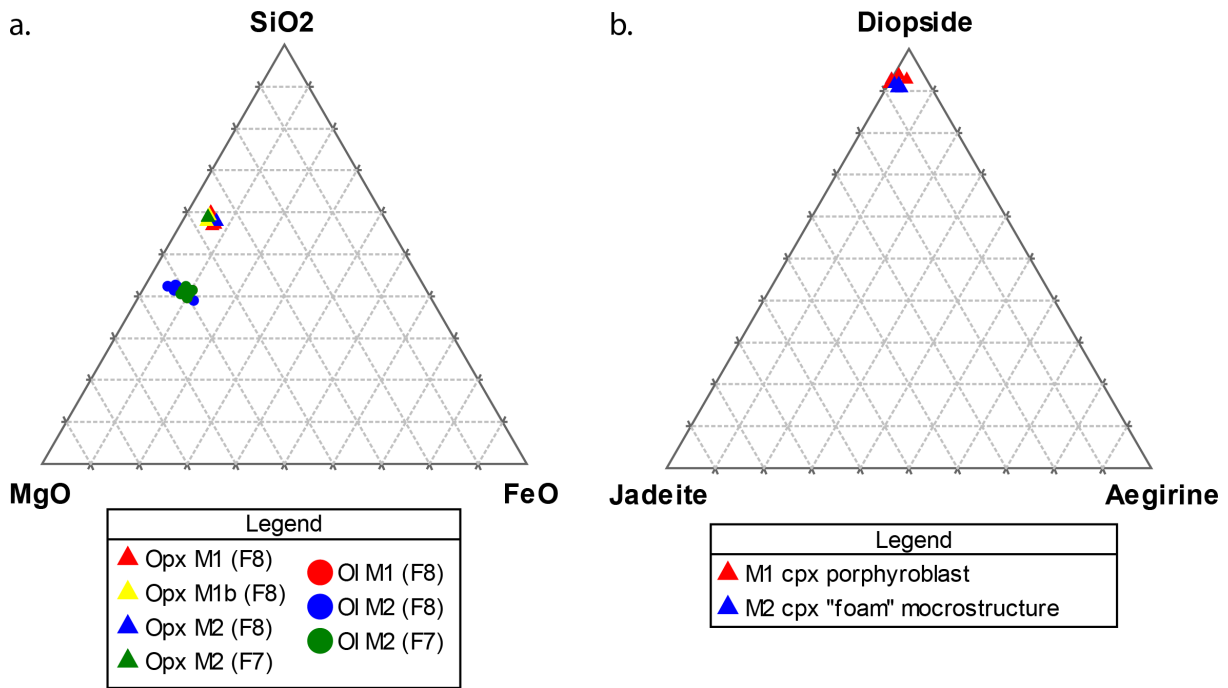


Fig. 5.2 - (a.) Triangular MgO-SiO₂-FeO diagram indicating olivine (Forsterite-Fayalite) and orthopyroxene (Enstatite-Ferrosilite) composition in different microstructure and lithology. (b.) Clinopyroxene compositions plotted on a triangular Diopside-Jadeite-Aegirine diagram. All Cpx are diopside in composition.

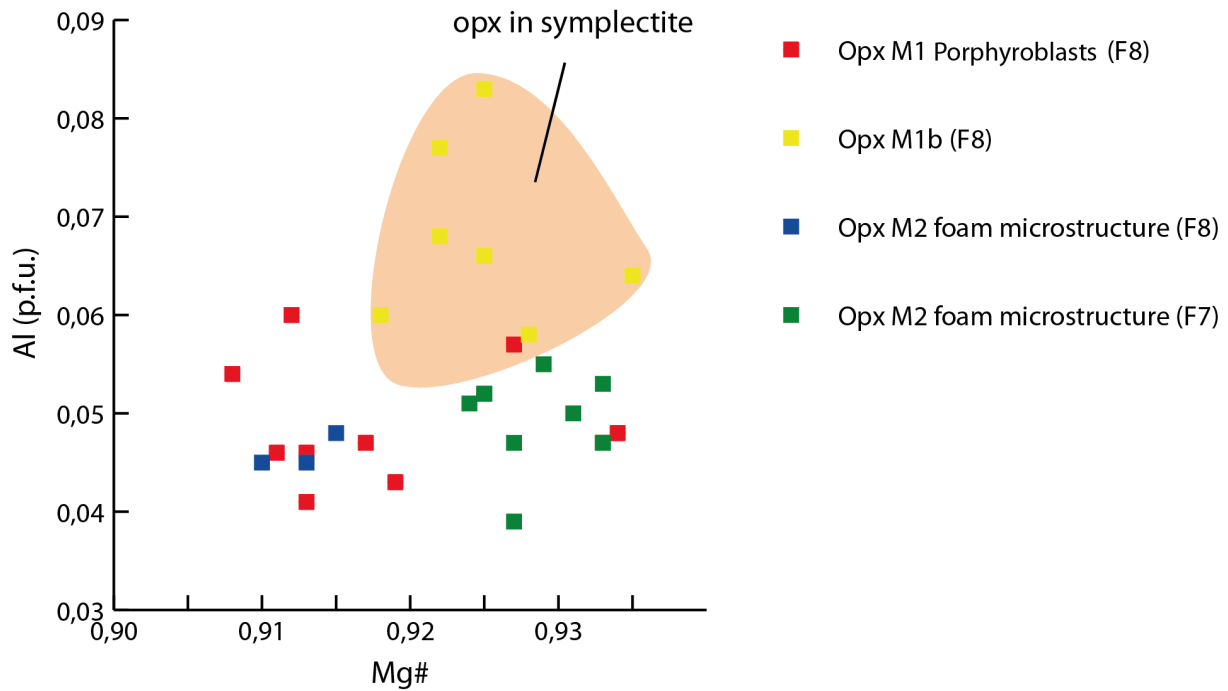


Fig. 5.3 - Al (p.f.u.) VS Mg# for orthopyroxene in different textures and rock types. Note the higher Mg# in the opx from the dunite and the high Al (p.f.u) and high Mg# in the M1b opx.

Clinopyroxene

Within the garnet peridotite, two structurally different cpx are found, called M1 porphyroblast and M2 cpx “foam” microstructure. Representative compositions of cpx are given in Tab. 5.1. No significant variation in composition is observed between the two generations of cpx. All Cpx have a diopside composition (Fig. 5.2b).

Garnet

Two generations of garnet grt1 (M1) and grt2 (M2). Grt1 consists of partially re-equilibrated crystals of around 5-15 mm in diameter. These crystals have a composition of prp~67%, alm+sps~20%, grs~6% and uvt~6-7%. This composition is fairly constant throughout the crystal and no crystal zoning has been observed (line-scan in Fig. A---). Grt2 statically grows over the poly-mineralic cloth formed after grt 1 and in the rims around the large globular spinels (Fig. 4.3). Grt2 has generally the same composition in term of prp and alm+sps than grt1. However, its grs content increases to values around 7-9% and its uvt content decreases to around 2-3%. Furthermore, exsolved garnet lamellae are found within M1 opx and cpx. While exsolved grt lamellae within opx have roughly the same composition as grt2, lamellae within cpx show a much lower prp content (Fig. 5.4).

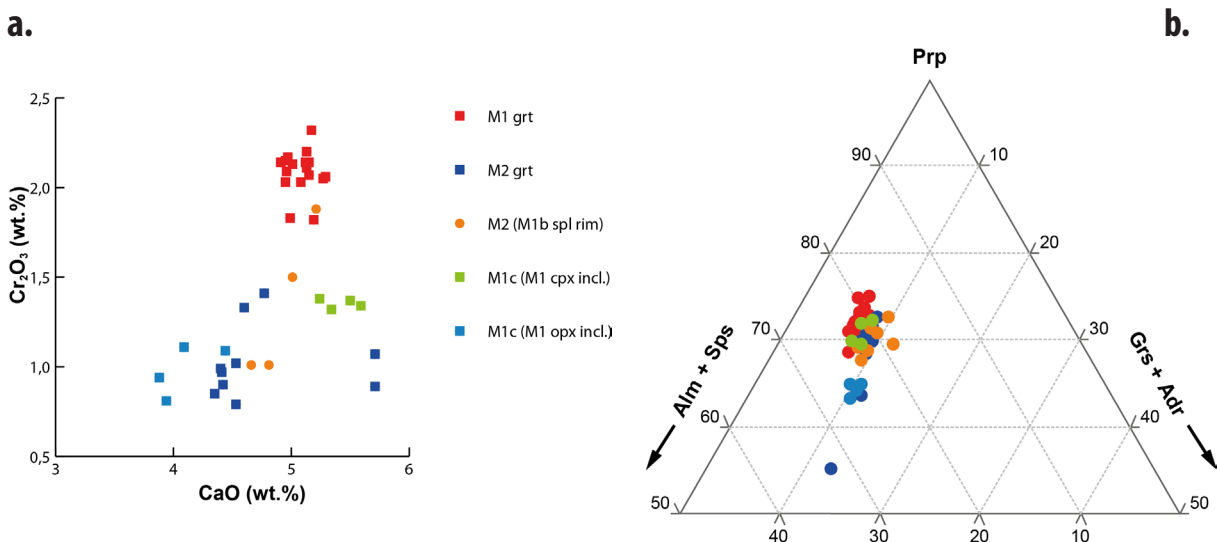


Fig. 5.4 - (a.) CaO (wt.%) VS Cr₂O₃ (wt.%) chart of the different garnet generations. Note the relatively higher Cr₂O₃ content (1.8-2.4 %) of M1 grt. The M2 grt, instead, is characterised by lower Cr₂O₃ content (0.8-1.5%) and fairly scattered CaO content (4.5-5.8%). (b.) Triangular end-member diagram of garnet with the variation of the normalised amounts of prp, grs+adr and alm+sps for the different garnet generations. All grt generations but grt in cpx have similar compositions (prp 67-75%, alm+sps 18-24% and grs+adr 6-12%). Grt in cpx has generally lower prp (64-65%), higher alm+sps content (25-26%) and constant grs+adr (10-11%). *N.B.:* amounts in (b.) are normalised on the total prp+alm+sps+adr+uvt.

Spinel

Spinel can be found in garnet lherzolite and in spinel dunite. Representative analyses of M1b and M2 spinels (sample F8) and M2 spinels from sample F7 are shown in Tab. 5.1. Other spinel analyses are shown in Tab. A1.4. In garnet peridotite (sample F8) two generations of spinel are found. The first generation consists of large (0.5-2 mm) globular M1b spinels, found around symplectites after M1a garnet. The zoning found in these spinels is associated with a relative increase of Cr# and a decrease of Mg# towards the rim in contact with M2 garnet (Fig. 5.5). The second generation is characterised by tiny and unzoned spinel inclusions (30-40 µm) inside the symplectite all in direct contact with M2 garnets.

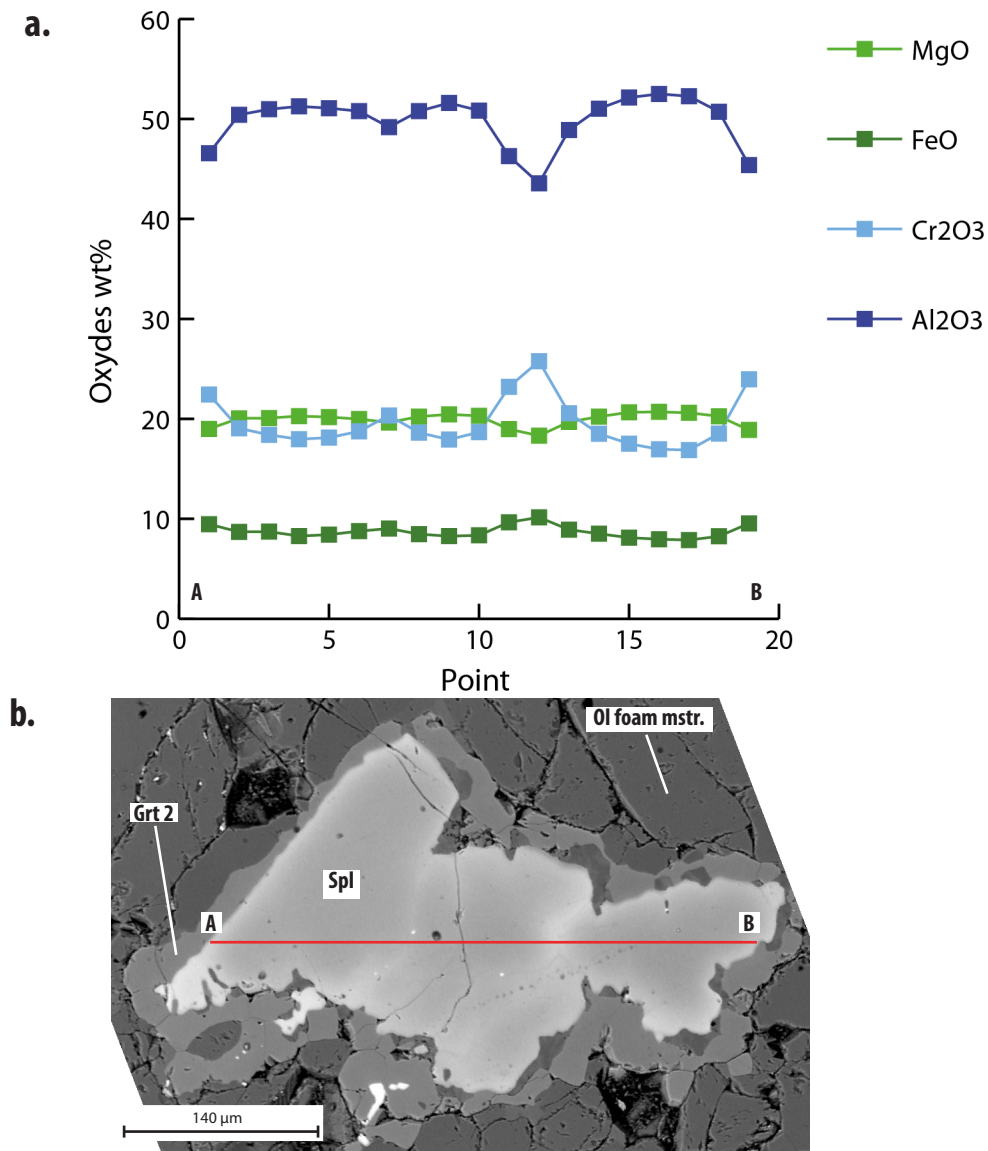


Fig. 5.5 - (a.) line-scan (A-B) across a globular M1b spinel. Note how in the rims the relative amounts of Al_2O_3 and MgO decrease and Cr_2O_3 and FeO increase. **(b.)** BSE image illustrating the range of the (A-B) EMP line-scan (red line) between point A and B (F8). This chemical variation can be seen in the micrograph as bright halos at the rim of the spinel. Furthermore, note in this picture the grt rim around the M1b spinel.

In Spinel dunite (sample F7) spinels are unzoned and usually associated with opx in clusters (Fig. F7-1 in the appendix). M2 spinels in dunite (F7) are characterised by a relative high Cr# (0.46-0.51) and a low Mg# (0.61-0.66). Fig. 5.7 shows the relationship between Cr# and Mg# of different spinel generations in different lithologies. M2 Spinel from dunite (green triangle) have a really high Cr# and plot at the boundary between spinel s.s. and Mg-chromite (Fig. 5.7). Instead, spinels from garnet peridotite have much lower Cr# (especially in the core of large M1b spinels). This, however, progressively increases to higher Cr# values within later M2 spinel generations. As Cr# increases, Mg# decreases linearly (Fig. 5.7). As can be seen from the graph in Fig. 5.6b, oxidation state of Fe is generally higher in dunite ($\text{Fe}^{3+} \sim 0.03$ p.f.u.) and lower in peridotite ($\text{Fe}^{3+} \sim 0.01$ -0.02 p.f.u.). Aside few values of scale, TiO_2 (wt%) amount do not vary between the two lithologies.

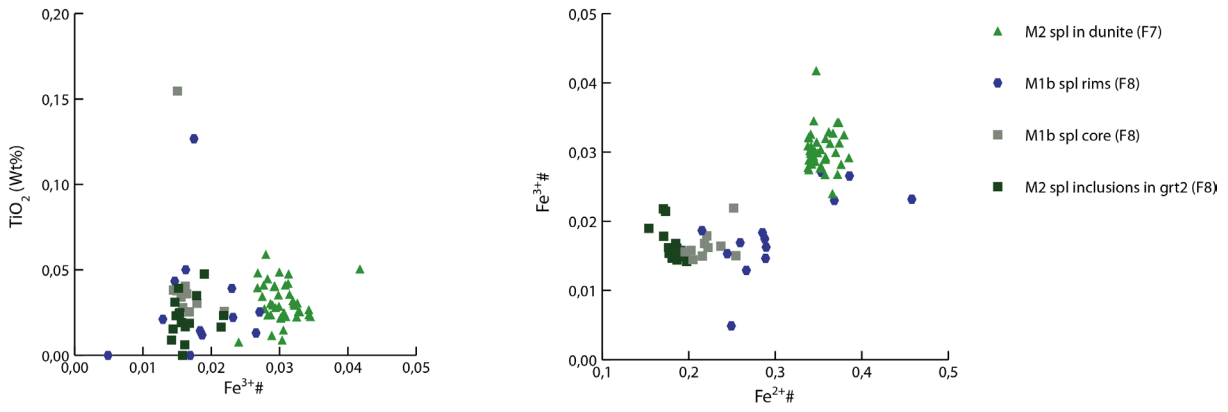


Fig. 5.6 - (a.) Fe³⁺ Vs TiO₂ (wt%) of M1 and M2 spinels from section F8 and M2 spinels from sample F7. Note the independence of TiO₂ from texture and lithology. (b.) Fe²⁺ VS Fe³⁺ of M1 and M2 spinels from section F8 and M2 spinels from sample F7. The overall iron amount in M2 spinel from dunite (F7) is higher than from peridotite but the ratio between the two oxidation states is fairly constant. In the garnet peridotite, the spinel generations can be differentiated by the Fe²⁺ amount. The amount of Fe³⁺ is, instead, quite constant.

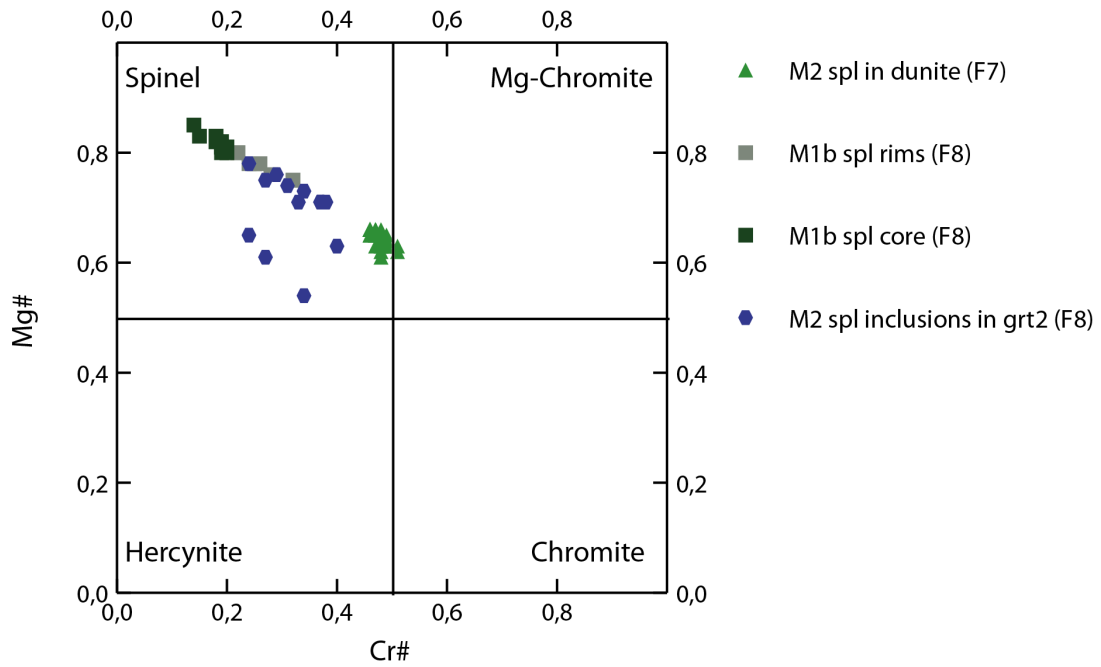


Fig. 5.7- Spinel classification diagram Cr# Vs Mg# of M1 and M2 spinels from section F8 and M2 spinels from sample F7 (). Note the Cr# is inversely proportional to the Mg#.

Amphibole and other minerals

EMP mineral compositions of representative amphiboles are shown in Tab. 5.1 and in Tab. A1.5. All analysed amphiboles are classified as pargasite according to the classification system by Leake *et al.* (1997).

Several minor phases like rutile and Fe-Ni sulfides (Fig. 4.11) has been found in garnet peridotite (F8) and dunite (F7). In particular, these sulfides were used by Brueckner *et al.* (2004) to infer the age of the partial melting. Trains of mono- and multi-phase solid and fluid inclusions found within M1 mineral assemblages are mainly composed of Sr-bearing carbonates (mainly magnesite and dolomite) and rare diopside (Fig. 4.2c).

5.2 Eclogite

Table 5.2. Representative major elements oxides of mineral compositions in eclogite sample (F6).

	Grt core	Grt rim	omp	zoi	dol
N°	11	1	3	7	8
SiO ₂	40.78	41.27	52.28	40.56	1.70
Al ₂ O ₃	22.74	22.66	8.09	30.32	0.01
FeO	12.65	14.99	1.97	2.57	1.31
MnO	0.26	0.40	0.02	0.10	0.13
MgO	12.63	12.00	12.50	2.89	22.34
CaO	10.07	8.92	20.34	15.09	31.36
NaO	-	-	2.73	0.63	0.01
TiO ₂	0.02	0.02	0.24	0.00	0.01
Cr ₂ O ₃	0.07	0.04	0.14	0.02	0.06
NiO	0.04	0.00	0.02	-	-
Totals	99.26	100.31	98.33	92.18	57.16

Garnet

Two generations of garnet grt1 (M1) and grt2 (M2). Grt1 consists of large, slightly elongated blasts, completely replaced by smaller grt2 (Fig. 4.6), containing inclusions of ky, zoi, Mg-Fe carbonates and omph. Grt2 consists of small, euhedral, inclusion-free crystals within the matrix. Grt2 composition is fairly homogeneous throughout the crystal (prp~47%, alm+sps~27%, grs+adr~26% and uvt <0.5%), only the edges of the crystal show a slight decrease in CaO and MgO and an increase in FeO (line-scan in Fig. 5.8a-b). Conversely, Al₂O₃ remains constant throughout the grt line-scan.

Clinopyroxene

Large and deformed M1 clinopyroxenes, reported by Verbaas & Van Roermund (2012), were not found in the eclogite sample (F6). Clinopyroxene occurs as small, euhedral and strain-free crystals. A representative cpx composition is shown in Tab. 5.2. Cpx composition fall at the border line between omphacite and diopside (Jd content = 18-22%; Fig. 5.9a). Their Jd content is slightly lower than the cpx reported in Janàk *et al.* (2013), coming from a sample from the same location. Cpx in the matrix is, usually, partially overprinted at the rims by a diopside + plagioclase symplectite. Furthermore, cpx occurs within small multiphase inclusions within M1 garnet.

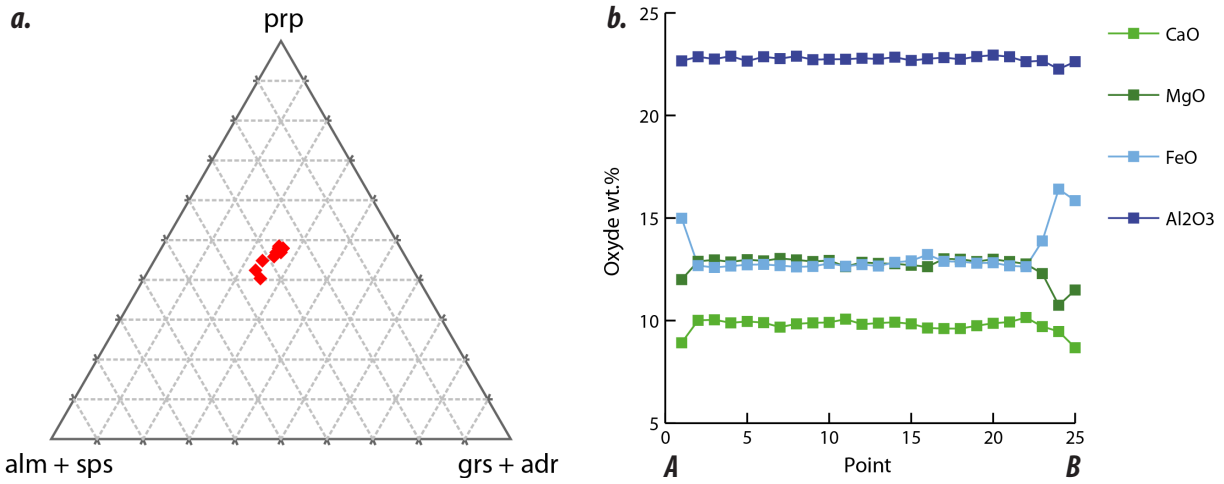


Fig. 5.8 - (a) Triangular end-member diagram of M2 garnet within eclogite (F6) showing the variation of the normalised amounts of prp, grs+adr and alm+sps. (b) line-scan (A-B) across a M2 grt in eclogite (F6). Note how in the rims the relative amounts of Al₂O₃ remain constant, MgO and CaO decrease and FeO increases. The position of the line-scan is indicated in fig. 4.6.

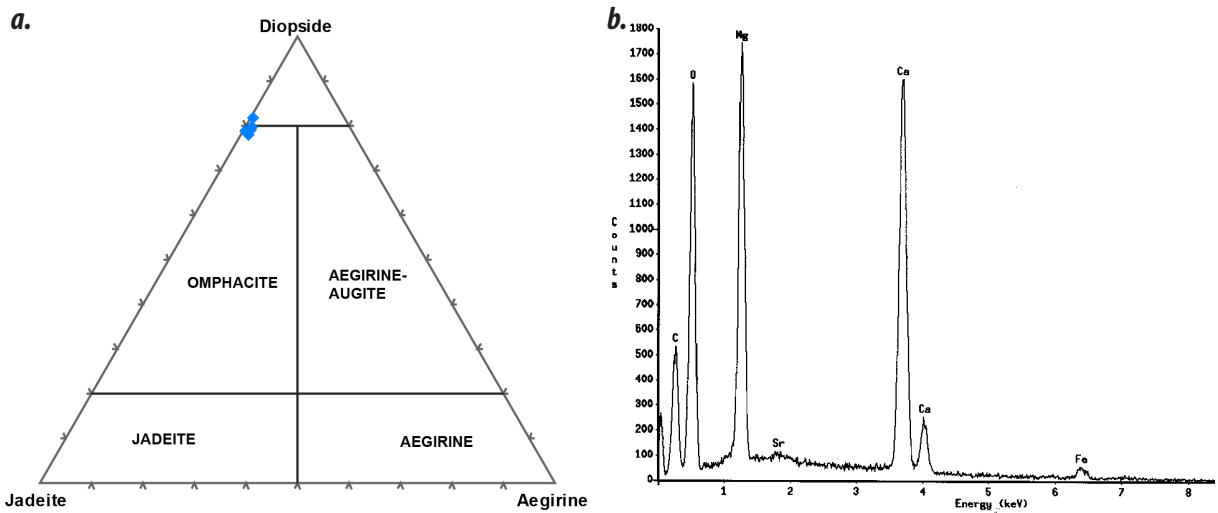


Fig. 5.9 - (a) Triangular end-member diagram of clinopyroxene within eclogite (F6) showing the variation of the normalised amounts of diopside, jadeite and aegirine. (b) ED spectrum of dolomite in the eclogite (F6). Note the small peak of Sr around 2 keV.

Other minerals

Secondary minerals consist of Fe-Mg-Ca carbonates, kyanite, phengite, zoisite and rare rutile. Dolomite occurs as small, subhedral, crystals within the matrix (Fig. 4.7b) and as small, rounded multiphase inclusions within M1 garnet, usually associated with other carbonates, diopside, zoisite and kyanite ± phengite. Several dolomite crystals in the matrix display partial rims of calcite (Fig. 4.7b). A typical ED spectrum for dolomite is shown in Fig. 5.9b. Note the small Sr peak around 2 keV.

Kyanite and zoisite occur as small needles within M1 garnet. Rutile occurs as small rounded inclusions in M1 garnets.

5.3 Geothermobarometry

In ultramafic rocks, classical geothermobarometers are divided into two subgroups called single crystal and ion exchange. Single crystal geothermobarometers are based on the fact that the relative compatibility of an element varies according to P and T. Examples are the Cr-in-cpx barometer and the Ni-in-garnet thermometer. In contrast, ion exchange geothermobarometers work on the ion equilibria between two different minerals. Examples are the Fe-Mg exchange between ol-spl, ol-grt, opx-cpx (solvus geothermometer) and the Cr-Al exchange between spl and opx. Geothermobarometers for HP (ultra-)mafic rocks are listed and discussed in Krogh Ravna & Paquin (2003) and in Brey *et al.* (2008).

In this work, the opx-cpx solvus geothermometer and the Al-in-opx barometer have been used to constrain the PT conditions of the early M1a mineral assemblage.

In order to constrain the PT conditions of post-M1a mineral assemblages, the thermometers based on Fe-Mg exchange between ol-spl, ol-grt, cpx-grt and opx-grt, on Na between opx-cpx and Ca between ol-cpx have been used (Nickel & Green, 1985; Ryan *et al.*, 1996; Brey & Köhler, 1990; Taylor, 1998; Brey *et al.*, 2008).

5.3.1 EMP mapping using a defocussed beam

Most of the HT M1a minerals contain exsolution lamellae or, in the case of grt1, have been partially overprinted by “low” T mineral assemblages. It is assumed here that the overall composition of M1a minerals did not change and can therefore be considered as a closed system, at least for Fe, Mg, Ca, Al and Si. Solid inclusions within M1a minerals indicate that an interaction occurred with COH-bearing fluids. For example, most of the Na is interpreted to be brought in by subduction derived fluids. It has been reduced to 1/3 in the analysis of opx, it has been modified in cpx in order to obtain a sum of 4.000 atoms p.f.u. and it has been considered zero in the analysis of garnet. This method was already discussed for similar purposes by Carswell and Van Roermund (2005) and by Spengler (2006) who analysed HT opx crystals from Bardane and Otrøy, Norway.

An EMP technique was applied in order to analyse the bulk chemistry of the original M1a opx, cpx and grt. The spot of the electron beam was “widened” to 10 µm giving a total interaction volume of about 2-3 µm³. Several line scans were performed on M1a phases with a spacing of 12 µm between each line and/or between each analysis. Each analysis represents the composition either of one phase, or a composite of more than one.

Well preserved areas of grt, cpx and opx have been selected in order to apply this technique (Section F8A). Four line scans of 30 points were performed on opx (4.32*10⁻⁵ mm³) and three line scans of 30 points on grt and cpx (3.24*10⁻⁵ mm³). Results are listed in Tab. 5.3.

Table 5.3. Results of chemical integration using defocussed EMP mapping. Defocussed analysis decreases the precision of the instruments. The error is estimated to be about $\pm 5\%$ (see Chap. 3). *Na content has been modified (see text).

	Garnet 1		Cpx 1		Opx 1	
	Wt %	Atoms p.f.u.	Wt %	Atoms p.f.u.	Wt %	Atoms p.f.u.
SiO ₂	40.36	3.020	49.60	1.896	52.26	1.882
TiO ₂	0.27	0.015	0.26	0.007	0.08	0.002
Al ₂ O ₃	20.57	1.814	4.11	0.185	4.65	0.197
Cr ₂ O ₃	2.06	0.122	1.12	0.034	0.44	0.013
FeO	8.30	0.519	2.14	0.068	6.34	0.191
MnO	0.37	0.024	0.08	0.003	0.16	0.005
MgO	17.95	2.002	16.22	0.924	31.28	1.680
NiO	0.03	0.002	0.03	0.001	0.06	0.002
CaO	5.99	0.480	20.84	0.854	0.98	0.038
Na ₂ O	0.74	0.000*	1.29	0.027*	0.16	0.003*
Totals	96.64	7.997	95.70	4.000	96.41	4.012

5.3.2 Results

The M1a assemblage

PT conditions of the M1a assemblage have been estimated using the mineral compositions listed in Tab. 5.3. The opx-cpx solvus geothermometers calibrated by Brey & Köhler (1990) give a temperature around 1000-1100 °C, slightly increasing with increasing P. The calibration of Taylor (1998) gives slightly higher results ($T \sim 1250$ °C). The three different versions of the Al-in-opx barometer, calibrated by Nickel & Green (1985), Brey & Köhler (1990) and Brey *et al.* (2008) give pressure of 2.1 ± 0.2 , 1.8 ± 0.2 and 1.7 ± 0.2 GPa respectively (T preset = 1125°C). The Cr-in-grt geobarometer (Ryan *et al.*, 1996) gives exceptionally high pressure results ($P > 2.5$ GPa) for the same T interval. For this reason it will be ignored. Geothermobarometry results for the M1a assemblage are summarized in Tab. 5.4.

A combination of the used geothermobarometers is illustrated in Fig. 5.10 by the shaded area. This area indicates that the M1a assemblage formed in between 1050-1200°C and 1.5-2.3 GPa.

Table 5.4. List of used geothermobarometers for the M1a mineral assemblage and results (presets*: $T=1125^\circ\text{C}$ and $P=1.9$ GPa).

Geothermobarometer		T (°C; preset*)	P (GPa; preset*)	References
P [RGP96]	Cr in Garnet	1125*	2.8 ± 0.3	Ryan <i>et al.</i> (1996)
P [NG85]	Al in Opx	1125*	2.1 ± 0.2	Nickel & Green (1985)
P [BBG08]	Al in Opx	1125*	1.7 ± 0.2	Brey <i>et al.</i> (2008)
P [BKN90]	Al in Opx	1125*	1.8 ± 0.2	Brey & Köhler (1990)
T [Taylor98]	Opx-Cpx Solvus	1250 ± 15	1.9*	Taylor (1998)
T [OpxBK90]	Opx-Cpx Solvus	1081 ± 15	1.9*	Brey & Köhler (1990)
T [BKN90]	Opx-Cpx Solvus	1019 ± 15	1.9*	Brey & Köhler (1990)

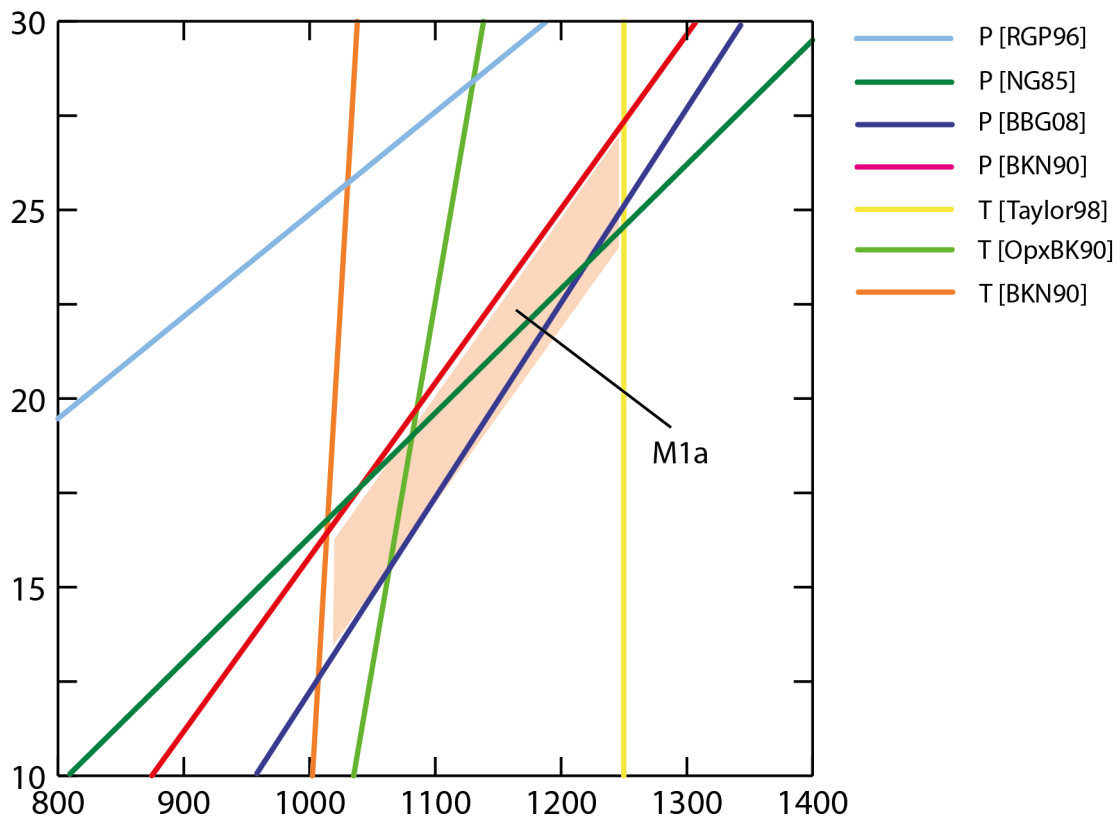


Fig. 5.10 - Geothermobarometry of the M1a mineral assemblage. The used geothermometers and geobarometers, except [RGP96], imply a $T = 1125 \pm 75^\circ\text{C}$ and a $P = 1.9 \pm 0.4 \text{ GPa}$ (references in Tab. 5.4).

Post-M1a mineral assemblages

PT condition of the post-M1a mineral assemblages in garnet peridotite (F8) have been estimated using the compositions outlined in Tab. A1.1-A1.5 (M1a: ol 19, opx 5, cpx 8, grt 8; opx 5, grt 39; cpx 8, grt 35; ol 32, opx 13, cpx 9, grt 21, spl 37). In thermometers involving M1b spl, analysis 66 and 46 (Tab. A1.4) for M1b spl core and rim respectively have been used. These two spl analyses has been chosen for their contrasting Cr#, low in the M1b spl core and high in the probably M2 spl rim.

In garnet peridotite, Fe-Mg exchange in M1 ol and M1b spl cores gives high temperatures: 1085 ± 60 (O'Neill & Wall, 1987) and $1164 \pm 60^\circ\text{C}$ (Ballhaus *et al.*, 1991). The same set of geothermometers, applied to M1b spl rims and/or M2 spl, gives T of 765 ± 60 and $799 \pm 60^\circ\text{C}$ respectively.

The M2 metamorphic conditions (3.0 GPa - 800°C) found by Janàk *et al.* (2013) are used here as a comparison to the geothermobarometric results. Geobarometers involving Al content in opx (Nickel & Green, 1985; Brey & Köhler, 1990; Brey *et al.*, 2008) give pressure between 2.1 and 2.8 GPa for the M1a mineral assemblage, 2.4 and 2.8 GPa for the M1a (opx-grt exsol.) and 2.7 and 2.9 for the M2 mineral assemblage (Tab. 5.6; Fig. 5.11).

Geothermometers applied on M1a, M2 and opx/cpx + grt exsolution shows two age clusters (Tab. 5.6; Fig. 5.11). Several thermometers involving Fe-Mg exchange between cpx and grt (Ellis & Green, 1979; Powell, 1985), Fe-Mg exchange between opx and grt (Harley, 1984), Na content in opx-cpx (Brey & Köhler, 1990), Fe-Mg exchange between ol and spl (O'Neill & Wall, 1987, Ballhaus *et al.*, 1991) and Al content in opx-spl (Witt-Eickschen & Seck,

1991) gives temperatures within the $800 \pm 60^\circ\text{C}$ range (concordant with M2 PT estimates of Janàk *et al.*, 2013). Other thermometers, used on the same mineral assemblages, involving Fe-Mg exchange between cpx and grt (Krogh, 1988; Krogh Ravn, 2000; Nakamura & Hirajima, 2005) and Fe-Mg exchange between ol and grt (O'Neil & Wood, 1979), gives lower temperatures, between 600 and 720°C . Geothermobarometry results for the M1a and M2 mineral assemblage in garnet peridotite (F8) are summarized in Tab. 5.6.

PT condition of the post-M1a assemblage in dunite (F7) have been estimated using the compositions from Tab. A1.1-A1.5 (opx 27; ol 2). In thermometers involving olivine and spl, an average composition of M2 spl has been used (P preset = 3.0 GPa). The Fe-Mg in spl-ol (O'Neill & Wall, 1987; Ballhaus *et al.*, 1991) geothermometers gives T around $634 \pm 60^\circ\text{C}$. The Zn in spl geothermometer (Ryan *et al.*, 1996) shows T around $660 \pm 30^\circ\text{C}$. Geothermobarometry results for the M2 mineral assemblage in dunite (F7) are summarized in Tab. 5.7.

Table 5.5. List of used geothermobarometers for the M1b mineral assemblage in garnet peridotite (F8) and results. pressure is set at P = 1.5 GPa.

Geothermobarometer		T (°C)	Assemblage	References
T [OW87]	Fe-Mg between ol and spl	1085 ± 60	M1b spl core	O'Neill & Wall (1987)
		765 ± 60	M1b spl rim	
T [Ballhaus91]	Fe-Mg between ol and spl	1164 ± 60	M1b spl core	Ballhaus <i>et al.</i> (1991)
		799 ± 60	M1b spl rim	

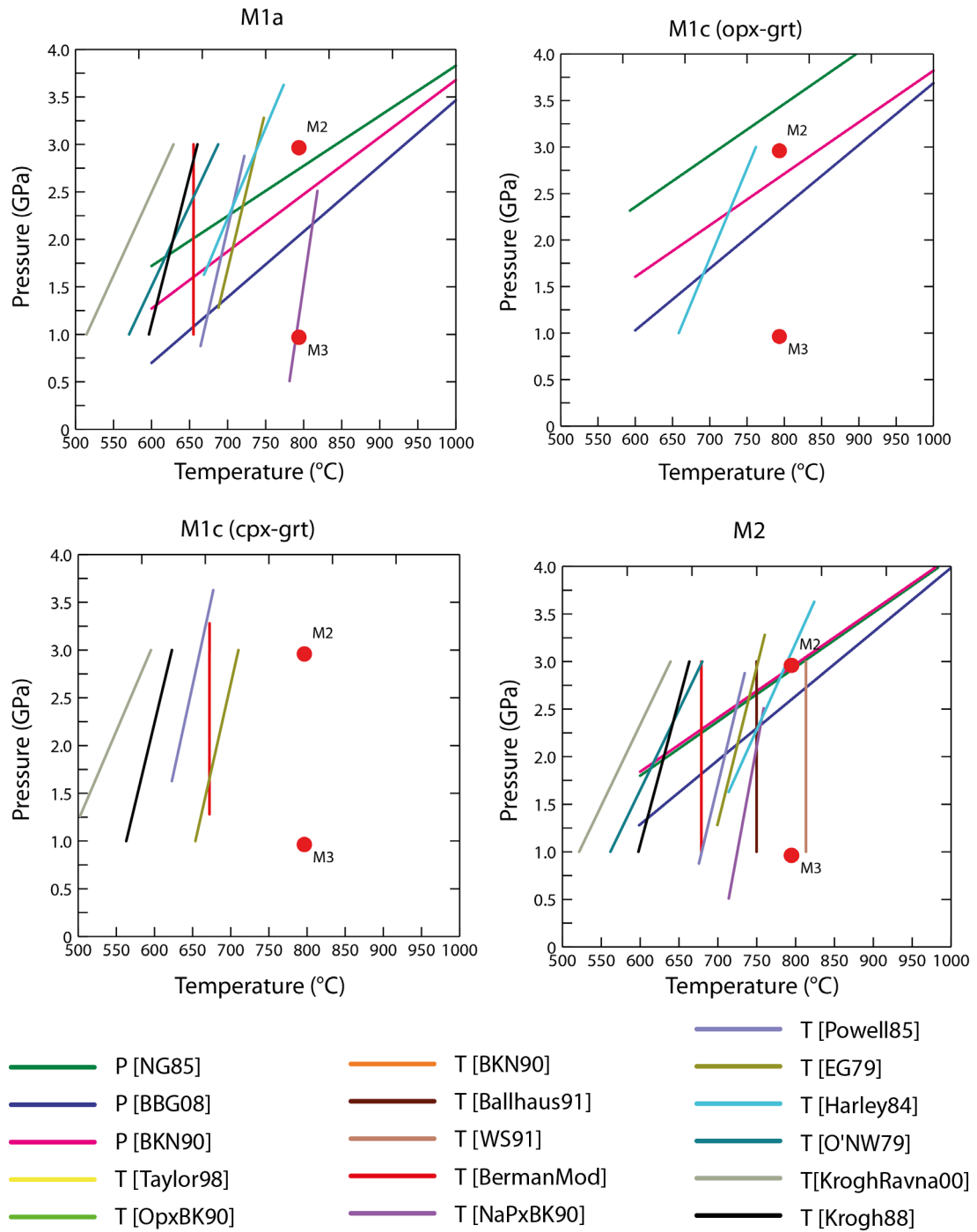


Fig. 5.11 - Geothermobarometry of the M1a and M2 mineral assemblage and opx and cpx plus associated grt exsolution (M1c). The red dots are the PT results of Janák *et al.* (2013) for the M2 and M3 mineral assemblage in eclogite. (references in Tab. 5.5).

Table 5.6. List of used geothermobarometers for the M1a and M2 mineral assemblage and for M1a opx and cpx plus their grt exsolution lamellae (M1c) in garnet peridotite (F8) and results. Pressure is set to $P = 3.0$ GPa according to the results of Janák *et al.* (2013) for the M2 mineral assemblage in eclogite.

Geothermobarometer		T (°C; *preset = 800°C)	P (GPa; *preset = 3.0 GPa)	Assemblage	References
P [NG85]	Al in Opx	*	2.8 ± 0.2	M1a	Nickel & Green (1985)
P [BBG08]	Al in Opx	*	2.1 ± 0.2	M1a	Brey <i>et al.</i> (2008)
P [BKN90]	Al in Opx	*	2.4 ± 0.2	M1a	Brey & Köhler (1990)
T [NaPxBK90]	Na between Opx-Cpx	826 ± 60	*	M1a	Brey & Köhler (1990)
T [EG79]	Fe-Mg between cpx and grt	754 ± 60	*	M1a	Ellis & Green (1979)
T [Powell85]	Fe-Mg between cpx and grt	729 ± 60	*	M1a	Powell (1985)
T [Beerman95MOD]	Fe-Mg between cpx and grt	655 ± 60	*	M1a	Nakamura & Hirajima (2005)
T [O'NW79]	Fe-Mg between ol and grt	688 ± 60	*	M1a	O'Neil & Wood (1979)
T [Harley84]	Fe-Mg between opx and grt	781 ± 60	*	M1a	Harley (1984)
T [KroghRavna00]	Fe-Mg between cpx and grt	629 ± 60	*	M1a	Krogh Ravna (2000)
T [Krogh88]	Fe-Mg between cpx and grt	660 ± 60	*	M1a	Krogh (1988)
P [NG85]	Al in Opx	*	2.8 ± 0.2	M1a (opx)	Nickel & Green (1985)
P [BBG08]	Al in Opx	*	2.4 ± 0.2	M1a (opx)	Brey <i>et al.</i> (2008)
P [BKN90]	Al in Opx	*	2.7 ± 0.2	M1a (opx)	Brey & Köhler (1990)
T [Harley84]	Fe-Mg between opx and grt	762 ± 60	*	M1a (opx)	Harley (1984)
T [EG79]	Fe-Mg between cpx and grt	710 ± 60	*	M1a (cpx)	Ellis & Green (1979)
T [Powell85]	Fe-Mg between cpx and grt	684 ± 60	*	M1a (cpx)	Powell (1985)
T [Beerman95MOD]	Fe-Mg between cpx and grt	598 ± 60	*	M1a (cpx)	Nakamura & Hirajima (2005)
T [KroghRavna00]	Fe-Mg between cpx and grt	595 ± 60	*	M1a (cpx)	Krogh Ravna (2000)
T [Krogh88]	Fe-Mg between cpx and grt	623 ± 60	*	M1a (cpx)	Krogh (1988)
P [NG85]	Al in Opx	*	2.9 ± 0.2	M2	Nickel & Green (1985)
P [BBG08]	Al in Opx	*	2.9 ± 0.2	M2	Brey <i>et al.</i> (2008)
P [BKN90]	Al in Opx	*	2.7 ± 0.2	M2	Brey & Köhler (1990)
T [OW87]	Fe-Mg between ol and spl	766 ± 60	*	M2	O'Neill & Wall (1987)
T [Ballhaus91]	Fe-Mg between ol and spl	750 ± 60	*	M2	Ballhaus <i>et al.</i> (1991)
T [WS91]	Al in opx-spl	813 ± 60	*	M2	Witt-Eickschen & Seck (1991)
T [O'NW79]	Fe-Mg between ol and grt	680 ± 60	*	M2	O'Neil & Wood (1979)
T [Harley84]	Fe-Mg between opx and grt	831 ± 60	*	M2	Harley (1984)
T [KroghRavna00]	Fe-Mg between cpx and grt	639 ± 60	*	M2	Krogh Ravna (2000)
T [Krogh88]	Fe-Mg between cpx and grt	663 ± 60	*	M2	Krogh (1988)
T [EG79]	Fe-Mg between cpx and grt	767 ± 60	*	M2	Ellis & Green (1979)
T [Powell85]	Fe-Mg between cpx and grt	741 ± 60	*	M2	Powell (1985)
T [Beerman95MOD]	Fe-Mg between cpx and grt	679 ± 60	*	M2	Nakamura & Hirajima (2005)

Table 5.7. List of used geothermobarometers for the M2 mineral assemblage in spinel dunite (F7) and results (P preset* = 1.0 GPa).

Geothermobarometer		T (°C)	Assemblage	References
T [OW87]	Fe-Mg between ol and spl	603 ± 60	M2	O'Neill & Wall (1987)
T [Ballhaus91]	Fe-Mg between ol and spl	581 ± 60	M2	Ballhaus <i>et al.</i> (1991)
T [WS91]	Al in opx-spl	783 ± 60	M2	Witt-Eickschen & Seck (1991)
T [ZnRGP96]	Zn in spl	647 ± 30	M2	Ryan <i>et al.</i> (1996)

5.3.3 Discussion

The results of the defocussed beam analyses (Tab. 5.3) is that the total sum of the elements wt% is lower than 100%. This is due to the lower accuracy of the wide beam EMP procedure with respect to the regular, well focussed 1 μm thick, beam. This error is further increased by imperfection in the sample surface. Geothermobarometry carried out using the defocussed beam technique will not be as accurate as when regular analyses are used. However, it will give a clear indication of the PT range of equilibration (low VS high P and T). These results then have to be compared with thermodynamic calculations and/or with PT conditions obtained for other mineral assemblages in order to verify their reliability.

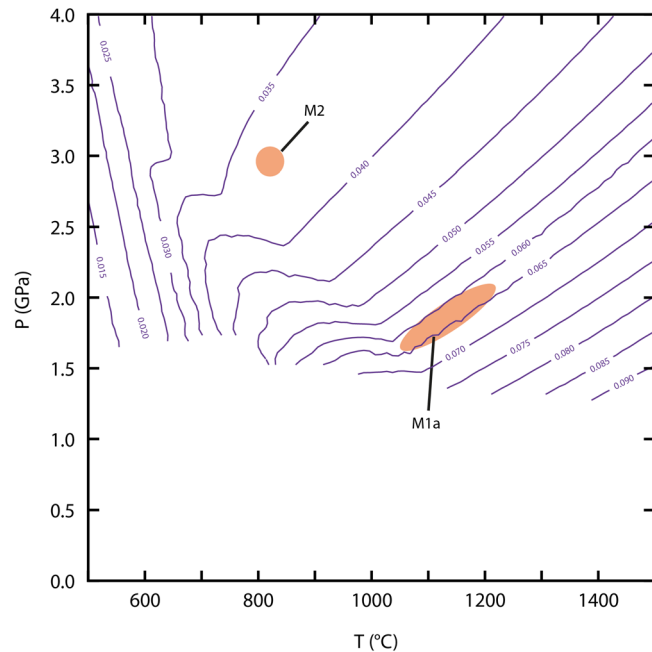


Fig. 5.12 - Isopleths for the stability of uvr in garnet. The stability fields for the different mineral assemblages are shown in light orange. M1 (1.6-2.1 GPa - 1000-1250°C; present study). M2 (3.0 GPa - 800°C; Janák *et al.*, 2013).

The M1a phases, especially the cloth after grt1, contain small amounts of pargasite. Most of the Na contained in this mineral is believed to be of metasomatic origin, introduced in the system together with small amounts of Si, Sr and COH-rich fluids. As such, the Na amount in the grt1 has not been considered and it has been reduced in the analysis of cpx and opx (sum of cations set to ~ 4.00). This technique is usually used to recalculate Fe^{3+} in EMP analyses. However, due to the highly reducing mantellic environment, Fe^{3+} has not been considered.

Recalculated grt1 mineral compositions obtained by wide beam analyses contain the same amount of Cr^{3+} as preserved grt1 (uvr $\sim 6\%$). However, amounts of Ca, Fe and Mg are different. This gives important indication of the element diffusion within garnet. Apparently, Ca, Fe and Mg, easily diffuse through the garnet and are exchanged with neighbour phases such as ol, opx and cpx at $800 < T < 1000^\circ\text{C}$. In fact, the relative amount of these elements is the same for both grt1 and grt2. Instead, Al and Cr content varies between grt1 and grt2. This implies that only little (or even none) Cr exchange occurred between different phases. This could be related to the different sites within garnet: bivalent (X^{2+}) shared between Ca, Fe^{2+} and Mg and trivalent (Y^{3+}) shared between Cr and Al.

Four barometers and three thermometers have been tested on the M1a mineral assemblage. The three different calibrations of the Al-in-opx barometer gives similar results, within 0.25 GPa between one another. The Cr-in-grt barometer give much higher results. This can be due to (1) error in the estimation of Cr or (2) the original amount of Cr content in garnet refers to an HT-HP condition. In this case, the original Cr content might have been preserved while the exchange of elements like Mg, Fe, Ca and Ni between grt and pyroxene continued in order to decrease the internal energy level. If so, the M1a mineral assemblage would represent the final stage of a near-isothermal decompression that occurred within the mantle.

The three different thermodynamic calibrations of the opx-cpx "solvus" geothermometers give all results between 1000 and 1250°C. According to the pseudosection in Fig. 4.11, for this T range, the stable mineral assemblage is always ol+opx+cpx+grt, for $P > 1.5$ GPa.

Fig. 5.12 shows isopleths for uvr in grt produced with PerpleX using the bulk rock composition of sample F8. The PT ranges for the M1a assemblage found by geothermobarometric calculation using M1a wide beam analysis coincides with the calculated isopleths for uvr 6.0-6.5 %, which represent the Cr content of M1a grt (Fig. 4.7a). Note in this diagram (Fig. 5.12) that the M2 PT found by Janàk *et al.* (2013) coincides with the calculated stability of uvr 3-4% (grt2; Fig. 4.7a).

Another indication for the temperature of the M1a assemblage is given by the study of the M1b spinel cores. Two thermometers based on the Fe-Mg exchange between M1 ol and spl composition have been used. Results are in between 1085 and 1164°C for the M1b assemblage. Assuming isothermic decompression, this must have been also the temperature range of the M1a assemblage, restricting the larger range obtained with the opx-cpx "solvus" thermometer.

M1b spl rims represent the interaction volume between the M1b spl itself with the M2 grt. Temperatures obtained using ol and M1b spl rims are therefore indicative of T during the M2 phase. Lower temperatures of 765-799°C are obtained using Fe-Mg exchange between ol and M1b spl rims. These T are concordant with the PT results for the M2 mineral assemblage in eclogite found by Janàk *et al.* (2013). However, the burial phase was probably isothermic. As such, the T results found in garnet peridotite (F8) for the M2 assemblage can be used to infer an (near-)isobaric cooling from around 1100 ± 60 °C M1b to 765-800°C ($P < 1.5$ GPa). This phase is called M1c.

The interception between the geothermometer and the geobarometer usually indicates the PT range of formation of a given mineral assemblage. However, as a mineral assemblage is re-equilibrated (i.e. element diffusion changes the composition of the mineral with respect to the original composition) the new composition will affect the thermometers and the barometer by shifting them to lower pressure and temperature (Fig. 5.13). Assuming the diffusion rate for every element in every mineral phase in a rock to be the same, the new interception line between barometer and thermometer will then indicate a PT of re-equilibration. However, diffusion rate can vary between minerals and element. Thus the shift of the calculated barometer and thermometer might not be equal (i.e. the barometer might shift faster than the thermometer or

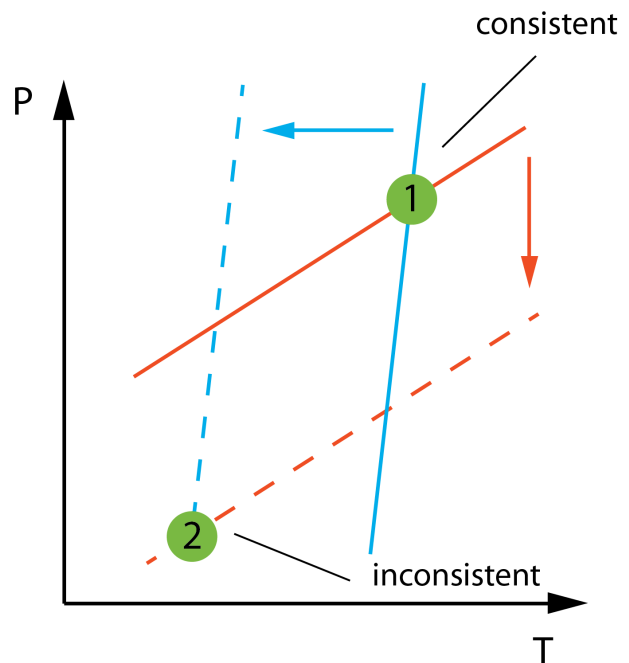


Fig. 5.13 - Shift to lower P and T of barometer (orange) and thermometer (blue). The green dot (1) indicate the consistent intercept of the barometer and thermometer, indicating original temperature and pressure. The green dot (2) gives inconsistent results because the shifting of barometer and thermometer might not be concordant.

viceversa). For example, most of the thermometer used involve Fe-Mg exchange and the barometer involve Al content in opx. It has been observed (Carswell & Harley, 1990) that the Al diffusion in opx is highly sensitive to pressure changes while Fe and Mg are more sensitive to temperature changes. In the case of the FGP, geothermobarometric results for the M2 mineral assemblage can be compared with the result of Janàk *et al.* (2013) for the eclogitic dike in order to evaluate their reliability.

Several geothermometers and geobarometers on the M1b and M2 mineral assemblage give consistent results with the PT estimates of Janàk *et al.* (2013). This is indicative of a strong metamorphic overprint of the M1 mineral assemblage (except for the M1b spl core) during the M2 metamorphic event. However, the pressure indicated by the barometers is slightly lower than the peak estimated in the eclogite. This is due to a late re-equilibration of the M1a-M2 mineral assemblages to lower P and T (Fig. 5.13).

Furthermore, Janàk *et al.* (2013) shows that the eclogitic dyke underwent a phase of isothermal decompression from P=3.0 GPa (M2) to P~1.0 GPa (M3), similar to the decompression in eclogites (Van Roermund, 1985). All other thermometers applied on M2 and M3 phases give concordant results between 640 and 720°C. These new results indicate a phase of isobaric cooling from T = 800°C (M3a; Janàk *et al.*, 2013) to T = 680±40°C (M3b; pressure is set at 1.5 GPa).

Most of the thermometers used involved Fe-Mg exchange between ol and other phases. However, olivine is the major component of the F8 garnet peridotite (ol > 70% in vol.) and these Fe-Mg exchanges should not affect its composition. Thus, it is assumed here that the Mg# of olivine remains constant with time.

5.4 Bulk rock chemical composition of the FGP

The Bulk rock chemical analyses of sample F2, F6, F7 and F8 are obtained by XRF analysis which was calibrated for typical elements of the ultramafic system (Mg, Fe, Si, Ca, Cr, Ni, etc.).

The element oxide analysis had to be carried out under dry conditions, therefore all samples were heated up in several steps. All elements eliminated during heating were measured and quantified as LOI in Tab. 5.8.

In the results of XRF analyses iron is calculated as Fe³⁺. A ratio of 0.9 between Fe²⁺ and Fe³⁺ has been assumed here based on the average oxidation state of EMP analyses.

Tab. 5.8. Results of XRF analyses performed on samples F2, F6, F7 and F8 expressed as major oxides.

Sample	Lithology	SiO ₂	Al ₂ O ₃	FeO*	Fe ₂ O ₃ *	MnO	CaO	MgO	Na ₂ O	Cr	Ni
F2	Harzburgite	41.07	0.97	8.19	0.91	0.11	0.41	48.10	0.03	2869	2904
F6	Eclogite	46.36	16.21	8.21	0.91	0.17	13.82	14.14	1.37	645	358
F7	Dunite	41.64	0.51	8.55	0.95	0.12	0.15	48.20	-	3509	2889
F8	Lherzolite	42.92	2.94	9.58	1.06	0.14	2.33	42.40	0.18	2693	2380

*XRF calculates all iron as Fe³⁺. A ratio of 0.9 between Fe²⁺ and Fe³⁺ has been assumed here.

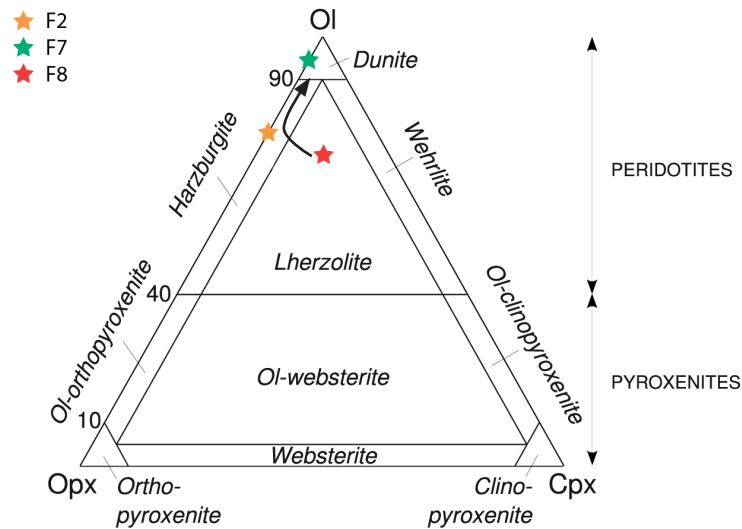


Fig. 5.14 - Classification for ultramafic rocks on the basis of mineral mode (Ol-Opx-Cpx).

All peridotite samples are characterised by a high MgO > 42% and low SiO₂ < 43%. Note the really low Al₂O₃ and CaO < 1% of samples F2 and F7, harzburgite and dunite respectively. Mineral abundances of the main phases in sample F2, F6, F7 and F8 were estimated using PerpleX. Mineral abundances, expressed in vol.%, are shown in Tab. 5.9 and plotted in Fig. 5.14.

Table 5.9. Modal percentage of the main minerals for the analysed samples. Amounts refers to optical estimation of the % vol. of the main rock-forming minerals. Cpx in eclogite (F6) is omphacite.

Sample	Lithology	olivine	opx	cpx	grt	spl
F2	Harzburgite	~75%	~20%	-	~5%	-
F6	Eclogite	-	-	55%	~45%	-
F7	Dunite	~92%	~5%	-	-	~3%
F8	Lherzolite	~70%	~10%	~10%	~10%	-

5.5 Pseudosection

The bulk rock composition of the sample F8 has been used to calculate a thermodynamic phase diagram using the software PERPLEX (Connolly, 2009). In order to simplify the system, H₂O has been considered as pure fluid phase at lithostatic pressure. This assumption does not influence the position this of phase boundary line for hydrated phases at T>600°C.

The pseudosection for the garnet peridotite sample (F8) is shown in Fig. 5.14. The blue lines are two phase boundaries in the eclogite (Sample F6).

Note in the diagram (Fig. 5.15) the spinel to garnet phase transition (~1.5 GPa). This phase boundary has been used to infer the upper P limit of the M1b/M1c mineral assemblage. The lower limit is, instead, defined by the garnet in phase boundary in eclogite (F6). In fact, within orthopyroxenites and eclogites garnet is always stable (i.e. the M1b symplectite does not form).

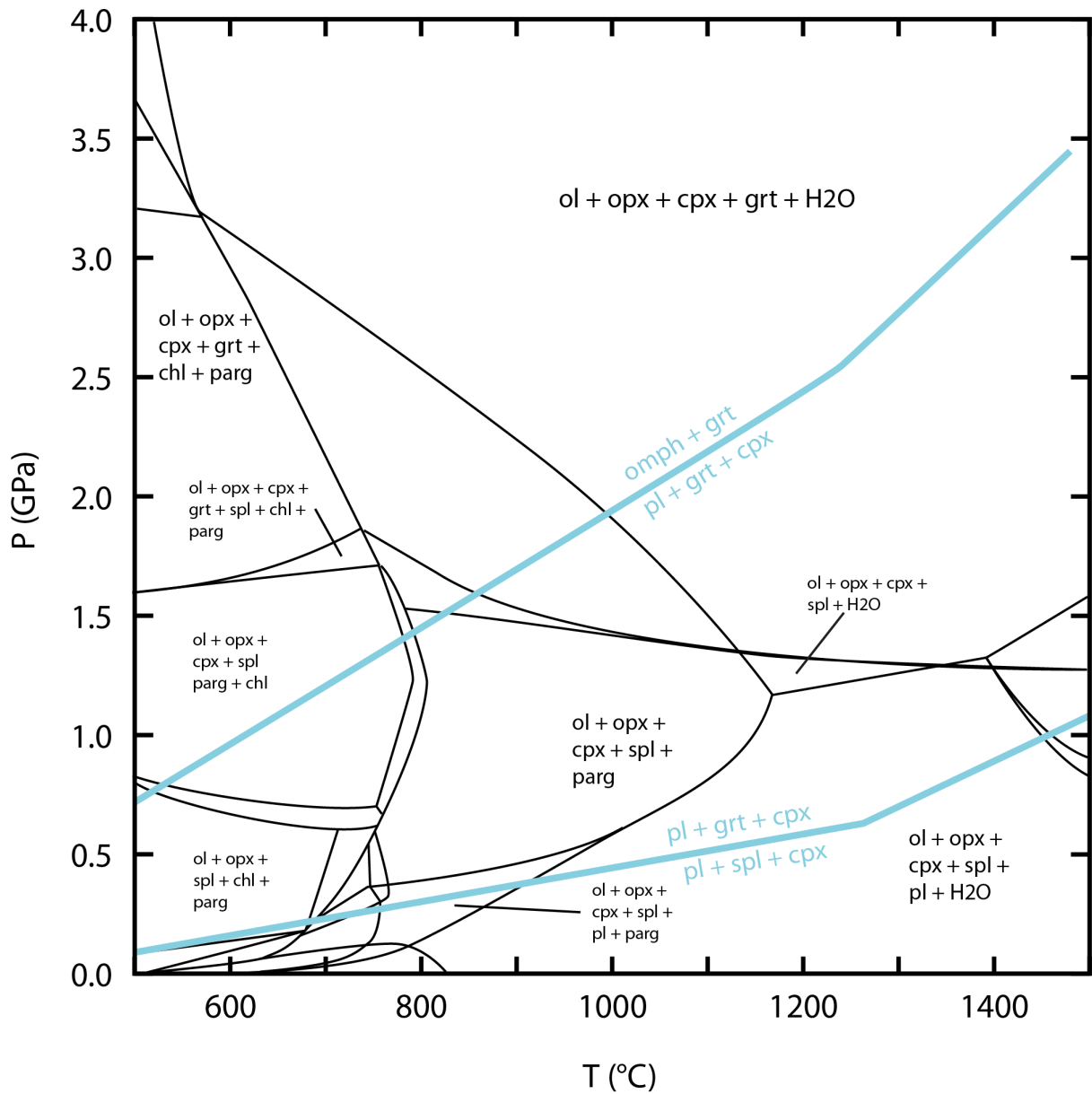


Fig. 5.15 - Calculated pseudosection for a Fringing garnet Iherzolite. Bulk rock composition F8 in tab. 4.7 plus H₂O = 0.8 (wt.%). The blue line are thermodynamic phase boundaries in eclogite (sample F6).

6 - OLIVINE FABRIC ANALYSIS

6.1 Introduction

Most upper mantle peridotites are characterized by a strong crystallographic preferred orientation (CPO) defined by the major olivine crystal axes. This CPO is believed to be the result of solid-state convective motion in the sub-continental lithospheric mantle. These motions induce different creep mechanisms believed to be the cause of the rotation of the crystallographic axes according to the mantle flow directions. Dislocation creep is the main mechanism that controls the rotation of olivine crystallographic directions into strong CPO patterns (Raterron *et al.*, 2007). However, other mechanisms like nucleation, recrystallization and grain boundary migration (GMB) can also significantly modify the CPO, by strengthening, weakening or by modifying the dominant operating slip system imposed by the deformation process (Karato, 1988; Zhang & Karato, 1995; Bystricky *et al.*, 2000). Thus, the characteristics of the final CPO depends on factors such as temperature, deviatoric stress and presence/absence of fluid (Jung & Karato, 2001; Jung *et al.*, 2006; Raterron *et al.*, 2007).

The Friningen garnet peridotite can be used to investigate the role and behaviour of olivine in the upper mantle for several reasons. First of all, the composition of the FGP is mainly dunitic/harzburgitic \pm garnet, with rare lherzolite and orthopyroxenite. The overall amount of olivine is, in most cases, $\geq 75\%$ and thus often approximated to be pure olivine. Furthermore, it is possible to associate a particular olivine fabric to the PT range during which it formed/developed.

The FGP is characterised by the presence of three distinct olivine microstructures, M1 olivine porphyroclasts, M2 and M3 olivine "foam" microstructures. The M1 grains are coarse, largely deformed olivine crystals, surrounded by dynamically recrystallized smaller grains with a particular microstructure: strain free grains surrounded by straight grain boundaries meeting in 120° angle called M2 olivine "foam" microstructure. The latter forms a pervasive olivine fabric present throughout the entire body and consists of 0.2-2 mm sized grains. The M3 foam microstructure consists of much smaller olivine grains (< 0.2 mm) and it has only been observed along localised, non-pervasive M3/D3 shear zones.

In this chapter, a thorough investigation of the aforementioned olivine microstructures will be presented in order to investigate the deformation mechanisms involved in their formation. This investigation involves the study of the crystallographic preferred orientation (CPO's), the associated deformation-induced dislocation substructure(s) and slip system(s) and a detailed analysis of the associated olivine microstructure(s).

6.2 Olivine

Olivine $[(Mg,Fe)_2(SiO_4)]$ is an orthosilicate with orthorhombic symmetry ($\alpha=\beta=\gamma=90^\circ$; $a>b>c$). In terms of chemistry it is a solid solution between Fayalite (Fe^{2+}) and Forsterite (Mg^{2+}). The crystallographic and optical characteristics of the end-member Forsterite (which is around 80-95% in olivine from peridotites) is shown in Fig. 6.1. In olivine, the crystallographic directions (a, b, c) are parallel to the optical axes (α, β, γ) and their relations are the following:

$$\begin{aligned}\alpha &\approx [010] // a = 10.21 \text{ \AA} \\ \beta &\approx [001] // b = 5.99 \text{ \AA} \\ \gamma &\approx [100] // c = 4.76 \text{ \AA}\end{aligned}$$

The energy of a dislocation is proportional to the square of the Burger vector (i.e. displacement vector of dislocations; Passchier & Trouw, 2006). In a deforming crystal, slip will then preferentially occur in the direction of the shortest Burger vector. In olivine, slip is "expected" to occur preferentially along the $[100]$ or $[001]$ directions (the energy required to activate the $[010]$ Burger vector is approximately four times as high as the other displacement directions). The operating slip planes are the planes along which dislocation glide takes place. The operating slip plane $[B](hkl)$ depends on temperature, pressure, stress, strain rate and water content.

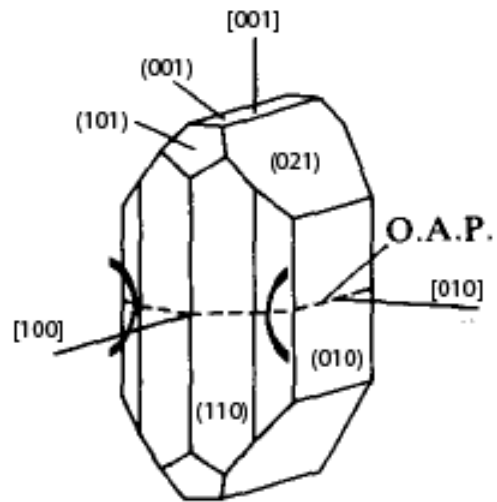


Figure 6.1 - Graphical representation of a forsterite crystal.

6.3 Deformation-induced olivine microstructures

By deforming a crystal its internal energy increases. This is due to the fact that dislocations and/or point defects are randomly introduced during deformation. This is a highly unstable state and causes activation of a series of mechanisms in order to decrease the total energy state of the crystal. Common mechanism involves (1) annihilation and migration of dislocations, (2) production of neoblasts, (3) migration of grain boundaries or (4) a combination of the aforementioned processes. In particular, mechanism (2), is called dynamic (i.e. stress induced) recrystallization (DXR). DXR is usually a result of a combination of two recrystallization mechanisms acting together: subgrain rotation (SGR) and grain boundary migration (GBM). Both these mechanisms are able to produce new grains.

SGR recrystallization occurs when dislocations, at high enough T can climb freely, producing subgrain boundaries. As such, the misorientation angle between adjacent subgrains will progressively increase. When this misorientation angle is $\geq 10^\circ$ it is said that the subgrain became a new grain (Passchier & Trouw, 2006).

In the case that two adjacent grains have a different dislocation density, this difference in stored strain energy will cause the grain boundary to move into the high energy crystal. This mechanism is especially active at high- T . At lower T , the grain boundary mobility is reduced. However, grain boundaries can locally bulge and form a new grain. This process is called grain boundary bulging (GBB).

Grain boundaries can be considered as planar defects with an internal strain energy component. In general, deformation and associated recovery processes (DXR) as described above produce grains with irregular grain boundaries (i.e. high energy surfaces). As such, straight grain boundaries are therefore preferred as the associated internal energy is much lower. This process of grain boundary "migration" may ultimately result in grain growth when, after straightening, the total grain boundary surface will further reduce. The combined processes of straightening and growth of grain boundaries is called grain boundaries area reduction (GBAR). This process, called annealing, is usually active during deformation. However, it may become dominant after deformation, especially at high-T (Bons & Urai, 1992). This later process may (or may not) cause considerable grain growth. However, Calon (1979) observed that, in the case of annealed olivine, grain growth was negligible. Furthermore, annealing processes may cause a reduction of the overall strength of olivine CPO's.

M1 olivine porphyroclasts

In the field, olivine porphyroclasts appear as coarse 2-5 mm-sized crystals and are usually associated with M1 garnet, \pm opx and \pm cpx. Good examples can be found in boulders in front of the peridotite body and, in place, in the vicinity of sample F8 location (Tab. 4.1; Fig. 6.2a-b).

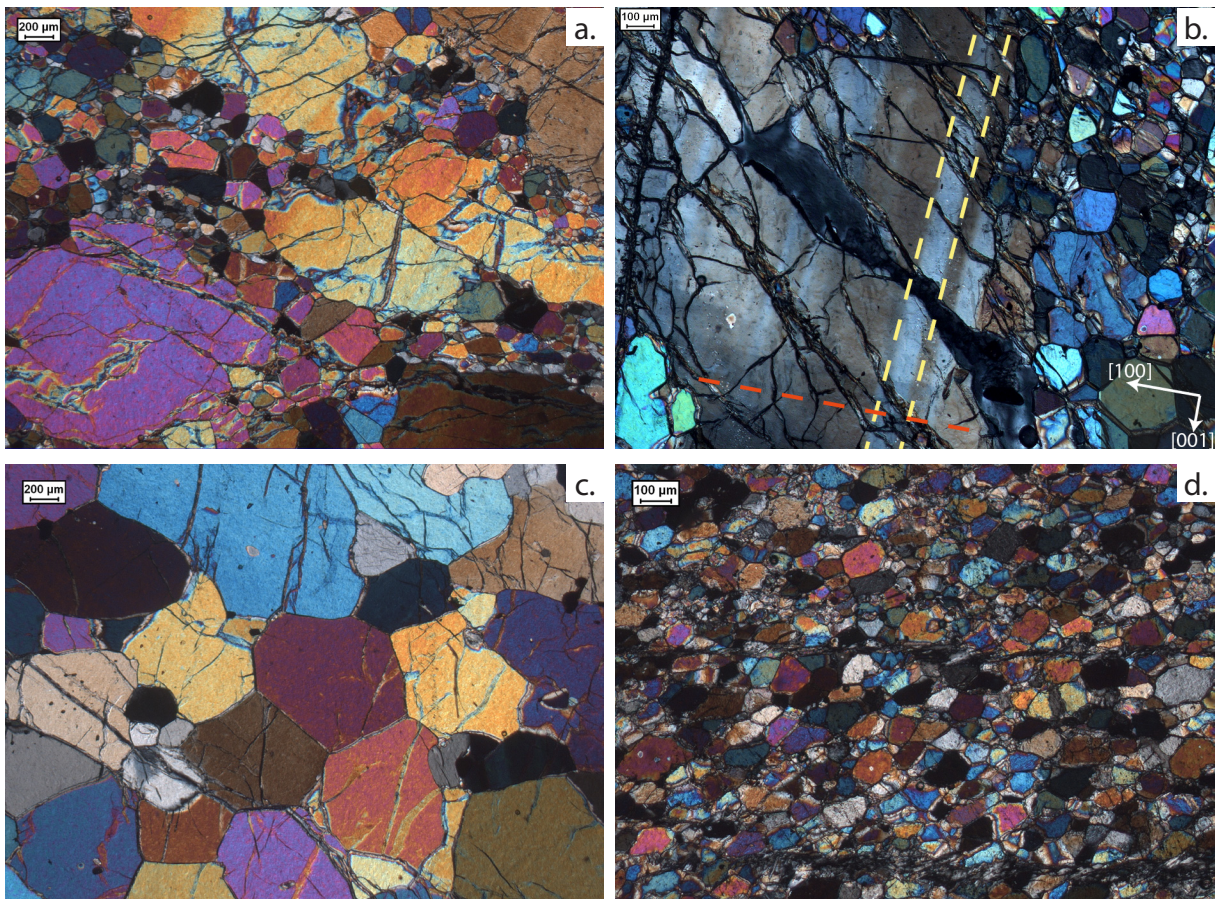


Fig. 6.2. Different olivine microstructures. (a.) cm-sized M1 olivine clasts. Note the olivine M2 "foam microstructure" at the edge of these crystals (F8). (b.) M1 olivine clasts show often one set of kink bands perpendicular to [100] but, in this picture, a second set is found perpendicular to [001]. The second set is, however, less defined, and it has been observed as undulose extinction in several other M1 clasts. (c.) M2 olivine "foam microstructure" (F7). Olivine grains display an annealed texture characterized by straight grain boundaries meeting in 120° triple point junctions. Grain size 1600-400 µm. (d.) M3 olivine "foam microstructure" within the M3 shear zone (F10). Strain-free olivine grains with straight grain boundaries defining triple point junctions. Grain sizes vary from 100 to 20 µm.

In the optical microscope, M1 olivine porphyroclasts consist of large (mm-sized) grains, highly deformed and corroded (Fig. 6.2a-b). Several grains contain tiny round-shaped inclusions formed by one or more phases (Mg-Fe-Ca carbonates, rutile and Fe-Ni sulfides). These inclusions define straight lines that sharply end at the edge of the crystal. The defect structure of most M1 olivine grains is characterised by one set of kink bands parallel to (100). In some olivine crystals, two sets of kink bands have been found. The second set parallel to (001). Cross-cutting relationships clearly indicate that the first set “precedes” the second (Fig. 6.2b). Grain boundaries of M1 olivine grains are highly irregular and always in contact with a fine-grained matrix consisting of optically strain free olivines (called M2 olivine foam microstructure).

M2 olivine foam microstructure 1

In the field, the M2 olivine foam microstructure 1 defines a penetrative fabric (called S2) throughout the peridotite body. Locally S2 makes an angle of about 30° with the compositional layering (S1). Normally, however, the two are parallel. Due to the granoblastic character of this fabric, the S2 foliation is generally hard to define and, in more dunitic layers only defined by oriented opx+spl clusters.

In the optical microscope, olivine M2 grains display an annealed texture, characterised by optical strain free grains with straight grain boundaries meeting in 120° triple point junctions, in equilibrium with opx+am±cpx±spl (Fig. 6.1c). The grain size is highly variable, ranging between 800-200 µm. Fluid inclusions are rare and, if present, never organized in linear patterns. This olivine M2 texture is clearly in equilibrium with M2 opx and cpx crystals, showing the same microstructure.

M3 olivine foam microstructure 2

In the field, the M3 olivine foam microstructure 2 consists of very fine grained olivine grains present within 2-10 cm thick anastomosing bands defining shear zones.

In the optical microscope (Fig. 6.1d), olivine M3 grains display an annealed texture with slightly elongated grains forming an angle of about 30° with the main foliation (S2). As the M2 olivine, M3 olivine “foam” microstructure is characterised by optically strain-free grains with straight grain boundaries meeting in 120° triple point junctions. The grain size is, however, small, ranging between 200-20 µm. Furthermore, the grain size is not homogeneous throughout the thin section but, instead, incremental microstructures define a transitional stage from larger to smaller grains. This olivine M3 texture is stable with opx and am.

6.4 Dislocation substructures

6.4.1 Introduction

Perfect (ideal) crystals consist of three dimensional arrays of atoms with no disturbance in their atomic arrangement. Real crystals contain imperfections that can be point, line, surface or volume defects disturbing the regular arrangement of atoms. In particular, line defects, or dislocations, play an important role in the rheology of the crystal, especially at high pressure and temperature. Dislocations can be divided in edge and screw dislocations. The former represent the end of the extra plane in the lattice while the latter are the twisted part of it (Passchier & Trouw, 2006). When edge and screw dislocation are interconnected, a dislocation loop may form. Every dislocation is associated with a Burger vector (B) representing the minimum displacement needed in order to re-establish the perfect lattice order. The line direction (L) of an edge dislocation is orthogonal to B ; in the case of screw dislocation it is parallel. The mobility of dislocations along the slip systems can be influenced by several factors like temperature, pressure, strain rate, mineral chemistry, and fluid content. The predominance of one (or more) of these factors over the others might favour the production (resulting in deformation) or the recovery (resulting in annealing) of particular distinct slip systems. Therefore, a study of the dominant dislocation substructure might indicate important constraints on the operating slip system, as well as P , T and strain rate conditions, during deformation.

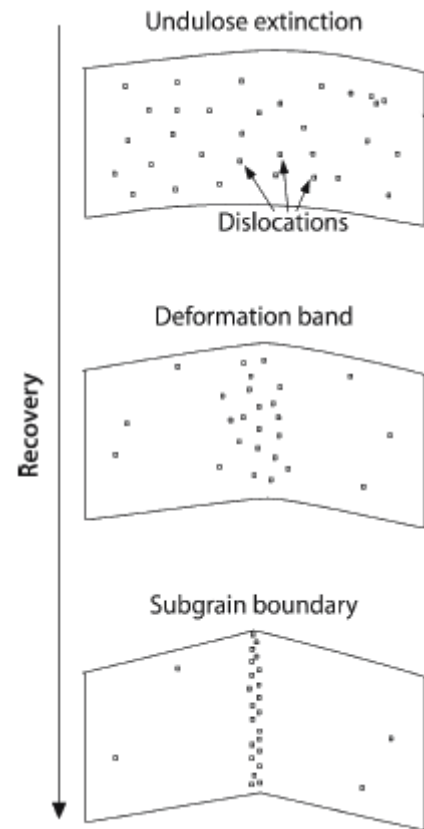


Fig. 6.3 - Schematic illustration of three steps of the recovery processes, syn- and post-deformation. During and shortly after deformation, dislocations are randomly oriented in the crystal. This causes undulose extinction (image on the top). As recovery propagates, dislocation organise into sub-structures in order to decrease the internal crystal energy. Recovery results in the annihilation of dislocations and/or formation of well organised structures called deformation bands (misorientation $<5^\circ$) or tilt walls and/or sub-grain boundaries. (Passchier & Trouw, 2006)

Plastic deformation causes production of new dislocations which results in a large increase of the internal strain energy of the crystal. In order to reduce this energy and/or to re-establish a lower and stable energy configuration (more stable crystal), the dislocations either annihilate through mutual interactions or rearrange themselves into lower energy configurations. Low energy configurations are called low-angle subgrain boundaries and are defined by well organized dislocation substructures. They separate regions within an almost strain free crystal surrounded by boundaries defined by well organized dislocations. The processes involved in the creation of low-angle subgrain boundaries is shown in Fig. 6.3. Consider a crystal being deformed. Dislocations will randomly be produced, increasing the internal energy of the crystal (called stored strain energy). This energy can be reduced by rearranging dislocations into vertical walls, forming, in the case of olivine, symmetrical tilt wall boundaries (misorientation $<5^\circ$) at first and, as recovery continues, of subgrain boundaries (misorientation $\leq 10^\circ$). If the misorientation $> 10^\circ$ a new grain is produced.

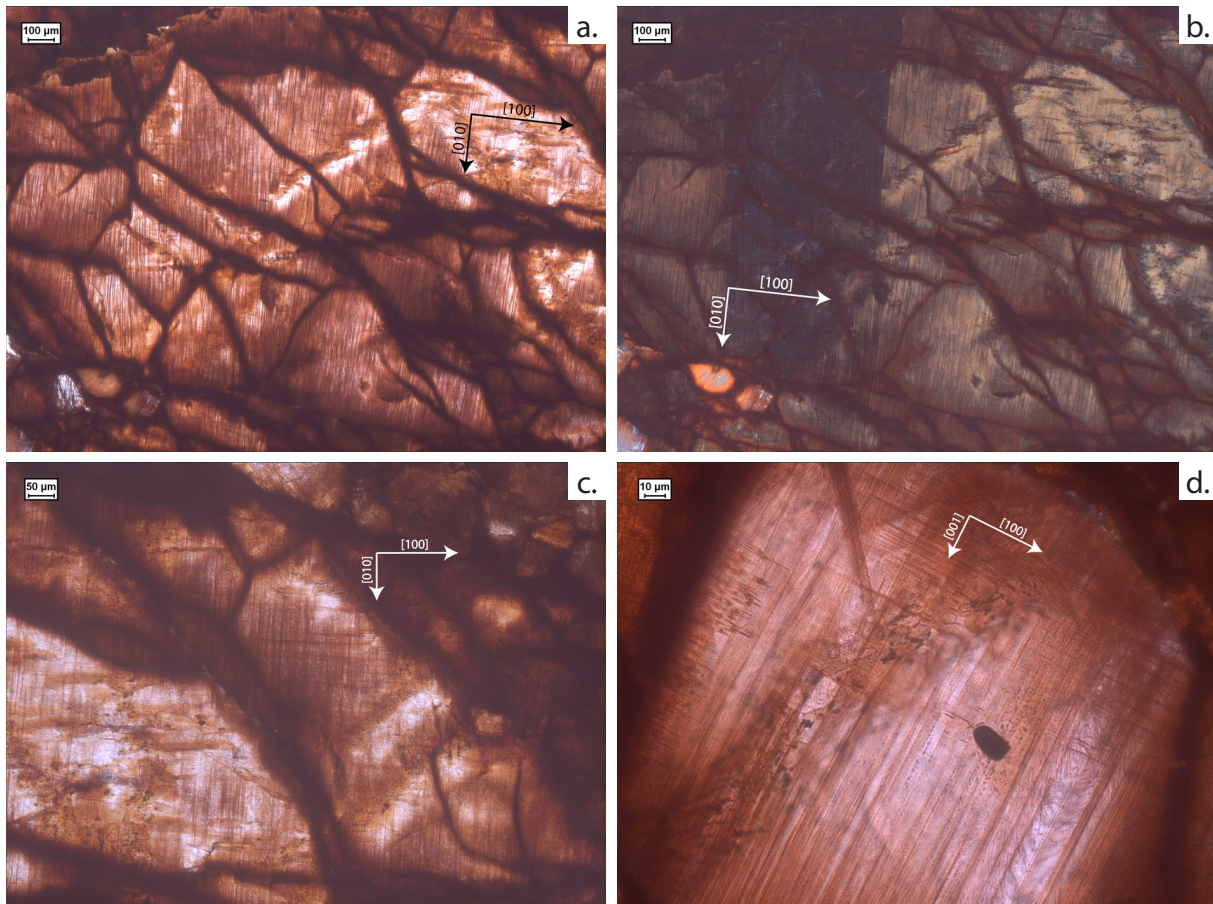


Fig. 6.4. Dislocation walls in different generations of olivine grains compared. (a.) Photomicrograph in PPL of dislocations in M1 olivine clast (F8). Dislocations are disposed along planes roughly perpendicular to the [100]. Note the misorientation in correspondence of the kink band (enlightened in b.). (b.) Photomicrograph of (a.) in XPL. The dislocation planes are parallel to the kink bands. (c.) Photomicrograph in XPL of dislocations in M1 olivine clast (F8). Note the two generations of dislocation walls. Dislocations perpendicular to [010] are less developed, though crosscut dislocation perpendicular to [100]. (d.) Photomicrograph in PPL of dislocations in M2 olivine "foam microstructure" (F8). Note three different sets of mutually perpendicular dislocation walls (two easily visible, a third one drawing little red dots on the surface of the crystal, representing tips of single dislocations). Note on the right side of the picture, sub-grain walls and rare line oblique with respect to the crystallographic axes.

Dislocations cannot be directly observed with the optical microscope because their size is too small (nm scale) for optic-based instruments. Usually TEM is required. However, several chemical techniques have been developed to decorate the dislocation core zone which makes them "visible" in the OM. Here, the olivine decoration technique, described by Kohlstedt *et al.* (1976), is used to visualize dislocations. Decoration is produced by heating up the sample to about 1000°C for one hour under atmospheric conditions (including oxygen). By this process Fe becomes oxidized. This process causes the precipitation of iron oxides (mainly hematite) in the dislocation core zones, making them visible in the optical microscope.

6.4.2 Optical observations

Most of the dislocation substructures consist of three sets of lines organised, parallel to the three crystallographic axes of the olivine crystal. In Fig. 6.4a-b, a M1 olivine clast is shown with a very well developed microstructure defined by dislocations perpendicular to [100]. Note, that the dislocation lines follow the misorientation of the crystal produced by the kink band. Sets of dislocations perpendicular to [010] and [001] are sometimes present but not particularly developed. In Fig. 6.4c a second set of dislocation is shown in a magnified

portion of the previous M1 grain. This second, less developed, set clearly crosscuts at high angle ($\sim 90^\circ$) the previous one.

Dislocation substructures present within olivine grains forming the olivine foam microstructure are highly variable, depending on the grade of annealing of the crystal. Olivine grains from section F7 are almost completely annealed and dislocations are extremely rare. Instead, olivines from section F8 (Fig. 6.4d) show a wide range of different dislocations substructures. Though usually different sets of dislocations are displayed better in other grains, the grain shown in Fig. 6.4d is highly representative of all the sets found. The most common set is perpendicular to $[100]$. However, also sets parallel to $[001]$ and $[010]$ can be observed. The latter can be visualised by the small dots in the picture, representing the tip of a dislocation line perpendicular to the field of view. On the right side of the picture, sub-grain walls and rare dislocation-line oblique with respect to the crystallographic axes can be seen.

6.4.3 Discussion

The dislocation substructures described in chapter 6.4.2 are the result of recovery processes active during and/or after deformation. M1 olivine clasts show two sets of regularly spaced dislocation walls. The spacing between dislocation walls equals 5-10 μm . Reduced spacing between dislocation walls might be the result of annealing processes that occurred while temperature were still high enough to allow dislocations to slip and climb. In fact, the mobility of dislocations highly depend on T. At HT, glide and climb of dislocations occurs simultaneously. Conversely, at relatively low temperatures, dislocation mobility is strongly limited, allowing dislocations only to glide in their slip plane.

The orientation of the dislocation walls as well as kink walls in M1 olivine clasts suggest a principal direction of motion parallel to the $[100]$. A secondary and late direction of motion is parallel to the $[010]$ direction. The three sets of dislocation found within the M2 olivine "foam microstructure" grains, were probably active at the same time, moving orthogonally in the direction of the crystallographic axes (Fig. 6.4d). This suggests that olivines had a different rheology then when M1 olivine clasts were deformed. During this second deformation phase, temperature was probably lower. This is suggested by the presence of randomly oriented (not annealed) dislocations (Fig. 6.4d).

6.5 Crystal preferred orientation (CPO)

In this section, the olivine fabric classification described by Jung & Karato (2001) is used. They identified the following four olivine slip types: A-type = $[100](010)$, B-type = $[001](010)$, C-type = $[001](100)$ and E-type = $[100](001)$.

A statistically significant number of grains has to be measured in order to produce a CPO diagram. The CPO's of four different samples were measured (F3-F7-F8-F10) and are shown in Fig. 6.5-6.8. In every CPO diagram, the real lineation and foliation is rotated in order to better visualize the data. The foliation is rotated to $000/90$ (E-W line in the CPO diagrams) and the lineation is rotated to $090/00$.

The CPO's of the M1 olivine clasts are shown in Fig. 6.5. This plot summarises measurements taken on 120 different crystals from sample F8. The real orientation of the lineation is $108/07$. This plot shows a very strong and clear CPO. The very strong cluster of $[010]$ directions indicates the main active slip plane was (010). The dominant slip direction is given by the cluster parallel to the E-W lineation (i.e. $[100]$ and $[001]$ directions both show a very strong cluster). This suggest two different slip systems were active during deformation: $[001](010)$ and $[100](010)$.

The CPO of an M2 olivine "foam microstructure" is shown in Fig. 6.6. This plot summarises measurements taken on 200 different olivine crystals from sample F7. The real orientation of the lineation is $210/20$. Fig. 6.6 shows a very strong and clear cluster of $[010]$ suggesting the main active slip plane was (010). Both $[100]$ and $[001]$ form clusters at small angle to L and perpendicular to S. As such, two different slip systems were active during deformation: $[001](010)$ and $[100](010)$. However, in this case the B-type CPO is clearly subordinate with respect to the A-type. Furthermore, slip directions show a really strong asymmetry with respect to the E-W foliation. A- and B-type indicate dextral (top-to-the-SW) and sinistral shear sense (top-to-the-NE) respectively.

The CPO of an M2 olivine "foam microstructure" is shown in Fig. 6.7. This plot summarises measurements taken on 170 different olivine crystals from sample F3. The real orientation of the lineation is $148/60$. This plot also shows a cluster of $[010]$ perpendicular to S suggesting the main active slip plane was (010). The $[100]$ plot defines a girdle perpendicular to S with a large cluster parallel to L. This suggests multiple slip directions were active.

The CPO of an M3 olivine "foam microstructure" is shown in Fig. 6.8. This plot was produced using the EBSD technique. The real orientation of the lineation is $045/25$. The plot shows a very weak CPO. However, small clusters indicate that $[100](001)$ slip was active. This shows a very strong asymmetry indicating a dominant dextral (top-to-the-NE) shear sense.

F8 - M1 ol clasts

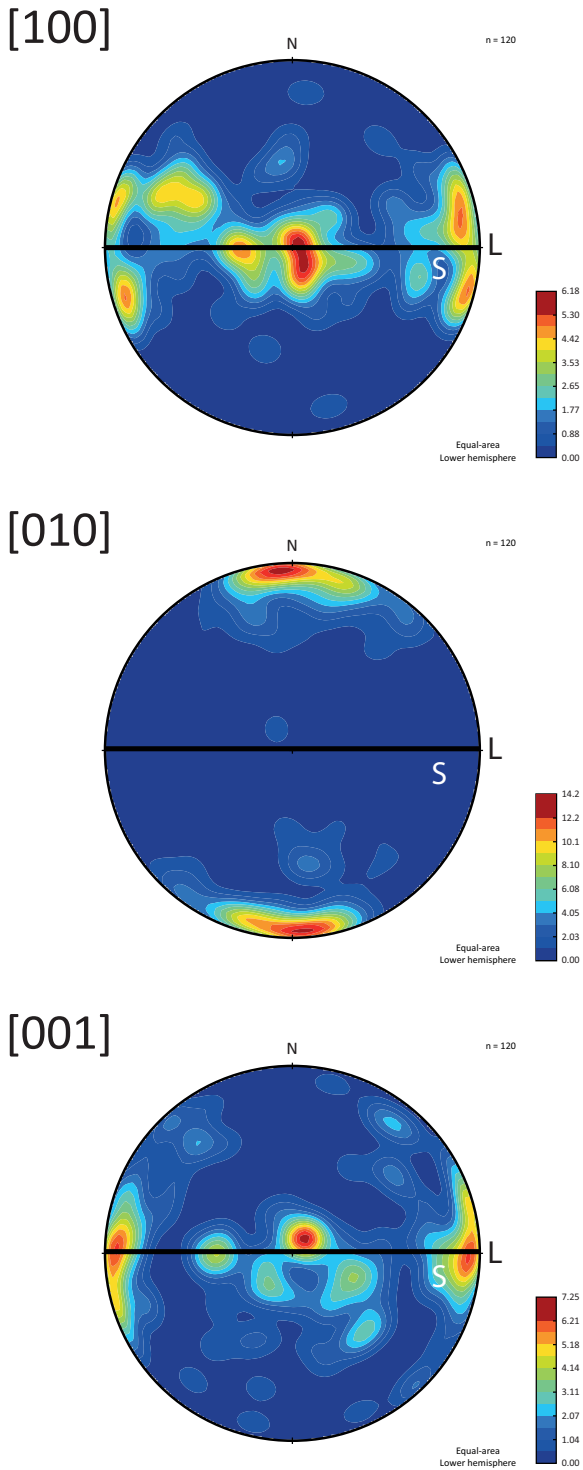


Fig. 6.5. Crystallographic Preferred Orientations (CPO) of M1 olivine grains (sample F8). N is the number of measured grains (N = 120). Mineral lineation oriented E-W. The CPO displays [010] axes max concentration perpendicular to the foliation and [100] and [001] display two max, parallel and normal to the lineation. This indicates both (010)[100] a-slip and (010)[001] b-slip were active during deformation.

F7 - ol "foam microstructure"

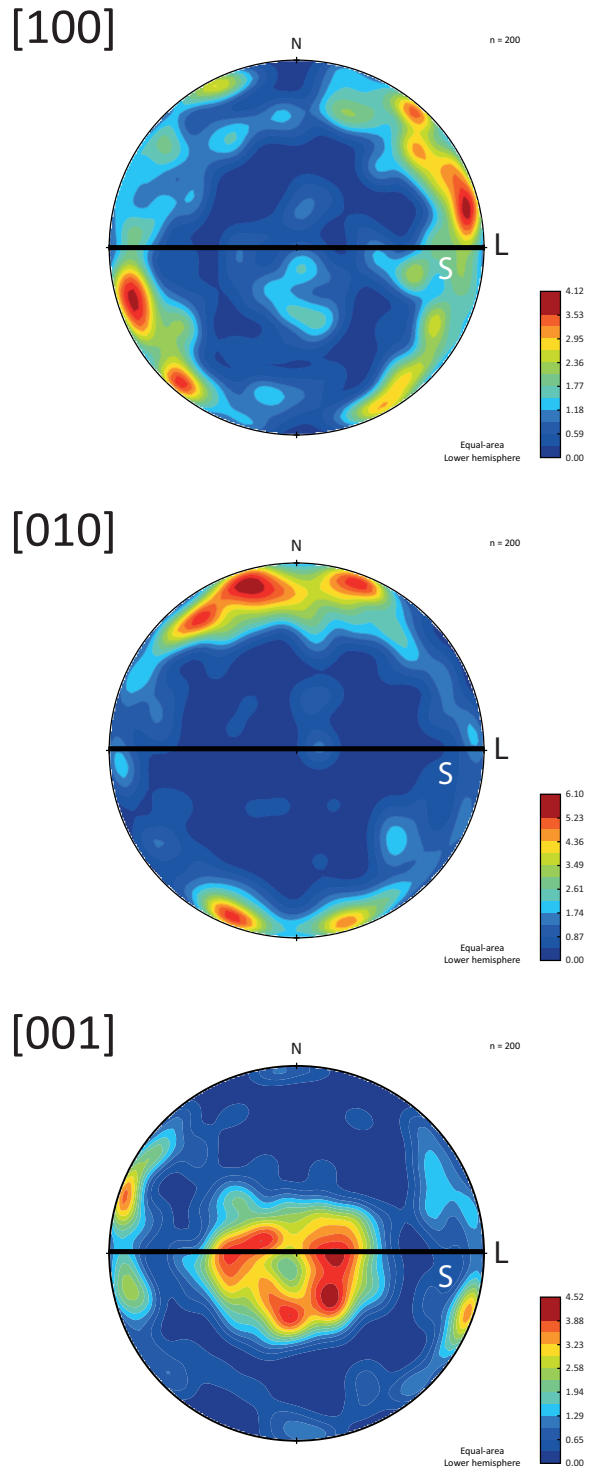


Fig. 6.6. Crystallographic Preferred Orientations (CPO) of M2 olivine grains (sample F7). N is the number of measured grains (N = 200). Mineral lineation oriented E-W. The CPO displays [010] axes max concentration perpendicular to the foliation and [100] parallel to the lineation. This indicates (010)[100] a-slip was active during deformation.

F3 - ol "foam microstructure"

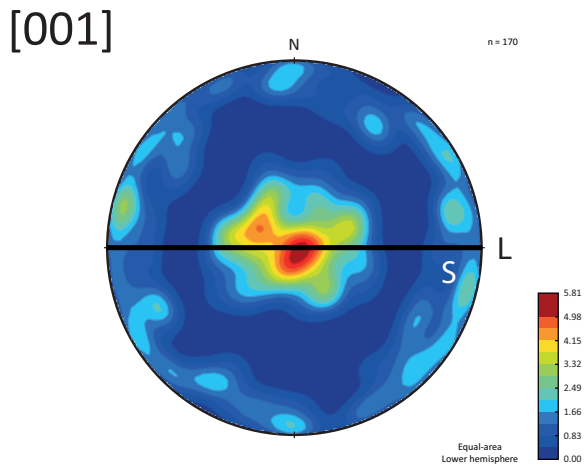
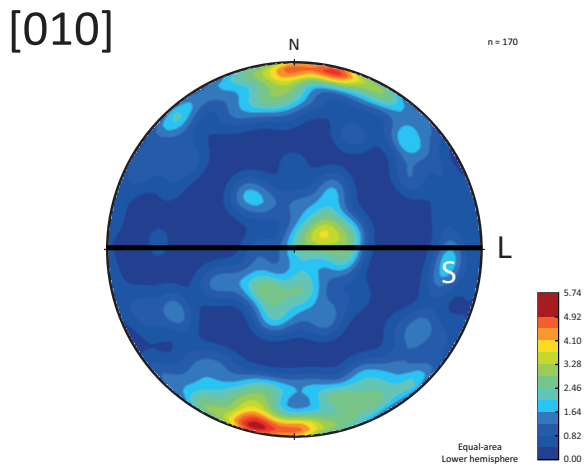
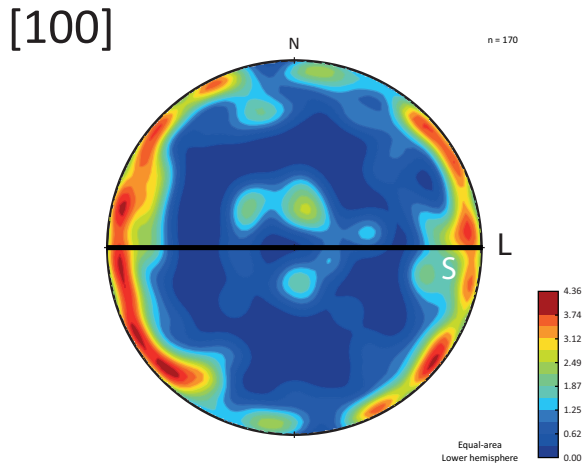


Fig. 6.7. Crystallographic Preferred Orientations (CPO) of M2 olivine grains (sample F3). N is the number of measured grains (N = 170). Mineral lineation oriented E-W. The CPO displays [010] axes max concentration perpendicular to the foliation and [100] defines a girdle perpendicular to S with a large cluster parallel to L. This suggests multiple slip directions were active.

F10 - ol "foam microstructure"

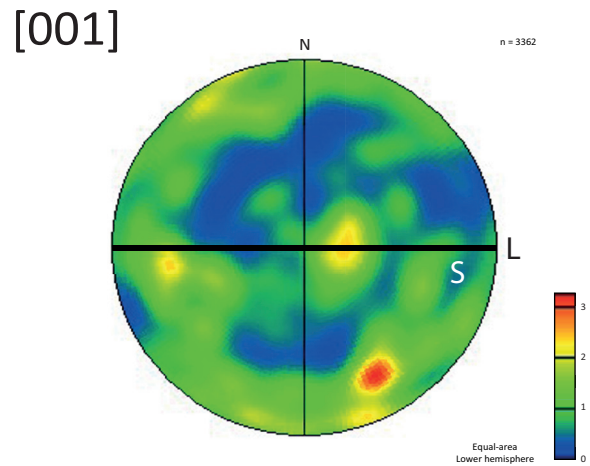
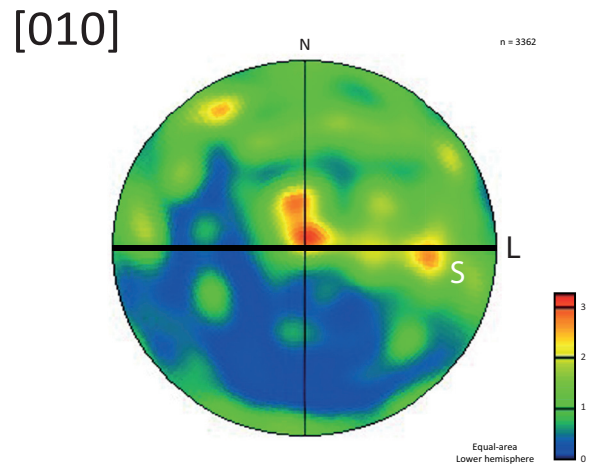
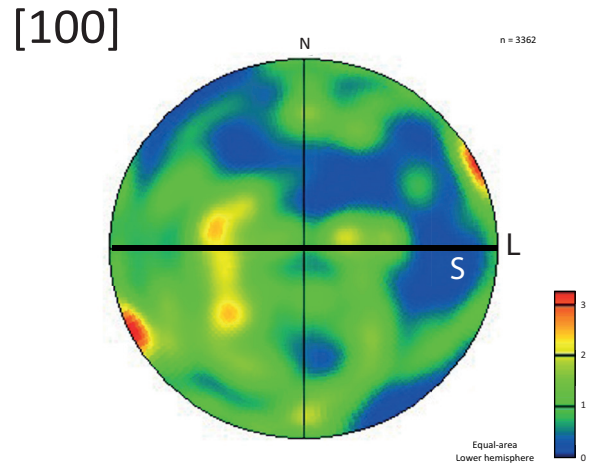


Fig. 6.8. Crystallographic Preferred Orientations (CPO) of M3 olivine grains (sample F10). Mineral lineation oriented E-W. Overall, the CPO displays a very weak preferred orientation. It displays [001] axes max concentration perpendicular to the foliation and [100] parallel to the lineation. This indicates (001)[100] e-slip was active during deformation.

6.5.1 Discussion

The M1 olivine fabric (Fig. 6.5) presents an unexpected result, showing both A- and B-types. These two CPO types were initially considered to be contrasting sub-types, i.e. A-type indicates low stress and dry condition, the B-type is usually associated with very high stress (>300 MPa) and relatively high water contents (Fig. 6.9; Jung *et al.*, 2006). However, Katayama & Karato (2006) investigated the role of temperature on the transition between B- and C-type. Their study showed that, for “low” temperatures ($T < 1000^{\circ}\text{C}$) the B-type can also occur at very low (1-5 MPa) stress conditions (typical mantle conditions).

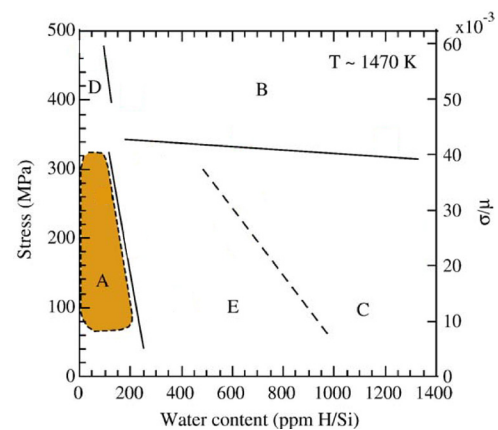


Fig. 6.9. A fabric diagram of olivine at $T \sim 1200^{\circ}\text{C}$ showing the dominant fabric as a function of stress and water content (COH). (Modified after Jung *et al.*, 2006)

M1 olivines (Fig. 6.5) record the progressive transition from a relatively hot ($T > 1200^{\circ}\text{C}$) and dry environment to a cold ($T < 1000^{\circ}\text{C}$) and wet environment. The relatively constant and coarse grain size indicates that the stress levels remained very low and typical of mantle conditions (1-3 MPa). Furthermore, the lack of a clear shear sense is a clear indicator for deformation under pure shear conditions, usually associated with an uniform mantellic fabric (i.e. tectonite) within peridotites (Drury *et al.*, 1991).

The fabric diagram of the M2 olivines (Fig. 6.6-6.7) show an asymmetric A-type CPO's (with minor B-type). A-type fabric is usually associated with dry and hot deformation environments. On the other hand, c-slip is expected to occur at lower temperatures (Jung & Karato, 2001; Raterron *et al.*, 2007). However, both structural and mineralogical evidences suggest this fabric was formed in a cold ($T \sim 800^{\circ}\text{C}$) environment at UHP ($P > 3.0 \text{ GPa}$). The great majority of deformation diagrams refer to olivine rheology for high T ($T > 1200^{\circ}\text{C}$) and low P . However, Raterron *et al.* (2007) showed that, for nominally anhydrous olivines, the transition between A- and C-slip (i.e. A- and C- type) varies with pressure. Raterron *et al.* (2007) showed that, under the PT condition that the M2 fabric was formed (3.0 GPa - 800°C), A-type fabric can be formed.

Sample F3 (Fig. 6.7) was collected few meters above a D3 shear zone. M2 olivines show here the development of an asymmetric A-type CPO's, with evidence of secondary E-type. E-type fabric is interpreted to be related to deformation of olivine under “wet” conditions (Jung *et al.*, 2006). Experimental data suggests the transition between A- and E-type is driven only by the change from a dry to a wet environment (Katayama *et al.*, 2004). Furthermore, the same authors suggest the E-type to be a combination of A- and C-slip. Sample F3 records the transition from A- to E-type, consistent with an increase in water fugacity in localized areas around the D3 shear zones.

Sample F10 (Fig. 6.8) was collected in a 10 cm-thick, anastomosing, D3 shear zone formed at $T = 600\text{-}700^{\circ}\text{C}$ and $P \sim 1 \text{ GPa}$. The very weak CPO's of this sample indicates that the main deformation mechanism was probably grain size sensitive creep. However, grain size insensitive creep was also operating, producing the weak E-slip.

The M2 olivine fabric (fig. 6.6), as well as the M3 olivine fabric (fig. 6.8) display an asymmetric CPO's with respect to the foliation. However, while the M2 olivine fabric indicates a top-to-the-SW shear sense, the M3 olivine fabric display a top-to-the-NE shear sense. This inversion in sense of shear might reflect the shift from subduction (M2) to eduction/nappe stacking (M3).

In conclusion, the FGP was originally a mantellic tectonite forming under low stress (1-3 MPa) and at high temperature ($T \geq 1200^\circ\text{C}$; A-slip). While still in the mantle, temperature decreased below 1000°C causing the transition between A- and B-slip. The D2 deformation was initially a penetrative fabric. However, this deformation event localized (probably in response to a decrease in temperature) into metric-sized shear zones, allowing preferential channels for fluid flow. As temperature decreased, deformation localized further into cm-sized, anastomosing (D3) shear zones. The mechanism involved in deformation of olivine within the D3 shear zones was a combination of grain size sensitive and insensitive creep, responsible for the production of a really weak CPO, as illustrated in fig. 6.8.

6.6 Paleopiezometry

It is well established that grain size can be used to reconstruct paleostress magnitudes (Passchier & Trouw, 2006). However, only recently it has been demonstrated that water plays a fundamental role in determining grain size during DXR (Shimizu, 1998; Jung & Karato, 2001). In addition, dry rocks deform preferentially through SGR. While, increasing water content fastens recovery processes and GBM, preventing high amounts of strain energy to be accumulated in the crystal, thus preventing SGR to operate

Though it is difficult to quantify the amount of water in olivine, the rock mineralogy can be used to get a first indicator to estimate water fugacity. In the FGP, the M1 assemblage consists of anhydrous minerals interpreted to originate in the SCLM. However, water might be dissolved as a trace element in olivine. For reasons of simplicity, this "water" is not taken into account and the M1 assemblage is considered to be "relatively" dry. The M2 assemblage is interpreted to have formed during subduction. Structural and mineralogical evidences suggest that amphibole (pargasite) was stable during the M2/D2 deformation phase. For this reason, the M2 assemblage is considered to have a moderate water fugacity. The M3 assemblage formed within D3 shear zones. This structural position granted a preferential path for fluid flow. The M3 assemblage is interpreted to have formed under relatively high water fugacity conditions.

Typical piezometers for "dry" (Van Der Wal *et al.*, 1993) and "wet" olivine (Jung & Karato, 2001) have been applied on M1 and M3 olivine. M2 olivine is interpreted to have formed under "moderate" water conditions. Therefore, an

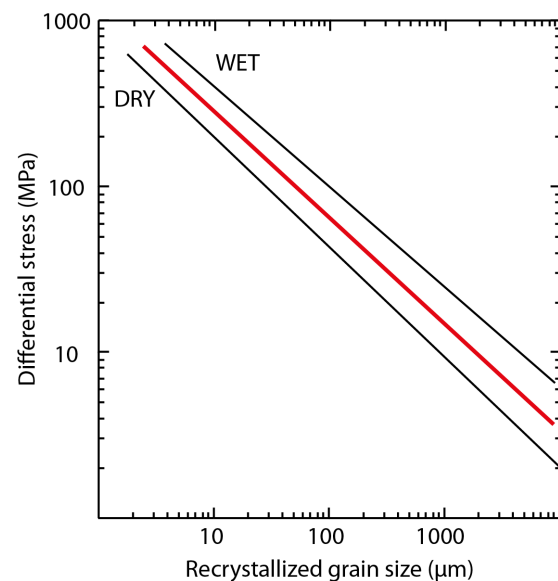


Fig. 6.10. Stress VS recrystallized grain size diagram for olivine. Solid black lines represent piezometers for "dry" (Van Der Wal *et al.*, 1993) and "wet" conditions (Jung & Karato, 2001). The red line represents an intermediate, arbitrary, piezometer for moderate water conditions. (after Jung & Karato, 2001 and Clos, 2013).

intermediate piezometer has been arbitrarily constrained (Fig. 6.10). Calculated differential stress results are shown in tab. 6.1. From the table it can be seen that M1 olivine was formed under very low differential stress conditions (1-3 MPa), typical values for mantle conditions. M2 olivine microstructures formed under intermediate differential stress conditions (10-30 MPa). It has to be pointed out that these stress conditions were not constant throughout the body. In fact, M2 olivine grain sizes slightly change from 200 to 1600 μm . Though this change seems arbitrary, deformation was probably more intense at the edges and weaker within the core of the body. M3 olivine was formed at very high differential stress conditions (70-150 MPa), typical of shear zones.

Table 6.1. Summary of the physical parameters used to calculate differential stress conditions during formation of olivine microstructures M1-M2 and M3.

ol generation	Size (μm)	estimated T	diff. stress (MPa)	Dominant Def. mechanism
M1	>5000 (5 - 10 mm)	1000 - 1100	1 - 3	GSI
M2	1600 - 200	770 - 830	10 - 30	GSI (GSS minor)
M3	100 - 20	660 - 700	70 - 150	GSS (GSI minor)

The main operating deformation mechanisms in the FGP were identified by using the deformation map of olivine, deformed with a strain rate of 10^{13} s^{-1} , produced by Den Hartog (2009). (Fig. 6.11; tab. 6.1). It can be seen from Fig. 6.11 that M1 olivine clasts formed through a grain size insensitive (GSI) creep (i.e. dislocation creep) in dry condition. The estimated temperature is between 1000 and 1100°C. The M2 olivine also formed by GSI, with a small component of grain size sensitive (GSS) creep in zones of particularly intense deformation. The estimated temperature is about 770-830°C. The M3 olivine formed in a high stress environment, mainly through GSS creep (diffusion creep). However, a small component of dislocation creep probably occurred at the same time. This might be responsible for the very weak CPO's found in sample F10 (shear zone). The estimated temperature is about 660-700°C. The temperature estimates for these three different olivine fabrics are concordant with the T estimates of the associated mineral assemblages.

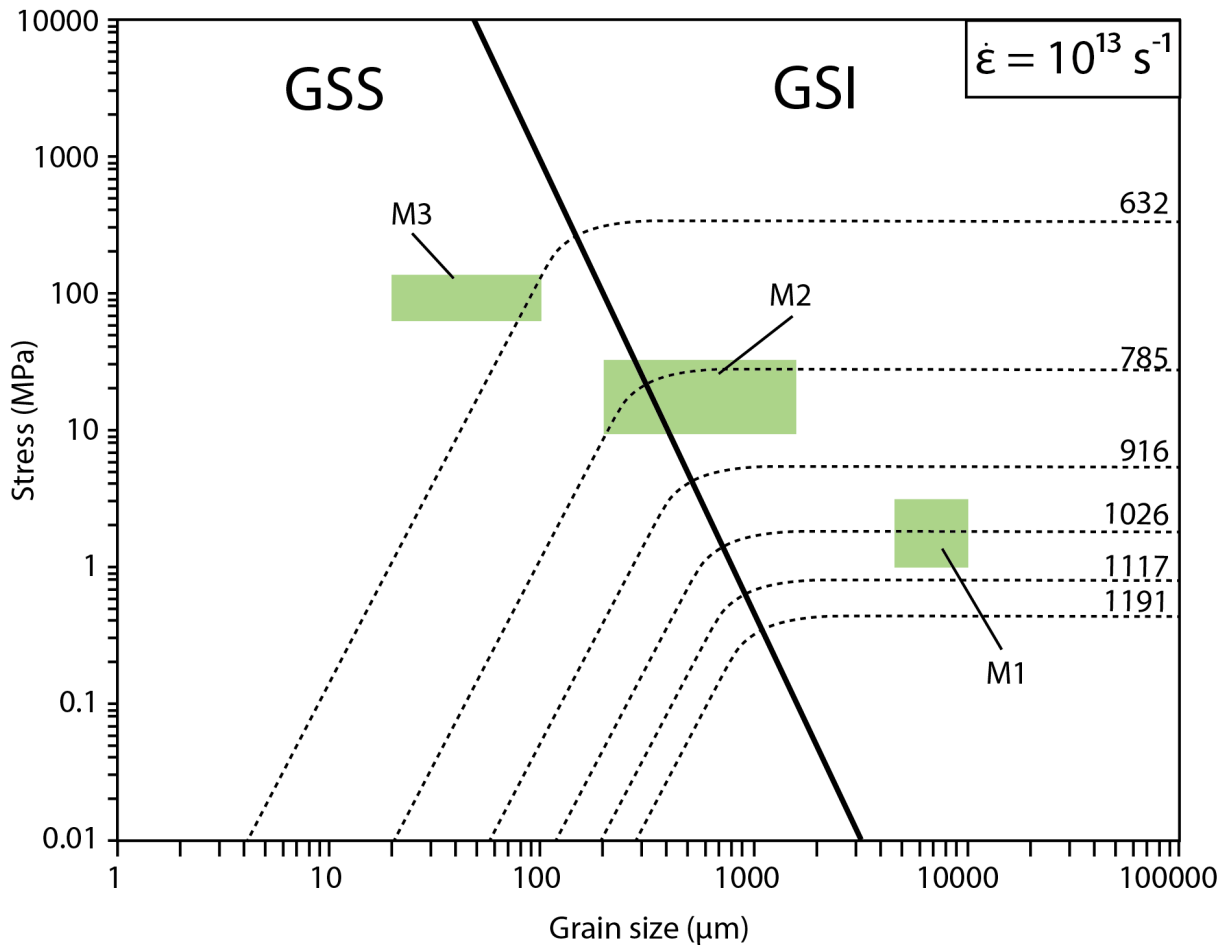


Fig. 6.11. Deformation mechanism map for olivine at constant strain rate (10^{13} s^{-1}), exploring variations of temperature between 630-1200°C. Green areas represent inferred grain size VS stress forming conditions for the different olivine microstructures. M1 olivines were formed through GSI creep (likely dislocation creep) between 1000-1100°C. M2 olivines were formed through a combination of GSI creep (likely dislocation creep) and minor GSS creep (diffusion creep) between 770-830°C. M3 olivines were formed through a combination of GSS creep and minor GSI creep (responsible for a weak CPO) between 660-700°C. (modified after Den Hartog, 2009)

7 - DISCUSSION

7.1 Protolith origin

The bulk rock composition of an ultramafic rock is strongly dependent on the degree of partial melting. This melting depends on (1) the tectonic setting of origin and (2) the thermal conductivity in the mantle. A detailed chemical investigation can help to identify the tectonic setting of the peridotite protolite and/or the age of partial melting. The most useful indicators are forsterite content (Mg#) in olivine and Cr# in spinel. The variability of these two factors is related to the tectonic setting where the peridotite protolith partial melting occurred.

The FGP has been refertilized, leaving almost no trace of the original depleted composition (Brueckner *et al.*, 2004). However, sample F7 belongs to a dunitic layer of the body, where little or no refertilization occurred. Its bulk rock composition is interpreted to be similar to the original refractory and depleted bulk rock composition of the FGP prior the Proterozoic refertilization events by the dykes.

Fig. 7.1 shows olivine Mg# and spinel Cr# field for a wide range of ultramafic rocks in different geological and tectonic settings

(Friend *et al.*, 2002), including the olivine-spinel mantle array (OSMA) of Arai (1994). Two depletion trends can be observed in this figure: (1) cratonic peridotites show $Mg\# > 90$ and (2) abyssal (i.e. oceanic) peridotites have lower $Mg\# = 87-90$. The diagram indicates that spl-Cr# alone cannot be used to reconstruct the geodynamic origin of a (garnet-) peridotite.

However, the combined values of ol-Mg# (92-93) and spl-Cr# (47-51), found in the dunite sample (F7; EMP results in Tab. A1.1 and A1.4) plot within the cratonic peridotites trend. Due to its high olivine Mg#, and spinel Cr#, FGP can thus be compared to the Almklovdalen and Otrøy mantle wedge garnet peridotites of the WGR and to a suite of ultramafic xenoliths derived from highly depleted, Archean lithospheric mantle underneath Laurentia (Bernstein *et al.*, 1998; 2006) and to xenolith samples from Greenland (Tab 7.1).

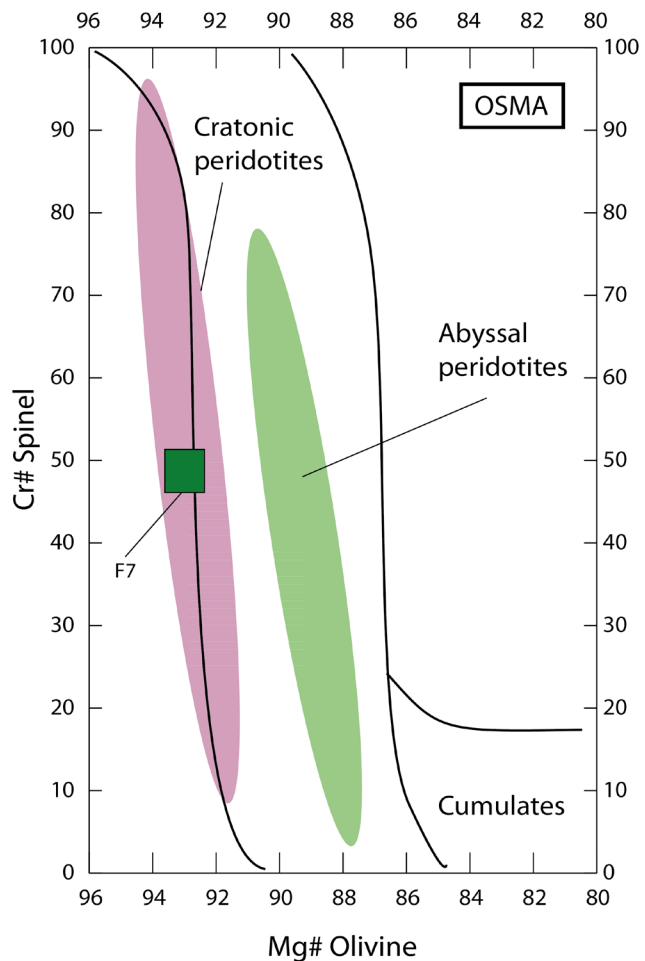


Fig. 7.1. Ol Mg# VS spl Cr# diagram outlining the fields for abyssal (green) and cratonic (purple) peridotites in relationship to the olivine-spinel mantle array (OSMA) and cumulates. The range of the dunite sample (F7) is the green rectangle. (after Friend *et al.*, 2002 and Clos, 2013)

Table 7.1. Ol Mg# and spl Cr# range for several ultramafic rocks from different geodynamic and tectonic settings. Data from FGP and KSP are comparable to the Archean peridotites of Almklovndalen and to the Xenoliths from the mantle underneath Greenland. Data from the Leka ophiolite are in clear contrasts with the aforementioned mantle peridotites. (references in the table)

Provenance	Rock composition	Mg# Olivine	Cr# Spinel	Reference
Friningen (SNC)	Garnet peridotite	90-91	18-40	Present study
	Dunite	93	47-51	
Kittelfjæl (SNC)	Harzburgite	91.2-92.2	76-81	Clos (2013)
	Dunite	92.5-93.6	89-96	
Almklovndalen (WGR)	Garnet peridotite	90.6-91.7	57-67	Beyer et al. (2006)
	Dunite	92-93.6	89-94	
Otrøy (WGR)	Garnet peridotite	90.3-91.5	40-50	Spengler (2006)
Xenoliths (Widermann Fjord Greenland)	Undifferentiated	92.7	5-75	Bernstein et al. (1998)
Xenoliths (Ubekendt Ejland, Greenland)	Dunite	92-93.7	47-96	Bernstein et al. (2006)
Leka (KNC)	Dunite	86-90	70-80	Iyer et al. (2007)

7.2 Estimation of a PTt path

Pre-M1

The early history for the FGP is interpreted to be related to its evolution in the mantle. Brueckner *et al.* (2004) suggested a really old, Archean (~3.0 Ga) melting event, recorded by Re-Os dating of pentlandites, followed by the emplacement of basic dykes in the mid-Proterozoic. A similar melting plus dyke intrusion events has been suggested by Brueckner *et al.* (2002) and Beyer *et al.* (2006) for several peridotite bodies in the WGR. This original melting event was followed by a series of Proterozoic (1.4-1.8 Ga) refertilization events related to the intrusion of basic dykes. The second refertilization event related to dyke intrusion can thus be responsible for the reintroduction of non-refractory elements (like Si, Al and Ca) back into the peridotite. The FGP was probably in the continental lithosphere when similar refertilization events and/or dyke intrusions occurred. It has been suggested (Spengler, 2006) that highly refractory dunites accrete to the base of the lithosphere (100-150 km), partitioned above a relatively fertile upwelling asthenosphere. Partial melting events occurring within this "fertile" asthenosphere might then form dike swarms that, after upward migration into the overlying lithospheric mantle, are responsible for "refertilization" of dunite.

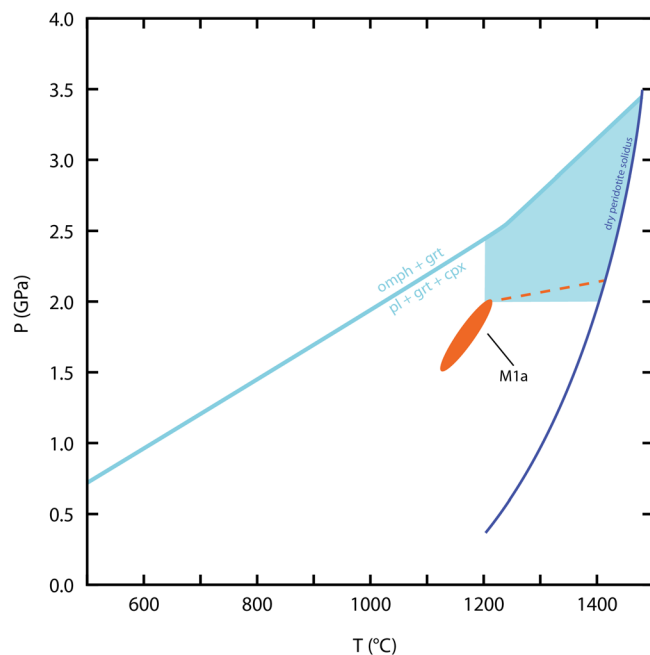


Fig. 7.2. PT stability field of the M1a mineral assemblage (ol+cpx+opx+grt) in garnet peridotite and pl + grt phase boundary line in the dyke (sample F6). The blue shaded area is the maximal PT range where both the M1a mineral assemblage in peridotite and the mineral association grt+pl are stable together (M1a). The orange dot represents the calculated PT conditions for the M1a mineral assemblage. The orange dashed line represents a possible PT path for the pre-M1 mineral assemblage.

The PT conditions during melting and dyke intrusion are highly unknown. However, the high positive Eu anomaly measured within the bulk rock composition of the dyke (Verbaas & Van Roermund, 2012) suggests that protolith of the dyke crystallized within the plagioclase stability field (in basaltic rocks) during the Proterozoic refertilization event.

M1

The older assemblage (M1a) of the FGP records a PT condition of 1.9 ± 0.4 GPa and $\sim 1125 \pm 75^\circ\text{C}$. These conditions might be set as minimal PT conditions for the refertilization event. The maximum pressure is represented by the pl-cpx-grt phase transition line in the dyke (basaltic composition; sample F6), obtained through thermodynamic calculations (fig. 7.2).

Re-equilibration of grt1 into pseudomorphs of spl+opx+cpx/parg at $1050\text{--}1100^\circ\text{C}$ indicate progressive decompression, combined with cooling. The presence of amphibole might suggest the rock was not nominally dry at this point in history. However, it is not possible to clearly infer a source for this water. It might be (1) water previously incorporated in olivine and other minerals as trace elements or (2) the rock underwent some sort of metasomatic event. In this latter case, the pseudomorph after grt1 consisted originally of spl+opx+cpx. Metasomatic events would have then inserted water into the system, partially replacing the original cpx in pargasite. Further investigations on trace elements and/or on H^+ isotopes might unravel a possible source for this water.

M2

This phase represents the reburial to UHP depth of the FGP, after crustal intrusion. M2 peak metamorphic conditions are recorded within the eclogitic dyke (3.0 GPa - 800°C ; Janàk *et al.*, 2013). In garnet peridotite, geobarometry applied to the M1a and M2 mineral assemblage record slightly lower P conditions (2.5 ± 0.4 GPa). Despite several thermometers are concordant with the results of Janàk *et al.* (2013) and indicate a $T = 800 \pm 50^\circ\text{C}$, many others record a lower $T = 650 \pm 50^\circ\text{C}$.

M3

This phase represents fast decompression of the garnet peridotite, followed by isobaric cooling, after the UHP event.

The eclogite records an isothermal decompression event from M2 UHP PT conditions to about 1.0 GPa (Janàk *et al.*, 2013). This phase is also recorded within external eclogites (Van Roermund, 1985). This M3a phase has not been recognised in the mineral assemblage of the FGP. However, several geothermometers applied on M1a and M2 mineral assemblage indicate a metamorphic re-equilibration at $T = 650 \pm 50^\circ\text{C}$.

Summary

In fig. 7.3, the final PT path of the Friningen Garnet Peridotite is documented. The figure includes all points discussed above.

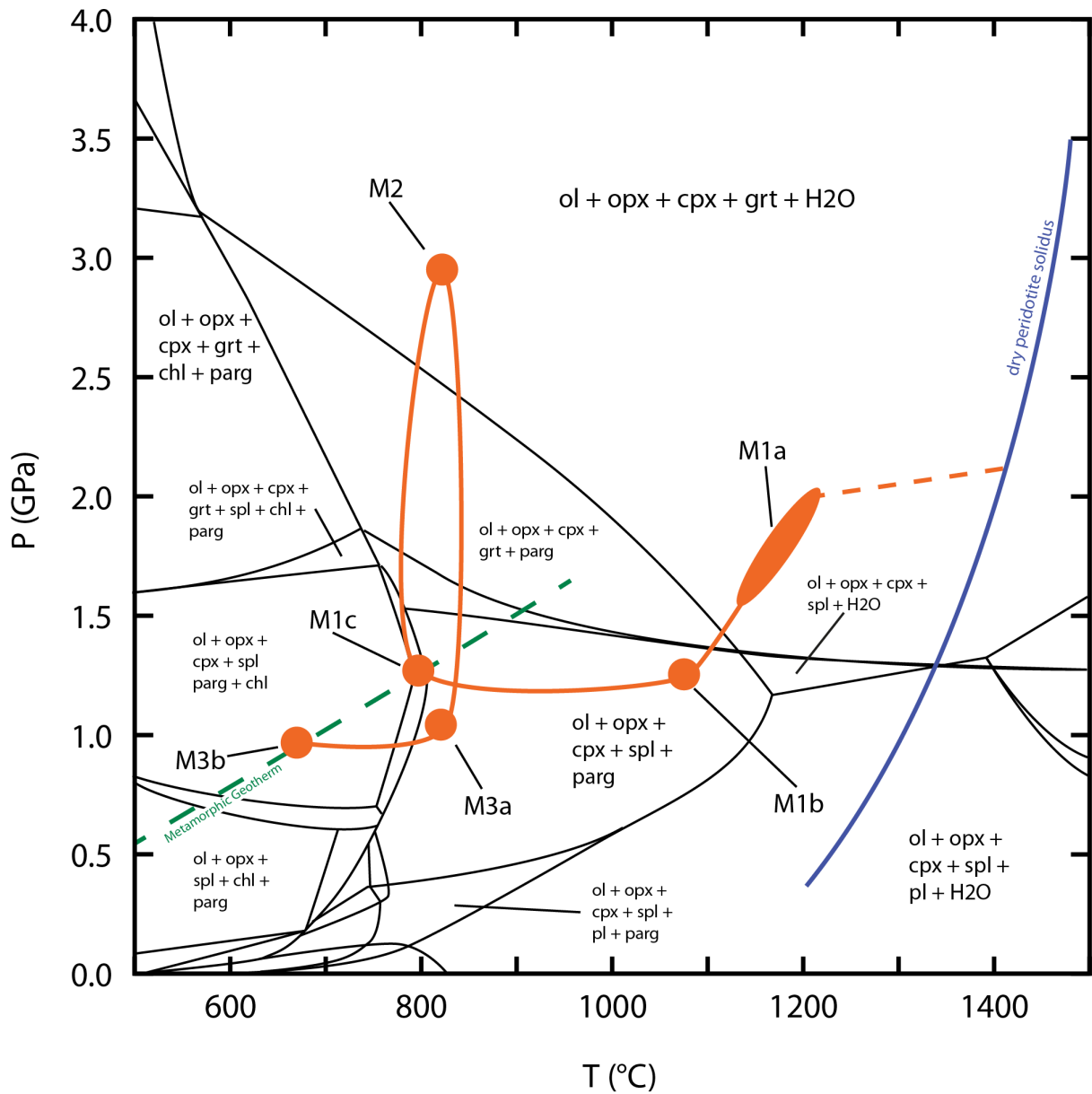


Fig. 7.3. PT path of the Friningen Garnet Peridotite. The metamorphic gradient (green dashed line) is from Bucher (1991) For a more elaborate description the reader is referred to the written text on page 63.

7.3 Slip systems and origin of water

During its mantellic history (M1), the FGP was deformed at really low differential stress (1-3 MPa) through HT-dislocation creep. This is recorded by (1) the coarse grained M1 olivines (5-10 mm) and (2) by their very strong CPO (sample F8). This CPO shows a mixture of a- and b-type olivine fabrics. As already discussed, this shift might indicate the passage from a dry to a wet environment coupled with a decrease in temperature. The graph in fig. 7.4 shows the b- to c-type fabric transition in water saturated olivines at $P = 2.0$ GPa (Katayama & Karato, 2006). At high T, b-type is expected to occur only under very high differential stress conditions. However, for lower temperatures ($T < 800^{\circ}\text{C}$) it occurs also for differential stress about 1-10 MPa.

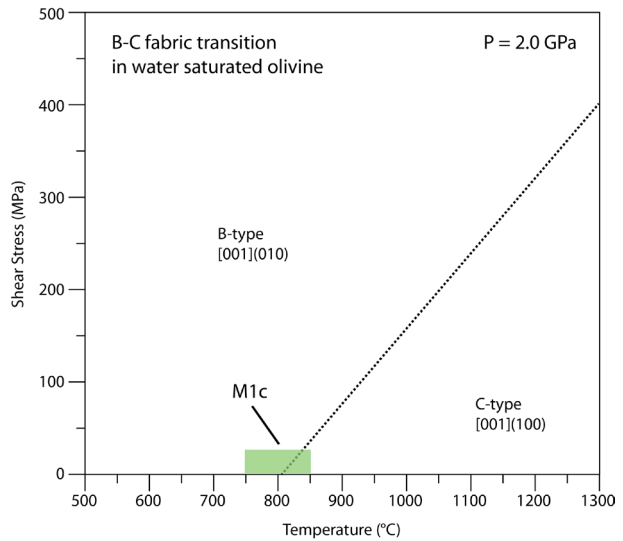


Fig. 7.4. B/C fabric transition map in temperature-stress space for water saturated olivine at $P = 2.0$ GPa. The green field displays the range for the M1a fabric ($P = 1.3-1.5$ GPa). The preset pressure is slightly higher than the inferred pressure for the M1b/M1c assemblage therefore the b-c transition line might occur at slightly higher T (Raterron *et al.*, 2007; modified after Katayama & Karato, 2006)

The a-type fabric in the M1 olivines probably reflects a very old deformation phase that, probably occurred in the mantle shortly after or during the Proterozoic refertilization event (HT - dry condition). The spl+opx+parg pseudomorphs after grt1 show a preserved vermicular structure, suggesting that the rocks did not undergo a deformation event during decompression and cooling. Between M1b and M2 (Fig. 7.3) subduction zone fluids percolated through the peridotite, adding water (and several other elements like CO_2 , Sr and Na) to the system. The interaction between mantle garnet/spinel peridotite and the subducting continental plate in the mantle is likely to be the cause for the reactivation of dislocation creep in olivine and the onset of b-type fabric.

The M1 mineral assemblage contains trains of fluid inclusions consisting of Sr-bearing carbonates, i.e. a clear indication of subduction fluid metasomatism. However, the shift from dry to wet environment might also be due to a decrease in the water solubility in olivine. A detailed study of the chemical composition of the solid+fluid inclusions might help to constrain the origin of the metasomatic fluid. Here it is proposed that the fluids are taken as being introduced at the start of subduction (M1c).

The M2 phase represents the prograde history of the FGP. During this phase intensive deformation produced a really pervasive S2 fabric throughout the body. The main deformation mechanism active in olivine is inferred to have been dislocation creep, producing a strong CPO and development of a-type fabric. This type of fabric, triggered by the activation of the $[100](010)$ slip system in olivine, is typical of hot ($T > 1100^{\circ}\text{C}$) and dry environments and it is usually found in ophiolites and/or asthenospheric mantle. However, in the FGP this a-type fabric resulted from a deformation that occurred at relatively low temperature ($T = 800^{\circ}\text{C}$) and high pressure ($P = 3.0$ GPa) with relatively wet conditions. Furthermore, the occurrence of $[100](010)$ slip is confirmed by the presence of kink bands and dislocation walls perpendicular to the $[100]$ directions.

The rheology of olivine in high pressure conditions is largely unexplored. Experimental studies (Jung & Karato, 2001; Jung *et al.*, 2006; Katayama & Karato, 2006) focussed their attention to the rheology of olivine deformed at low P and high T conditions ($P < 2.0$ GPa; $T > 1100^{\circ}\text{C}$), typical conditions for sub-oceanic mantle environments and/or asthenosphere. Raterron *et al.* (2007) explored the effect on pressure on the rheology of dry olivine. However, this author considered only the behaviour of a single dry olivine crystal. Though this first exploration already predicted the occurrence of a-type fabric in HP-LT environments, more studies should be carried out in order to apply these olivine flow laws to natural samples.

The M3 phase represents the final stages of the retrograde path of the FGP after the UHP event. The transition from M2 to M3 was probably progressive: as temperature decreased, strain localized along anatomised shear zones. Along these decimetric-sized bands, strain was too high, and T too low for dislocation creep to be the dominant deformation mechanisms. Olivines were mostly deformed through a combination of grain size sensitive creep (diffusion and/or Coble creep) and grain size insensitive creep (dislocation creep). This resulted in the production of a very small grain size (20-100 μm) and a weak e-type CPO. This fabric is typical of relatively high stress, low pressure, cold and wet condition. It has been recorded in olivine deformed under similar circumstances in the Kittelfjäll Spinel Peridotite (Clos, 2013).

7.4 Geodynamic interpretation

In this chapter, the PTt-d path of the FGP is linked to the evolution of the Seve Nappe Complex in order to better understand its geodynamic significance during the evolution of the Caledonian orogen. Geochemical, petrological and structural data discussed in the previous chapters are linked together to produce a PTt-d path of the area that can be used as an input in a geodynamic model of the area. However, the validity of this model is only restricted to the SNC. In addition, the geodynamic history of the FGP can be compared to the PTt-d history of another mantle wedge peridotite of the SNC: the Kittelfjäll Spinel Peridotite (KSP; Calon, 1979; recently studied by Clos, 2013).

According to the model of Bruecker & Van Roermund (2004) the FGP can be interpreted as a mantle wedge garnet peridotite that originates from a cold and thick lithospheric mantle wedge, underneath either Laurentia or a micro-continent positioned between Baltica and Laurentia. The M1a assemblage, including the primary assemblages of the eclogitic dyke, are interpreted to be the result of a Proterozoic recrystallization event (~ 1.5 Ga) related to refertilization of an Archean dunite body by a dyke "swarm". Absolute timing of the M1b assemblage (decompression+cooling event) is uncertain but interpreted to be related to mantle upwelling, subsequent to Iapetus Ocean spreading (570-550 Ma; Fig. 7.5a). Alternatively, this phase might be related to an even older (Proterozoic) decompression/cooling event.

The multiphase solid and fluid inclusions, present only in M1 mineral assemblages, are interpreted as evidence for a third refertilization event related to an early Caledonian subduction zone fluid infiltration event.

At the same time, the FGP became incorporated into the subducting continental crust (SNC) during "early Caledonian" subduction (450 Ma) down to UHPM conditions (M2). It is uncertain

how fast the subduction was. However, it resided at UHP depth long enough to allow UHP mineral assemblage to form.

The early Caledonian eduction phase is considered to be isothermal (M3a; 1.0 GPa - 800 °C) and followed by a slow cooling to M3b (1.0 GPa - 650-700°C). Most of the mineralogy of the peridotite underwent a strong metamorphic re-equilibration as indicated by thermobarometric calculations. An exception to this rule is given by the Cr content in M1 and M2 garnets and spinels.

This newly documented PTt-d path of the FGP, except for the M2 subduction age, resembles that of cold mantle wedge garnet peridotites from the Western Gneiss Complex (Van Roermund, 2009a; Zhang *et al*, 2011).

The Kittelfjäll Spinel Peridotite (KSP) also belongs to the Central/Middle Belt of the SNC. The rock envelope of the KSP consists of a ky+Kfs+bt gneiss (Marsfjäll gneiss) and/or a grt-cpx-pl bearing amphibolite (Kittelfjäll amphibolite). The KSP is characterized by two contrasting olivine microstructures, formed in response to retrograde tectono-metamorphic conditions (Clos, 2013). Coarse grained, highly strained olivine crystals (up to 20 cm; called M1^K porphyroclasts) are surrounded by dynamically recrystallized olivine grains (200-2000 µm) that define a characteristic olivine "foam" microstructure (called M2^K grains). The M1^K assemblage consists of coarse grained olivine, opx and spinel; the M2^K assemblage of ol+opx+spl+tr+chl.

Fig. 7.5 summarises the evolution of the two mantle fragments. Both the KSP and the FGP are interpreted to be orogenic peridotites with subcontinental affinity. Their early Caledonian PTt-d path is inferred to be roughly similar (Fig. 7.5a). However, the PTt-d path of both peridotite differ in their Caledonian evolution and crustal intrusion. The KSP was emplaced during eduction from the Laurentia mantle wedge (hanging wall) or from the Baltic mantle lithosphere (footwall).

The joined PTt-d path of the FGP and KSP gives important information about the role of the SNC during early Caledonian and Scandian collisions between Baltica and Laurentia (Gee *et al*, 2013). For the many similarities with the WGR, the SNC might be interpreted as the most external part of Baltica, detached and thrust over the sedimentary cover of the middle allochthon. However, in order to confirm this hypothesis, more studies should be carried out on the eclogite from the SNC, in order to find evidences for pre-Caledonian (>450 Ma) mineral assemblages.

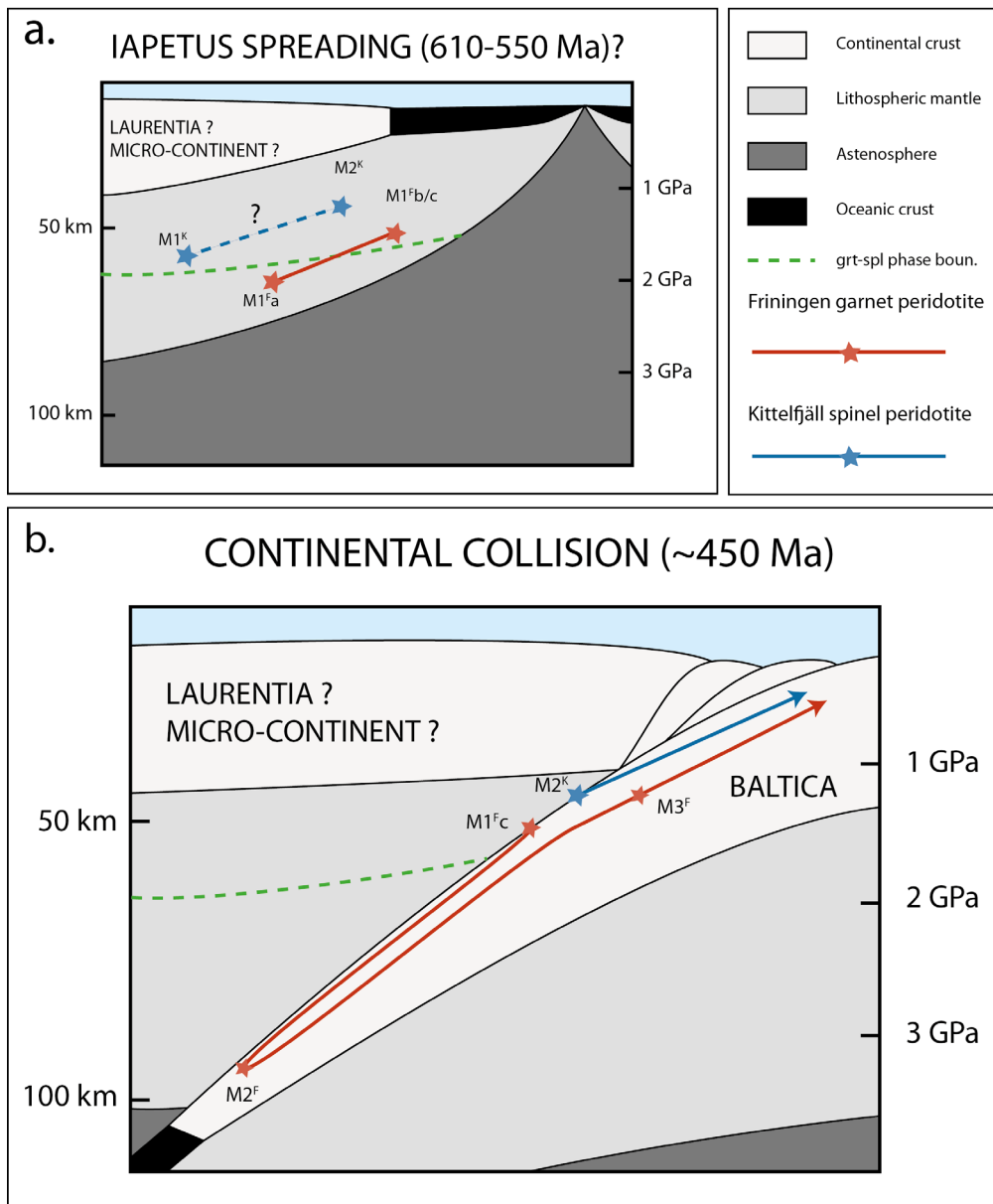


Fig. 7.5. Simplified cartoons illustrating the evolution of the Friningen Garnet Peridotite (FGP) and the Kittelfjäll Spinel Peridotite (KSP) at (a.) 610-550 Ma and (b.) ~450 Ma. (a.) The asthenospheric related to Iapetus spreading have had interpreted in this MSc thesis to be the cause of the decompression within the sub-continental lithosphere recorded in the FGP (note the transition from garnet to spinel mineral assemblage). The position of the M1 assemblage of the KSP is purely speculative, since no pressure information was obtained. (b) the FGP intruded the downgoing slab and was carried to UHP depth. The KSP only shows a retrograde fabric. As such, the KSP is interpreted to have "intruded" only during exhumation.

8 - CONCLUSION

The FGP resulted from an Archean depletion event, followed by (1) Proterozoic refertilization (1.2-1.1 Ga) by intrusion of dikes and (2) early Caledonian refertilization by the introduction of subduction zone fluids.

Pre-Caledonian HP-HT metamorphic conditions of $1125\pm 75^\circ\text{C}$ and 1.9 ± 0.4 GPa are determined for the early M1a assemblage (ol+opx+cpx+grt). These physical conditions were followed by an inferred early Caledonian exhumation event down to $1050\text{-}1100^\circ\text{C}$ and 1.5 GPa (M1b) and followed by cooling to 800°C (M1c), based on the break down of high-Cr M1a grt (ugt=6%) into opx+cpx+spl+parg symplectites (M1b) .

The early-Caledonian UHPM evidence (M2; $T=800^\circ\text{C}$ and $P=3.0$ GPa), discovered within an eclogitic dyke (Janàk *et al.*, 2013; Gee *et al.*, 2013), is displayed in the FGP by low-Cr M2 grt (ugt=3%) replacing the M1b lower P symplectite assemblage and growth of M2 garnets around M1b spinels. Pl+di symplectites after omphacite in the internal eclogitic dyke and breakdown of kyanite to sapphirine and plag and phengite to biotite and plagioclase (Janàk *et al.*, 2013) are indicative of isothermal decompression (M3a) down to 800°C and 1.0 GPa. This M3a phase has not been recognised in the mineral assemblage of the FGP. However, several geothermometers applied on M1a and M2 mineral assemblages indicate a metamorphic overprint at $T=650\pm 50^\circ\text{C}$ (M3b). An exception to this rule is formed by the Cr-content of M1a and M2 garnets.

The finding of the stable mineral assemblage dolomite+grt+ky+zoi±ph in the eclogitic dyke and of Sr-bearing carbonates in multiphase solid inclusions within M1a opx, cpx and ol indicates early (i.e. before crustal intrusion) slab-derived fluid metasomatism.

Three olivine microstructures develop in response to different deformation events and different PT conditions:

- Olivine M1 porphyroclasts grew in the mantle at HT and low differential stress (1-3 MPa). The main mechanism involved was dislocation creep, producing a mixture of a- and b-type fabric. These two fabrics are probably the result of two deformation phases, different in temperature and water content.
- Olivine M2 foam microstructure grew during subduction, after crustal intrusion. The main mechanism involved was dislocation creep, producing a-type fabric.
- Olivine M3 foam microstructure grew after strain localization along anastomosed shear zones at low T ($650\text{-}700^\circ\text{C}$) and high differential stress (70-100 MPa). The main mechanism involved was grain size sensitive creep. However, dislocation creep was also involved producing a weak e-type olivine CPO.

9 - FUTURE WORKS

1. Detailed study of the solid and/or fluid inclusions, the trace elements and the H⁺ isotopes in order to define the origin and composition of the (metasomatic) fluids.
2. A petrological and microstructural investigation of other garnet/spinel-bearing ultramafic bodies in the Seve Nappe Complex in order to establish their petrogenesis.
3. Investigations of eclogite in the Seve Nappe Complex in order to find evidence of preserved UHP mineral assemblages and/or protolith ages.

10 - ACKNOWLEDGMENTS

The first thanks goes to my parents, my father Roberto and my mother Carla. They comprehended, supported and accepted my decisions. They always advised and never decided for me concerning paths that I could take. A special thanks go to my grandfathers, my grandfather Alessandro and my grandmothers Titti and Maria, for their support, which was needed during difficult times. As my girlfriend and best friend, Stella guided me through this path. She supported me when it was most needed and helped me in choosing the right track. I thank Frediano for the nice time spent together, for our enlightening discussions, and because it is always nice to have someone to share your passion with. I thank Herman. His support, his time and his advices where vital for my intellectual growth and for the accomplishment of this work. I thank Oliver for his help with the EBSD, for the discussions and for showing me some of the wanders of the micro-world.

Il primo ringraziamento va ai miei genitori. Essi hanno sempre compreso, supportato e accettato le mie decisioni; mi hanno sempre consigliato, senza mai decidere per mio conto, la strada da percorrere. Uno speciale ringraziamento va ai miei nonni, mio nonno Alessandro e le mie nonne, Titti e Maria, per il loro supporto, essenziale nei momenti più difficili. Come mia ragazza e mia migliore amica, Stella mi ha guidato lungo il mio percorso, supportandomi quando più ne avevo bisogno e aiutandomi nelle decisioni più importanti. Ringrazio Frediano, per i bei momenti spesi insieme, per le discussioni accese e perché è sempre bello avere qualcuno con il quale si possa condividere una passione. Ringrazio Herman. Il suo supporto, la sua disponibilità e i suoi consigli sono stati vitali per la mia crescita intellettuale e per il compimento di questo lavoro. Ringrazio Oliver per il suo aiuto con l'EBSD, per le discussioni e per avermi mostrato le meraviglie del mondo microscopico.

11 - REFERENCES

- Arai, S.** (1994) - Characterization of spinel peridotites by olivine–spinel compositional relationships: review and interpretation. *Chem. Geol.* **113**, 191–204
- Avé Lallemant, H.G. & Carter, N.L.** (1970) - Syntectonic recrystallization of olivine and modes of flow in the upper mantle. *Geol. Soc. Am. Bull.* **81**, 2203–2220
- Ballhaus, C., Berry, R.F., Green, D. H.** (1991) - High pressure experimental calibration of the olivine-orthopyroxene-spinel oxygen geobarometer: implications for the oxidation state of the upper mantle. *Contrib. Mineral. Petr.* **107**, 27–40
- Bernstein, S., Kelemen, P.B., Brooks, C.K.** (1998) - Depleted spinel harzburgite xenoliths in Tertiary dykes from East Greenland: restites from high degree melting. *Earth Planet. Sc. Lett.* **154**, 221–235
- Bernstein, S.H., Kelemen, K., Peter, B., Brooks, P.B., Kent, C.** (2006) - Ultra-depleted, shallow cratonic mantle beneath West Greenland: dunitic xenoliths from Ubekendt Ejland. *Contrib. Mineral. Petr.* **152**, 335–347
- Beyer, E.E., Griffin, W.L., O'Reilly, S.Y.** (2006) - Transformation of Archaean lithospheric mantle by refertilization: evidence from exposed peridotites in the Western Gneiss Region, Norway. *J. Petrol.* **47**, 1611–1636
- Bogdanova, S., Gorbatshev, R., Stephenson, R.A., Guterch, A.** (2001) - Eurobridge: Palaeoproterozoic Accretion of Fennoscandia and Sarmatia. *Tectonophysics* **339**, 1–37.
- Bons, P.D. & Urai, J.L.** (1992) - Syndeformational grain growth: microstructures and kinetics. *J. Struct. Geol.* **14**, 1101–1109
- Brey, G.P. & Koehler, T.** (1990) - Geothermobarometry in four-phase lherzolites II: New thermobarometers, and practical assessment of existing thermobarometers. *J. Petrol.* **31**, 1353–1378
- Brey, G.P., Bulatov, V.K., Girnis, A.V.** (2008) - Geobarometry for Peridotites: Experiments in Simple and Natural Systems from 6–10 GPa. *J. Petrol.* **49**, 3–24
- Brueckner, H.K.** (1972) - Interpretation of Rb–Sr ages from the Precambrian and Palaeozoic rocks of southern Norway. *Am. J. Sci.* **171**, 334–358
- Brueckner, H.K.** (1998) - Sinking intrusion model for the emplacement of garnet-bearing peridotites into continent collision orogens. *Geology* **26**, 631–634
- Brueckner, H.K. & Medaris, L.G.** (1998) - A tale of two orogens: the contrasting TPt history and geochemical evolution of mantle in high- and ultrahigh-pressure metamorphic terranes of the Norwegian Caledonides and the Czech Variscides. *Schweiz. Mineral. Petrogr. Mitt.* **78**, 293–307.
- Brueckner, H.K. & Medaris, L.G.** (2000) - A general model for the intrusion and evolution of “mantle” garnet peridotites in high pressure and ultrahigh-pressure metamorphic terranes. *J. Metamorph. Geol.* **18**, 123–133
- Brueckner, H.K. & Van Roermund, H.L.M.** (2004) - Dunk tectonics: A multiple subduction/eduction model for the evolution of the Scandinavian Caledonides. *Tectonics* **23**, TC2004 1–20
- Brueckner, H.K. & Van Roermund, H.L.M.** (2007) - Concurrent HP metamorphism on both margins of Iapetus: Ordovician ages for eclogites and garnet pyroxenites from the Seve Nappe Complex, Swedish Caledonides. *J. Geol. Soc. London* **164**, 117–128
- Brueckner, H.K., Carswell, D.A., Griffin, W.L.** (2002) - Paleozoic diamonds within a Precambrian peridotite lens in UHP gneisses of the Norwegian Caledonides. *Earth Planet. Sc. Lett.* **203**, 805–816

- Brueckner, H.K., Van Roermund, H.L.M. & Pearson, N.** (2004) - An Archean to Paleozoic evolution for a garnet peridotite lens with sub-Baltic Shield affinity within the Seve Nappe Complex of Jämtland, Sweden, Central Scandinavia Caledonides. *J. Petrol.* **43**, 415–437
- Bryhni, I., & Andréasson, P.G.** (1985) - Metamorphism in the Scandinavian Caledonides. In: *Gee, D.G. & Sturt, B.A. (eds.), The Caledonide Orogen - Scandinavia and Related Areas.* Chichester, John Wiley and Sons, 763-782
- Bryhni, I., & Grimstad, E.** (1970) - Supracrustal and infracrustal rocks in the Gneiss Region of the Caledonides west of Breimsvatn. *Norges geol. Unders.* **266**, 105-140
- Bucher, K.** (1991) - Mantle fragments in the Scandinavian Caledonides. *Tectonophysics* **190**, 173-192
- Bystricky, M., Kunze, K., Burlini, L., Burg, J.-P.**, (2000) - High shear strain of olivine aggregates: rheological and seismic consequences. *Science* **290**, 1564 – 1567
- Calon, T.J.**, (1979) - A study of the alpine-type peridotites in the Seve-Koli Nappe Complex Central Swedish Caledonides with special reference to the Kittelfjäll peridotite. *Doct. Thesis, Univ. of Leiden*, 236 pp.
- Carswell, D.A. & Harley, S.L.** (1990) - Mineral barometry and thermometry. In: *Carswell, D.A. Ed. , Eclogite Facies Rocks.* Blackie, Glasgow, pp. 83–110
- Carswell, D.A. & Van Roermund, H.L.M.** (2005) - On multi-phase mineral inclusions associated with microdiamond formation in mantle-derived peridotite lens at Bardane on Fjørtoft, west Norway. *Eur. J. Min.* **17**, 31-42
- Carswell, D.A., Brueckner, H.K., Cuthbert, S.J., Mehta, K., O'Brien P. J.** (2003), The timing of stabilization and the exhumation rate for ultra- high pressure rocks in the Western Gneiss Region of Norway. *J. Metamorph. Geol.*, **21**, 601–612
- Carter, N.L., Avé Lallemant, H.G.**, (1970) - High temperature flow of dunite and peridotite. *Geol. Soc. Am. Bull.* **81**, 2181 – 2202
- Chopin, C.** (1984) - Coesite and pure pyrope in high-grade blueschists of the Western Alps: a first record and some consequences. *Contrib. Mineral. Petr.* **86**, 107-118
- Clos, F.** (2013) - Retrograde olivine fabrics in cold, ultra-depleted spinel mantle wedge peridotite in the Seve Nappe Complex (central Swedish Caledonides). *MSc thesis, Utrecht University, The Netherlands.*
- Condie, K.C.** (1997) - Plate Tectonics and Crustal Evolution. Butterworth-Heinemann Ltd. (4th Edition); Oxford, UK, 282 p.
- Connolly, J.A.D.** (2009) - The geodynamic equation of state: what and how. *Geochemistry, Geophysics, Geosystems* **10**, Q10014. DOI:10.1029/2009GC002540
- Cuthbert, S.J. & Carswell, D.A.** (1990) - Formation and exhumation of medium-temperature eclogites in the Scandinavian Caledonides. In: *Carswell, D.A. Ed. , Eclogite Facies Rocks.* Blackie, Glasgow, pp. 180–203.
- Den Hartog, S.A.M.** (2009) - Microphysics of Subgrain Development and Dynamic Recrystallization with Implications for Strength Evolution in trans-lithospheric Shear Zones. *MSc thesis, Utrecht University, The Netherlands.*
- Den Tex, E.** (1969) - Origin of Ultramafic Rocks, their Tectonic Setting and History: A Contribution to the Discussion of the Paper “The Origin of Ultramafic and Ultrabasic Rocks” by P.J. Wyllie. *Tectonophysics* **7**, 457-488
- Dobrzhinetskaya, L.F., Eide, E.A., Larsen, R.B., Smith, D.C., Sturt, B.A., Trønnes, R.G., Taylor, W.R., Poshukhova, T.V.** (1995) - Microdiamonds in high-grade metamorphic rocks from the Western Gneiss Region, Norway. *Geology* **23**, 597–600
- Drury, M.R., Vissers, R.L.M., Van der Wal, D., Hoogerduijn Strating, E.H.** (1991) – Shear localization in the Upper Mantle. *Pure Appl. Geophys.* **137**, 439-460

- Du Rietz, T.** (1935) - Peridotites, Serpentine, and Soapstones of Northern Sweden, with special reference to some occurrences in Northern Jämtland. *Geol. Fören. Stock. För.* **57**, 133-260
- Ellis, D.J. & Green, D.H.** (1979) - An experimental study of the effect of Ca upon garnet-clinopyroxene Fe-Mg exchange equilibria. *Contrib. Mineral. Petr.* **71**, 13-22
- Ernst, W.G., Maruyama, S., Wallis, S.** (1997) - Buoyancy-driven, rapid exhumation of ultrahigh-pressure metamorphosed continental crust. *P. Natl. Acad. Sci. USA* **94**, 9532-9537
- Evans, B. W. & Trommsdorff, V.** (1978) - Petrogenesis of garnet-lherzolite, Cima Di Gagnone, Lepontine Alps. *Earth Planet. Sc. Lett.* **40**, 333-348
- Friend, C.R.L., Bennett, V.C., Nutman, A.P.** (2002) - Abyssal peridotites >3,800 Ma from southern West Greenland: field relationships, petrography, geochronology, whole-rock and mineral chemistry of dunite and harzburgite inclusions in the Itsaq Gneiss Complex. *Contrib. Mineral. Petr.* **143**, 71-93
- Gademan, M.** (2011) - Finnmarkian Monazite EMP ages in the Central belt of the Seve Nappe, north Jämtland/south Västerbotten, Sweden. *MSc thesis, Utrecht University, The Netherlands.*
- Gee, D. G., Fossen, H., Henriksen, N., Higgins, A.K.** (2008) - From the Early Paleozoic Platforms of Baltica and Laurentia to the Caledonide Orogen of Scandinavia and Greenland. *Episodes* **31**, 44-51
- Gee, D. G., Marian, J., Majka, J., Robinson, P., Van Roermund, H.L.M.** (2013) - Subduction along and within the Baltoscandian margin during the closing of the Iapetus Ocean and Baltica-Laurentia collision. *Lithosphere* **5**, 169-178
- Gee, D.G.** (1975) - A tectonic model for the central part of the Scandinavian Caledonides. *Am. J. Sci.* **275**, 468-515
- Gorbatshev, R.** (1985) - Precambrian basement of the Scandinavian Caledonides. In: *Gee, D.G. & Sturt, B.A. (eds.), The Caledonide Orogen — Scandinavia and Related Areas. Chichester, John Wiley and Sons*, 197-212
- Harley, S.L.** (1984) - An experimental study of the partitioning of Fe and Mg between garnet and orthopyroxene. *Contrib. Mineral. Petr.* **86**, 353-373
- Hartz, E.H. & Torsvik, T.H.** (2002) - Baltica upside down: a new plate tectonic model for Rodinia and the Iapetus Ocean. *Geology* **30**, 255-258
- Herzberg, C.** (2004) - Geodynamic information in peridotite petrology. *J. Petrol.* **45**, 2507-2530
- Hogerwerf, M.** (2010) - Age dating project in the Central Belt of the Seve Nappe Complex of Southern Västerbotten, Sweden, leading to a construction of a new geodynamic model of the formation of the Caledonian Orogeny. *MSc thesis, Utrecht University, The Netherlands.*
- Holland, T.J.B., Powell, R., 1998.** *An internally consistent thermodynamic data set for phases of petrological interest. J. Metamorph Geol.* **16**, 309-344
- Iyer, K., Austrheim, H., John, T., Jamtveit, B.** (2007) - Serpentinization of the oceanic lithosphere and some geochemical consequences: Constraints from the Leka Ophiolite Complex, Norway. *Chem. Geol.* **249**, 66-90
- Janák, M., Van Roermund, H.L.M., Majka, J.C., Gee, D.G.** (2013) - UHP metamorphism recorded by kyanite-bearing eclogite in the Seve Nappe Complex of northern Jämtland, Swedish Caledonides. *Gondwana Research* **23**, 865-879
- Jung, H. & Karato, S.I.** (2001) - Water-Induced Fabric Transitions in Olivine. *Science* **293**, 1460-1463
- Jung, H., Katayama, I., Jiang, Z., Hiraga, T., Karato, S.** (2006) - Effect of water and stress on the lattice-preferred orientation of olivine. *Tectonophysics* **421**, 1-22
- Karato, S.I.** (1988) - The role of recrystallization in the preferred orientation of olivine. *Phys. Earth Planet. In.* **51**, 107-122

- Katayama, I. & Karato, S.** (2006) - Effect of temperature on the B- to C-type olivine fabric transition and implication for flow pattern in subduction zones. *Phys. Earth Planet. In.* **157**, 33–45
- Katayama, I., Jung, H., Karato, S.** (2004) - A new type of olivine fabric at modest water content and low stress. *Geology* **32**, 1045–1048
- Kohlstedt, D.L., Goetze, C., Durham, W.B., Vander Sande, J.** (1976) - New technique for decorating dislocations in olivine. *Science* **191**, 1045–1046.
- Krogh Ravna E.** (2000) The garnet–clinopyroxene Fe²⁺–Mg geothermometer: an updated calibration. *J. Metamorph. Geol.* **18**, 211–219
- Krogh Ravna, E.J. & Paquin, J.** (2003) - Thermobarometric methodologies applicable to eclogites and garnet peridotites. In: Carsweel, D.A. & Compagnoni, R. (eds.) - *Ultrahigh pressure metamorphism: Budapest, Hungary, Eötvös University Press, EMU Notes in Mineralogy* **5**, 229–259
- Krogh, E. J.** (1988). *The garnet-clinopyroxene Fe-Mg-geothermometer—a reinterpretation of existing experimental data. Contrib. Mineral. Petr.* **99**, 44–48.
- Krogh, T. E., Kamo, S. L., Robinson, P., Terry, M. P., Kwok, K.** (2011) - U–Pb zircon geochronology of eclogites from the Scandian Orogen, northern Western Gneiss Region, Norway: 14–20 million years between eclogite crystallization and return to amphibolite-facies conditions. *Can. J. Earth Sci.* **48**, 441–472
- Krogh, T., Robinson, P., Terry, M.P.** (2003) Precise U–Pb zircon ages define 18 and 19 m.y. subduction to uplift intervals in the Averøya-Nordøyane area, Western Gneiss Regions. In: Eide, E.E., editor. *The Alice Wain Memorial West Norway Eclogite Field Symposium, abstract volume* 70–71
- Leake, B.E., Woolley, A.R., Arps, C.E.S., et al.** (1997) - Nomenclature of amphiboles: report of the Subcommittee on Amphiboles of the International Mineralogical Association, Commission on New Minerals and Mineral Names. *Am. Mineral.* **82**, 1019–1037
- Medaris, L.G. & Carswell, D.A.** (1990) - Petrogenesis of Mg–Cr garnet peridotites in European metamorphic belts. In: *Eclogite facies rocks*, D.A. Carswell, ed. Blackie, Glasgow, 260–290.
- Meert, J.G. & Torsvik, T.H.** (2003) - The making and unmaking of a supercontinent: Rodinia revisited. *Tectonophysics* **375**, 261–268
- Mørk, M.B.E., Kullerud, K. V., Stabel, A.** (1988) - Sm–Nd dating of Svecofennian eclogites Norrbotten, Sweden: evidence for early Caledonian (505Ma) subduction. *Contrib. Mineral. Petr.* **99**, 344–351
- Nakamura, D. & Hirajima, T.** (2005) Experimental evaluation of garnet-clinopyroxene thermometry as applied to eclogites. *Contrib. Mineral. Petr.*, **150**, 581–588
- Nickel, K.G. & Green, D.H.** (1985) - Empirical geothermobarometry for garnet peridotites and implications for the nature of the lithosphere, kimberlites and diamonds. *Earth Planet. Sc. Lett.* **73**, 158–170
- O'Neill, H.St.C. & Wall, V.J.** (1987) The olivine-orthopyroxene-spinel oxygen geobarometer, the nickel precipitation curve, and the oxygen fugacity of the Earth's upper mantle. *J. Petrol.*, **28**, 1169–1191
- O'Neill, H.St.C. & Wood, B.J.** (1979) - An experimental study of Fe–Mg-partitioning between garnet and olivine and its calibration as a geothermometer. *Contrib. Mineral. Petr.* **70**, 59–70
- Passchier, C.W. & Trouw, R.A.J.** (2006) - *Microtectonics*. Springer-Verlag Berlin Heidelberg edition
- Poirier, J.P.** (1975) On the slip systems of olivine. *J. Geophys. Res.* **80**, 4059–4061
- Powell, R.** (1985) - Regression diagnostics and robust regression in geothermometer/geobarometer calibration: the garnet-clinopyroxene geothermometer revisited. *J. Metamorph. Geol.* **3**, 231–43

- Qvale, H., & Stigh, J.** (1985) - Ultramafic rocks in the Scandinavian Caledonides. In: *Gee, D.G. & Sturt, B.A. (eds.), The Caledonide Orogen — Scandinavia and Related Areas*. Chichester, John Wiley and Sons, 693-716
- Raterron, P., Chen, J., Weidner, D., Cordier, P.** (2007) - Pressure-induced slip-system transition in forsterite: Single-crystal rheological properties at mantle pressure and temperature. *Am. Min.* **92**, 1436-1445
- Roberts, D.** (2003) - The Scandinavian Caledonides: event chronology, palaeogeographic settings and likely modern analogues. *Tectonophysics* **365**, 283-299
- Roberts, D. & Gee, D.G.** (1985) - An introduction to the structure of the Scandinavian Caledonides. In: *Gee, D.G. & Sturt, B.A. (eds.), The Caledonide Orogen — Scandinavia and Related Areas*. Chichester, John Wiley and Sons, 55-68
- Roberts, D., Heldal, T., Melezhik, V.M.** (2001) - Tectonic structural features of the Fauske conglomerates in the Løvgavlén quarry, Nordland, Norwegian Caledonides, and regional implications. *Nor. Geol. Tidsskr.* **81**, 245– 256
- Robinson, P.** (2003) - Tectonostratigraphic setting, structure and petrology of HP and UHP metamorphic rocks and garnet peridotites in the Western Gneiss Region, Møre og Romsdal, Norway. *NGU Report* **2003**, 98–103
- Root, D. & Corfù, F.** (2012) - U-Pb geochronology of two discrete Ordovician high-pressure metamorphic events in the Seve Nappe Complex, Scandinavian Caledonides. *Contrib. Mineral. Petr.* **163**, 769-788
- Ryan, C. G., Griffin, W. L. & Pearson, N. J.** (1996) - Garnet geotherms: pressure–temperature data from Cr-pyrope garnet xenocrysts in volcanic rocks. *J. of Geophys. Res.* **101**, 5611–5625.
- Schmädicke, E., Gose, J., Will, T.M.** (2010) - The P-T evolution of ultra high temperature garnet-bearing ultramafic rocks from the Saxonian Granulitgebirge Core Complex, Bohemian Massif. *J. Metamorph. Geol.* **28**, 489-508
- Shimizu, I.** (1998) - Stress and temperature dependence of recrystallized grain size: a subgrain misorientation model. *Geophys. Res. Lett.* **25**, 4237-4240.
- Siivola, J., & Schmid, R.** (2007) - Recommendations by the IUGS Subcommittee on the Systematics of Metamorphic Rocks: List of mineral abbreviations. Web version 01.02.07. (http://www.bgs.ac.uk/scmr/docs/papers/paper_12.pdf) IUGS Commission on the Systematics in Petrology
- Spengler, D.** (2006) - Origin and evolution of deep upper mantle rocks from western Norway. *PhD thesis, Utrecht University, The Netherlands. Geol. Ultrajectina* **266**, 1-287
- Spengler, D., Brueckner, H. K., Van Roermund, H. L.M., Drury, M.R.** (2009) - Long-lived, cold continental subduction of Baltica towards 200 km depth. *Earth Plan. Sci. Lett.* **281**, 27-35
- Stephens, M.B.** (1988) - The Scandinavian Caledonides: a complexity of collisions. *Geol. Today* **4**, 20-26.
- Stephens, M.B. & Gee, D.G.** (1985) - A tectonic model for the evolution of the eugeoclinal terranes in the central Scandinavian Caledonides. In: *Gee, D.G., Sturt, B.A. (Eds.), The Caledonide Orogen—Scandinavia and Related Areas*. Wiley, Chichester, 953– 970.
- Taylor, W.R.** (1998) - An experimental test of some geothermometer and geobarometer formulations for upper mantle peridotites with application to the thermobarometry of fertile lherzolite and garnet websterite. *Neues Jb. Miner. Abh.* **172**, 381-408.
- Torsvik, T.H.** (2003) - The Rodinia Jigsaw Puzzle. *Science* **300**, 1379-1381.
- Van der Wal, D., Chopra, P., Drury, M., Fitz Gerald, J.,** (1993) - Relationships between dynamically recrystallized grain size and deformation conditions in experimentally deformed olivine rocks. *Geophys. Res. Lett.* **20**, 1479–1482
- Van Roermund, H.L.M.** (1985) - Eclogites of the Seve Nappe, central Scandinavian Caledonides. In: *D.G. Gee & B.A. Sturt (Eds.): The Caledonide Orogen – Scandinavia and related areas, John Wiley & Sons*, 873–886

- Van Roermund, H.L.M.** (1989) - High-pressure ultramafic rocks from the allochthonous nappes of the Swedish Caledonides. In: *Gayer, R.A. (Ed.), The Caledonide Geology of Scandinavia. Graham & Trotman, London*, 205-219
- Van Roermund, H.L.M.** (2009a) - Recent progress in Scandian ultrahigh-pressure metamorphism in the northernmost domain of the Western Gneiss Complex, SW Norway: continental subduction down to 180200 km depth. *J. Geol. Soc.* **166**, 739-751
- Van Roermund, H.L.M.** (2009b) - Mantle-wedge garnet peridotites from the northernmost ultra-high pressure domain of the Western Gneiss Region, SW Norway. *Eur. J. Min.* **21**, 1085-1096
- Van Roermund, H.L.M. & Drury, M. R.** (1998) - Ultra-high pressure ($P > 6$ GPa) garnet peridotites in Western Norway: exhumation of mantle rocks from > 185 km depth. *Terra Nova* **10**, 295-301
- Van Roermund, H.L.M., Bakker, E.** (1983) - Structure and metamorphism of the Tängen-Inviken area, Seve Nappes. *Central Scandinavian Caledonides GFF* **105**, 301-319.
- Van Roermund, H.L.M., Carswell, D.A., Drury, M.R., Heijboer, T.C.** (2002), Microdiamonds in a megacrystic garnet websterite pod from Bardane on the island of Fjortoft, western Norway: Evidence for diamond formation in mantle rocks during deep continental subduction. *Geology* **30**, 959-962
- Verbaas, J. & Van Roermund, H.L.M.,** (2012) - The tectonometamorphic evolution of the Friningen peridotite lens, N. Jämtland, Sweden. E-Book by Lambert. 88 pp.
- Von Blanckenburg & F., Davies, J.H.** (1995) - Slab breakoff: a model for syncollisional magmatism and tectonics in the Alps. *Tectonics* **14**, 120-131.
- Vrijmoed, J.C., Van Roermund, H.L.M., Davies, G.R.** (2006) - Evidence for diamond-grade ultra-high pressure metamorphism and fluid interaction in the Svartberget Fe-Ti garnet peridotite-websterite body, Western Gneiss Region, Norway. *Mineralogy and Petrology* **88**, 381-405
- Walter, M.J.,** (1998) - Melting of garnet peridotite and the origin of komatiite and depleted lithosphere. *J. Petrol.* **39**, 29-60
- Williams, P.F. & Zwart, H.J.** (1977) - A model for the development of the Seve-Köli Caledonian Nappe Complex. In: *Saxena, S.K., Bhattacharji, S. (Eds.), Energetics of Geological Processes. Springer-Verlag*, 170-187
- Witt-Eickschen, G.E. & Seck, H.A.** (1991) - Solubility of Ca and Al in orthopyroxene from spinel peridotite: an improved version of an empirical geothermometer. *Contrib. Mineral. Petr.* **106**, 431-439
- Zarichsson, E.** (1973) - Structural geology of the Marsfjällen area, Caledonides of Västerbotten, Sweden. *Sveriges Geol. Unders.* **689**, 1-115.
- Zhang, C., Van Roermund, H.L.M., Zhang, L.F** (2011) - 16 - Orogenic Garnet Peridotites: Tools to Reconstruct Paleogeodynamic Settings of Fossil Continental Collision Zones. In: *Ultrahigh Pressure Metamorphism, 25 Years After The Discovery Of Coesite And Diamond. London*.
- Zhang, S. & Karato, S.,** (1995) - Lattice preferred orientation of olivine aggregates deformed in simple shear. *Nature* **375**, 774-777
- Zwart, H.J.** (1974) - Structure and metamorphism in the Seve-Köli Nappe Complex (Scandinavian Caledonides) and its implications concerning the formation of metamorphic nappes. In: *Bellière, J. & Duchesne, J.C. (eds) Géologie des Domaines Cristallins. Centenaire de la Société Géologique de Belgique, Liège*, 129-144

APPENDIX 1 - MINERAL CHEMISTRY

Table A1.1 - Olivines in garnet peridotite (F8) and dunite (F7)

Section	F7	F7	F7	F7	F7	F7	F7	F7	F7	F7	F7	F7	F7	F7	F8	F8
Assemblage	M2	M2	M2	M2	M2	M2	M2	M2	M2	M2	M2	M2	M2	M2	M1	M1
N°	1	2	3	4	5	6	7	8	9	10	11	12	13	14	15	16
SiO ₂	40.38	40.57	41.10	40.88	40.75	40.59	40.83	40.99	40.95	40.82	40.63	40.82	40.61	40.94	39.86	40.02
Cr ₂ O ₃	0.00	0.00	0.02	0.00	0.01	0.00	0.00	0.00	0.00	0.02	0.00	0.00	0.00	0.02	0.00	0.00
FeO	6.80	6.50	7.42	7.41	7.37	7.42	7.55	7.41	7.43	7.27	7.50	7.43	7.72	7.33	10.14	8.95
MnO	0.06	0.09	0.07	0.07	0.09	0.10	0.10	0.08	0.07	0.08	0.10	0.07	0.08	0.10	0.09	0.08
MgO	50.19	50.68	50.25	50.41	50.12	49.38	49.83	50.25	50.32	50.20	50.00	50.14	49.99	50.64	49.60	49.56
NiO	0.44	0.44	0.45w	0.40	0.39	0.43	0.39	0.40	0.43	0.43	0.40	0.41	0.43	0.40	0.41	0.34
CaO	0.00	0.00	0.00	0.00	0.00	0.00	0.00	0.00	0.00	0.00	0.00	0.00	0.00	0.00	0.00	0.00
Totals	97.87	98.28	99.31	99.17	98.73	97.92	98.70	99.13	99.19	98.81	98.63	98.87	98.84	99.42	100.10	98.95
Mg*	93.1%	93.6%	92.3%	92.4%	92.4%	92.2%	92.2%	92.4%	92.4%	92.5%	92.2%	92.3%	92.2%	92.7%	92.2%	92.1%

Table A1.1 - Olivines in garnet peridotite (F8) and dunite (F7) - continued (1)

Section	F8	F8	F8	F8	F8	F8	F8	F8	F8	F8	F8	F8	F8	F8	F8	F8
Assemblage	M1	M1	M1	M1	M1	M1	M1	M1	M1	M1	M1	M2	M2	M2	M2	M2
N°	17	18	19	20	21	22	23	24	25	26	27	28	29	30	31	32
SiO ₂	40.40	39.48	39.88	40.23	40.16	40.10	40.50	40.62	40.53	40.37	40.55	40.45	39.75	40.24	40.07	40.29
Cr ₂ O ₃	0.00	0.00	0.00	0.00	0.00	0.00	0.00	0.00	0.00	0.00	0.00	0.01	0.01	0.00	0.00	0.00
FeO	9.09	9.23	9.23	9.31	9.21	9.24	8.95	9.08	9.42	9.25	9.19	9.25	9.06	9.45	9.31	8.73
MnO	0.07	0.08	0.07	0.07	0.10	0.10	0.09	0.08	0.09	0.10	0.08	0.06	0.08	0.08	0.07	0.08
MgO	49.75	49.38	49.68	49.83	49.67	49.37	49.18	49.15	49.14	48.75	48.87	49.82	49.35	49.67	49.70	49.69
NiO	0.41	0.37	0.38	0.36	0.38	0.39	0.34	0.41	0.36	0.40	0.39	0.39	0.42	0.33	0.39	0.46
CaO	0.00	0.01	0.00	0.00	0.00	0.00	0.00	0.00	0.01	0.00	0.01	0.00	0.01	0.00	0.00	0.00
Totals	99.72	98.55	99.24	99.79	99.51	99.20	99.05	99.33	99.55	98.86	99.08	99.99	98.68	99.76	99.54	99.25
Mg*	91.8%	92.7%	92.5%	92.0%	92.0%	91.7%	90.9%	90.7%	90.7%	90.5%	90.5%	91.7%	92.3%	91.8%	92.1%	92.0%

Table A1.1 - Olivines in garnet peridotite (F8) and dunite (F7) - continued (2)

Section	F8	F8	F8	F8	F8	F8	F8	F8	F8	F8	F8	F8	F8
Assemblage	M2	M2	M2	M2	M2	M2	M2	M2	M2	M2	M2	M2	M2
N°	33	34	35	36	37	38	39	40	41	42	43	44	
SiO ₂	40.46	39.80	39.92	40.10	40.29	40.45	40.03	40.25	40.38	40.46	40.52	40.66	
Cr ₂ O ₃	0.02	0.00	0.00	0.00	0.02	0.02	0.00	0.00	0.00	0.00	0.00	0.01	
FeO	9.12	8.96	9.06	8.95	9.28	8.97	9.25	9.23	9.09	9.08	9.01	9.19	
MnO	0.05	0.09	0.09	0.07	0.08	0.00	0.06	0.09	0.09	0.08	0.08	0.09	
MgO	49.67	49.32	49.10	48.95	49.17	49.18	49.60	49.24	48.79	49.10	48.73	49.30	
NiO	0.42	0.44	0.39	0.38	0.37	0.00	0.38	0.40	0.41	0.38	0.34	0.35	
CaO	0.00	0.00	0.00	0.00	0.00	0.05	0.01	0.00	0.00	0.00	0.00	0.00	
Totals	99.74	98.61	98.56	98.46	99.21	98.67	99.34	99.22	98.77	99.10	98.67	99.60	
Mg*	91.6%	92.2%	91.7%	91.2%	91.2%	90.7%	92.1%	91.3%	90.5%	90.8%	90.6%	90.7%	

Table A1.2 - Orthopyroxenes in garnet peridotite (F8) and dunite (F7)

Section	F8	F8	F8	F8	F8	F8	F8	F8	F8	F8	F8	F8	F8	F8	F8	F8	
Assemblage	M1	M1	M1	M1	M1	M1	M1	M1	M1	M1	M1	M1	M2	M2	M2	M1b (grt incl.)	M1b (grt incl.)
N°	1	2	3	4	5	6	7	8	9	10	11	12	13	14	15	16	
SiO2	55.68	56.42	55.65	56.63	57.26	57.20	56.93	56.62	56.73	57.02	56.91	56.99	56.42	56.77	56.68	56.70	
TiO2	0.05	0.06	0.07	0.05	0.03	0.05	0.05	0.10	0.11	0.05	0.07	0.03	0.07	0.07	0.02	0.00	
Al2O3	1.13	1.17	1.78	1.39	1.00	1.13	1.32	1.15	1.47	1.13	1.06	1.11	1.09	1.17	1.46	1.61	
Cr2O3	0.22	0.23	0.24	0.21	0.18	0.17	0.18	0.19	0.22	0.19	0.24	0.17	0.36	0.18	0.19	0.26	
FeO	6.43	6.00	5.89	6.01	5.97	5.98	6.23	5.91	5.95	5.91	5.93	6.06	6.18	6.36	5.52	5.43	
MnO	0.12	0.12	0.10	0.11	0.11	0.11	0.15	0.09	0.08	0.09	0.10	0.10	0.10	0.12	0.08	0.06	
MgO	34.59	35.15	34.81	34.95	34.86	34.31	34.31	34.71	34.43	34.78	34.95	34.55	34.40	34.69	34.54	35.05	
CaO	0.28	0.19	0.17	0.16	0.16	0.16	0.17	0.19	0.32	0.14	0.15	0.15	0.18	0.17	0.16	0.15	
Na2O	0.01	0.01	0.00	0.02	0.03	0.02	0.00	0.00	0.00	0.00	0.01	0.03	0.00	0.00	0.03	0.00	
Total	98.51	99.34	98.70	99.54	99.61	99.12	99.36	98.95	99.31	99.31	99.40	99.18	98.81	99.53	98.66	99.26	

Table A1.2 - Orthopyroxenes in garnet peridotite (F8) and dunite (F7) - continued (1)

Section	F8	F8	F8	F8	F8	F8	F7	F7	F7	F7	F7
Assemblage	M1b (grt incl.)	M1b (grt incl.)	M1b (grt incl.)	M1b (grt incl.)	M1b (grt incl.)	M1b (grt incl.)	M2	M2	M2	M2	M2
N°	17	18	19	20	21	22	23	24	25	26	27
SiO2	56.60	56.54	57.18	56.46	56.70	57.37	57.39	57.55	57.30	57.46	57.16
TiO2	0.03	0.01	0.01	0.02	0.02	0.05	0.04	0.00	0.01	0.00	0.01
Al2O3	1.41	1.58	1.68	2.03	1.88	1.03	1.17	0.97	1.16	1.26	1.31
Cr2O3	0.17	0.24	0.19	0.19	0.20	0.20	0.53	0.73	0.33	0.22	0.25
FeO	5.53	5.61	5.26	5.31	5.26	5.44	5.01	5.01	5.17	5.15	5.10
MnO	0.09	0.07	0.07	0.09	0.08	0.18	0.11	0.13	0.13	0.11	0.13
MgO	34.98	35.01	35.13	34.73	34.71	35.63	35.49	35.56	35.55	35.30	35.57
CaO	0.19	0.16	0.15	0.15	0.20	0.20	0.17	0.14	0.17	0.19	0.19
Na2O	0.04	0.12	0.02	0.07	0.04	0.02	0.02	0.00	0.05	0.02	0.00
Total	99.05	99.34	99.71	99.04	99.09	100.12	99.92	100.08	99.88	99.71	99.72

Table A1.3 - Clinopyroxenes in garnet peridotite (F8) and dunite (F7)

Section	F8	F8	F8	F8	F8	F8	F8	F8	F8	F8
Assemblage	M1	M1	M1	M1	M1	M1	M1	M1	M2	M2
N°	1	2	3	4	5	6	7	8	9	10
SiO2	54.33	54.16	54.23	54.05	53.60	53.84	53.59	53.05	54.25	54.20
TiO2	0.20	0.22	0.17	0.21	0.20	0.19	0.20	0.20	0.14	0.18
Al2O3	2.04	2.30	2.12	2.17	2.15	2.14	2.08	2.05	2.26	2.11
Cr2O3	0.91	1.16	1.09	1.13	1.04	1.08	1.02	1.03	0.70	0.81
FeO	1.55	1.63	1.54	1.65	1.61	1.59	1.63	1.63	1.69	1.74
MnO	0.03	0.06	0.07	0.02	0.04	0.04	0.08	0.05	0.07	0.03
MgO	16.56	16.11	16.42	16.41	16.26	16.27	16.33	16.19	16.40	16.25
NiO	0.04	0.01	0.01	0.05	0.00	0.03	0.04	0.03	0.00	0.00
CaO	23.40	22.77	23.10	22.97	22.83	22.78	22.87	22.77	22.55	22.79
Na2O	1.03	1.23	1.11	1.13	1.12	1.07	1.02	1.14	1.25	1.14
Total	100.08	99.66	99.87	99.80	98.84	99.04	98.87	98.15	99.29	99.26

Table A1.4 - Garnets in garnet peridotite (F8)

Section	F8	F8	F8	F8	F8	F8	F8	F8	F8	F8	F8	F8	F8	F8	F8	F8
Assemblage	M1	M1	M1	M1	M1	M1	M1	M1	M1	M1	M1	M1	M1	M1	M1	M1
N°	1	2	3	4	5	6	7	8	9	10	11	12	13	14	15	16
SiO2	42.71	41.38	41.62	41.83	41.86	41.33	41.50	41.48	41.45	41.23	41.54	41.32	41.26	40.79	41.35	41.35
TiO2	0.21	0.05	0.08	0.09	0.06	0.19	0.17	0.10	0.04	0.02	0.10	0.17	0.07	0.06	0.05	0.07
Al2O3	20.09	21.68	21.63	21.91	21.67	21.52	21.79	21.83	21.71	21.72	21.79	21.77	21.69	21.61	21.64	21.57
Cr2O3	1.82	2.03	2.03	2.32	2.20	2.17	2.09	2.14	2.14	1.83	2.13	2.15	2.07	2.11	2.06	2.14
FeO	8.83	10.34	10.43	9.66	9.86	10.21	10.21	10.56	10.54	9.88	9.93	9.94	9.81	9.79	9.85	9.98
MnO	0.35	0.52	0.54	0.48	0.44	0.49	0.47	0.50	0.49	0.45	0.47	0.44	0.44	0.46	0.45	0.46
MgO	20.13	18.29	18.33	18.73	18.70	18.50	18.43	18.37	18.27	18.56	18.77	18.87	18.53	18.60	18.41	18.44
NiO	0.16	0.00	0.00	0.01	0.00	0.00	0.00	0.01	0.00	0.00	0.00	0.01	0.00	0.00	0.00	0.00
CaO	5.19	5.08	4.95	5.17	5.13	4.97	4.96	4.91	5.12	4.99	5.01	4.95	5.15	5.13	5.29	5.15
Total	99.49	99.38	99.60	100.21	99.91	99.39	99.63	99.91	99.76	98.69	99.73	99.62	99.02	98.55	99.10	99.15

Table A1.4 - Garnets in garnet peridotite (F8) - Continued (1)

Section	F8	F8	F8	F8	F8	F8	F8	F8	F8	F8	F8	F8
Assemblage	M1	M2	M2	M2	M2	M2	M2	M2	M2	M2	M2	M2
N°	17	18	19	20	21	22	23	24	25	26	27	27
SiO2	41.35	41.81	41.59	41.71	41.65	42.03	41.94	41.88	42.04	40.79	42.23	42.23
TiO2	0.05	0.02	0.01	0.05	0.00	0.01	0.02	0.03	0.03	0.03	0.07	0.07
Al2O3	21.74	22.50	22.57	22.47	22.84	22.73	22.53	22.82	23.04	22.37	22.88	22.88
Cr2O3	2.05	1.33	0.97	1.41	0.85	0.90	1.02	0.99	0.79	0.89	1.07	1.07
FeO	11.22	10.52	10.35	10.18	10.15	10.44	10.41	10.26	10.09	14.09	9.45	9.45
MnO	0.54	0.47	0.45	0.47	0.43	0.43	0.45	0.45	0.46	1.42	0.51	0.51
MgO	17.70	18.72	18.90	18.50	18.76	18.60	18.64	19.02	18.92	14.66	18.78	18.78
NiO	0.02	0.05	1.62	0.02	0.00	0.02	0.00	0.00	0.01	0.00	0.00	0.00
CaO	5.27	4.60	4.41	4.77	4.35	4.42	4.53	4.40	4.53	5.71	5.71	5.71
Total	99.92	100.01	100.88	99.58	99.03	99.58	99.53	99.85	99.91	99.96	100.69	100.69

Table A1.4 - Garnets in garnet peridotite (F8) - Continued (2)

Section	F8	F8	F8	F8	F8	F8	F8	F8	F8	F8	F8	F8
Assemblage	M2 (spl rim)	M2 (spl rim)	M2 (spl rim)	M2 (spl rim)	M1c (cpx incl)	M1c (cpx incl)	M1c (cpx incl)	M1c (cpx incl)	M1c (opx incl)	M1c (opx incl)	M1c (opx incl)	M1c (opx incl)
N°	28	29	30	31	32	33	34	35	36	37	38	39
SiO2	42.07	41.39	41.41	40.79	41.76	41.33	41.45	41.74	42.01	40.75	40.47	41.21
TiO2	0.07	0.04	0.04	0.06	0.04	0.04	0.05	0.06	0.02	0.03	0.07	0.03
Al2O3	22.51	22.27	22.83	22.37	22.30	22.07	22.02	22.24	22.67	22.67	22.70	22.44
Cr2O3	1.50	1.88	1.01	1.01	1.34	1.37	1.38	1.32	1.09	0.94	0.81	1.11
FeO	9.75	9.87	9.31	9.70	11.52	11.58	12.04	11.81	10.81	10.66	9.99	10.94
MnO	0.56	0.57	0.54	0.59	0.74	0.85	0.81	0.90	0.59	0.63	0.56	0.68
MgO	19.07	18.68	19.36	18.68	17.14	16.82	16.97	16.74	18.62	18.98	19.13	18.54
NiO	0.00	0.00	0.02	0.06	0.02	0.00	0.04	0.00	0.00	0.00	0.00	0.00
CaO	5.01	5.21	4.81	4.66	5.59	5.50	5.24	5.34	4.44	3.88	3.94	4.09
Total	100.53	99.92	99.34	97.91	100.44	99.57	100.00	100.13	100.26	98.54	97.67	99.04

Table A1.5 - Spinel in garnet peridotite (F8) and dunite (F7)

Section	F7	F7	F7	F7	F7	F7	F7	F7	F7	F7	F7	F7	F7	F7	F7	F7
Assemblage	M2	M2	M2	M2	M2	M2	M2	M2	M2	M2	M2	M2	M2	M2	M2	M2
N°	1	2	3	4	5	6	7	8	9	10	11	12	13	14	15	16
SiO2	0.01	0.01	0.01	0.00	0.00	0.04	0.01	0.02	0.34	0.02	0.02	0.00	0.01	0.02	0.00	0.01
TiO2	0.02	0.03	0.03	0.03	0.01	0.03	0.04	0.03	0.01	0.04	0.04	0.02	0.02	0.03	0.03	0.03
Al2O3	30.10	30.22	29.97	30.03	29.92	29.98	29.59	28.19	29.23	29.06	29.08	30.23	30.31	30.17	30.14	30.03
Cr2O3	38.03	37.77	38.09	38.19	38.14	38.17	38.68	39.69	39.32	39.30	39.06	38.29	38.44	38.44	38.22	38.54
Fe2O3	2.57	2.64	2.75	2.57	2.58	2.89	2.67	2.92	2.14	2.47	2.81	2.73	2.56	2.50	2.89	2.47
FeO	13.59	13.47	13.42	13.43	13.24	13.34	13.36	14.05	14.55	13.76	13.62	13.38	13.54	13.32	13.38	13.34
MnO	0.58	0.63	0.64	0.63	0.65	0.62	0.66	0.68	0.67	0.61	0.62	0.60	0.59	0.62	0.63	0.63
MgO	14.40	14.39	14.51	14.46	14.49	14.63	14.51	13.90	14.13	14.23	14.33	14.58	14.60	14.64	14.64	14.61
NiO	0.03	0.09	0.02	0.05	0.05	0.08	0.08	0.04	0.04	0.09	0.06	0.09	0.05	0.10	0.06	0.07
ZnO	0.26	0.32	0.28	0.31	0.30	0.28	0.25	0.24	0.29	0.28	0.26	0.37	0.28	0.27	0.24	0.28
VO	0.26	0.25	0.21	0.24	0.25	0.23	0.22	0.24	0.25	0.20	0.23	0.24	0.25	0.25	0.26	0.22
Total	99.86	99.82	99.92	99.95	99.62	100.29	100.07	100.00	100.96	100.06	100.13	100.54	100.65	100.36	100.50	100.24
Mg*	65.4%	65.6%	65.8%	65.7%	66.1%	66.2%	65.9%	63.8%	63.4%	64.8%	65.2%	66.0%	65.8%	66.2%	66.1%	66.1%
Fe2*	34.6%	34.4%	34.2%	34.3%	33.9%	33.8%	34.1%	36.2%	36.6%	35.2%	34.8%	34.0%	34.2%	33.8%	33.9%	33.9%
Cr*	45.9%	45.6%	46.0%	46.0%	46.1%	46.1%	46.7%	48.6%	47.4%	47.6%	47.4%	45.9%	46.0%	46.1%	46.0%	46.3%
Fe3*	2.9%	2.9%	3.1%	2.9%	2.9%	3.2%	3.0%	3.3%	2.4%	2.8%	3.1%	3.0%	2.8%	2.8%	3.2%	2.7%

Table A1.4 - Spinel in garnet peridotite (F8) and dunite (F7) - continued (1)

Section	F7	F7	F7	F7	F7	F7	F7	F7	F7	F7	F7	F7	F7	F7	F7	F7
Assemblage	M2	M2	M2	M2	M2	M2	M2	M2	M2	M2	M2	M2	M2	M2	M2	M2
N°	17	18	19	20	21	22	23	24	25	26	27	28	29	30	31	32
SiO2	0.01	0.01	0.01	0.00	0.00	0.02	0.01	0.00	0.00	0.01	0.02	0.03	0.09	0.07	0.04	0.02
TiO2	0.03	0.02	0.01	0.04	0.03	0.02	0.04	0.06	0.02	0.03	0.05	0.03	0.03	0.03	0.04	0.05
Al2O3	29.97	29.79	29.58	29.65	29.39	29.96	29.10	29.40	26.95	28.61	28.05	28.01	28.46	27.59	28.66	28.15
Cr2O3	38.76	38.78	38.91	38.81	39.19	38.78	39.46	39.11	41.15	39.56	40.43	39.06	39.54	40.26	39.69	40.04
Fe2O3	2.95	2.79	2.75	2.78	2.69	2.73	2.39	2.51	3.03	2.85	2.38	3.01	2.57	2.89	2.52	2.79
FeO	13.53	13.32	13.47	13.46	13.73	13.70	14.02	13.85	14.33	13.99	14.47	14.38	13.94	14.25	14.77	14.59
MnO	0.61	0.61	0.63	0.59	0.60	0.57	0.60	0.60	0.67	0.62	0.61	0.62	0.61	0.62	0.58	0.58
MgO	14.67	14.66	14.51	14.56	14.37	14.54	14.13	14.26	13.58	14.07	13.70	13.53	14.02	13.81	13.74	13.70
NiO	0.05	0.11	0.10	0.09	0.04	0.06	0.05	0.06	0.10	0.09	0.08	0.09	0.08	0.05	0.04	0.07
ZnO	0.27	0.24	0.24	0.26	0.26	0.29	0.22	0.28	0.26	0.19	0.24	0.22	0.28	0.19	0.12	0.25
VO	0.25	0.23	0.23	0.22	0.24	0.25	0.25	0.25	0.28	0.26	0.27	0.26	0.27	0.26	0.24	0.25
Total	101.10	100.56	100.42	100.47	100.55	100.93	100.28	100.38	100.37	100.28	100.30	99.24	99.88	100.02	100.44	100.48
Mg*	65.9%	66.2%	65.8%	65.9%	65.1%	65.4%	64.2%	64.7%	62.8%	64.2%	62.8%	62.6%	64.2%	63.3%	62.4%	62.6%
Fe2*	34.1%	33.8%	34.2%	34.1%	34.9%	34.6%	35.8%	35.3%	37.2%	35.8%	37.2%	37.4%	35.8%	36.7%	37.6%	37.4%
Cr*	46.5%	46.6%	46.9%	46.8%	47.2%	46.5%	47.6%	47.2%	50.6%	48.1%	49.2%	48.3%	48.2%	49.5%	48.2%	48.8%
Fe3*	3.3%	3.1%	3.1%	3.1%	3.0%	3.0%	2.7%	2.8%	3.4%	3.2%	2.7%	3.4%	2.9%	3.3%	2.8%	3.1%

Table A1.4 - Spinel in garnet peridotite (F8) and dunite (F7) - continued (2)

Section	F7	F8	F8	F8	F8	F8	F8	F8	F8	F8	F8	F8	F8
Assemblage	M2	M2	M2	M2	M2	M2	M2	M2	M2	M2	M2	M2	M2
N°	33	34	35	36	37	38	39	40	41	42	43	44	45
SiO ₂	0.00	0.26	0.42	0.21	0.94	0.27	1.37	0.32	0.26	0.21	0.19	0.26	0.28
TiO ₂	0.05	0.01	0.04	0.00	0.02	0.05	0.00	0.01	0.04	0.03	0.02	0.01	0.04
Al ₂ O ₃	28.43	39.03	35.83	40.87	38.47	36.49	43.39	46.24	42.30	45.51	37.21	41.54	33.47
Cr ₂ O ₃	39.82	28.77	31.93	27.78	29.73	32.01	23.85	22.01	25.68	21.42	28.59	23.45	33.75
Fe ₂ O ₃	2.67	1.71	1.33	1.60	1.20	1.50	0.46	1.82	1.45	2.61	2.10	2.45	2.07
FeO	14.43	11.92	11.91	10.99	11.53	12.01	11.13	9.46	10.42	15.28	18.48	15.97	14.85
MnO	0.59	0.36	0.42	0.37	0.40	0.42	0.30	0.27	0.33	0.43	0.61	0.50	0.49
MgO	13.79	16.75	16.45	17.60	17.79	16.54	18.81	19.35	18.06	15.69	12.28	14.27	14.30
NiO	0.07	0.08	0.05	0.07	0.06	0.03	0.09	0.05	0.06	0.08	0.08	0.07	0.08
ZnO	0.23	0.17	0.21	0.20	0.16	0.24	0.19	0.24	0.19	0.07	0.00	0.02	0.12
VO	0.25	0.12	0.13	0.15	0.13	0.08	0.10	0.09	0.13	0.09	0.11	0.10	0.18
Total	100.33	99.17	98.71	99.85	100.45	99.65	99.70	99.86	98.91	101.40	99.65	98.64	99.62
Mg*	63.0%	71.5%	71.1%	74.1%	73.3%	71.1%	75.1%	78.5%	75.5%	64.7%	54.2%	61.4%	63.2%
Fe ²⁺ *	37.0%	28.5%	28.9%	25.9%	26.7%	28.9%	24.9%	21.5%	24.5%	35.3%	45.8%	38.6%	36.8%
Cr*	48.4%	33.1%	37.4%	31.3%	34.1%	37.0%	26.9%	24.2%	28.9%	24.0%	34.0%	27.5%	40.4%
Fe ³⁺ *	3.0%	1.8%	1.5%	1.7%	1.3%	1.6%	0.5%	1.9%	1.5%	2.7%	2.3%	2.7%	2.3%

Table A1.4 - Spinel in garnet peridotite (F8) and dunite (F7) - continued (3)

Section	F8	F8	F8	F8	F8	F8	F8	F8	F8	F8	F8	F8
Assemblage	M1b (line)	M1b (line)	M1b (line)	M1b (line)	M1b (line)	M1b (line)	M1b (line)	M1b (line)	M1b (line)	M1b (line)	M1b (line)	M1b (line)
N°	46	47	48	49	50	51	52	53	54	55	56	56
SiO ₂	0.02	0.02	0.00	0.01	0.02	0.00	0.02	0.00	0.00	0.02	0.00	0.00
TiO ₂	0.03	0.03	0.02	0.02	0.04	0.01	0.04	0.02	0.02	0.02	0.02	0.04
Al ₂ O ₃	46.57	50.42	50.97	51.26	51.08	50.78	49.18	50.78	51.60	50.84	46.28	46.28
Cr ₂ O ₃	22.44	19.06	18.40	17.96	18.13	18.75	20.34	18.62	17.93	18.67	23.20	23.20
Fe ₂ O ₃	1.65	1.57	1.54	1.45	1.53	1.43	1.44	1.57	1.70	1.50	1.59	1.59
FeO	9.46	8.70	8.72	8.28	8.42	8.77	9.03	8.47	8.27	8.35	9.66	9.66
MnO	0.30	0.25	0.25	0.25	0.29	0.26	0.28	0.27	0.24	0.23	0.33	0.33
MgO	19.00	20.05	20.08	20.28	20.18	19.98	19.64	20.23	20.45	20.30	18.97	18.97
NiO	0.16	0.21	0.20	0.23	0.21	0.20	0.21	0.18	0.27	0.17	0.18	0.18
ZnO	0.31	0.29	0.24	0.26	0.34	0.32	0.36	0.24	0.27	0.34	0.23	0.23
VO	0.18	0.17	0.16	0.16	0.17	0.17	0.17	0.13	0.16	0.16	0.18	0.18
Total	100.10	100.77	100.60	100.15	100.39	100.66	100.71	100.52	100.92	100.61	100.67	100.67
Mg*	0.78	0.80	0.80	0.81	0.81	0.80	0.80	0.81	0.82	0.81	0.78	0.78
Fe ²⁺ *	0.22	0.20	0.20	0.19	0.19	0.20	0.20	0.19	0.18	0.19	0.22	0.22
Cr*	0.24	0.20	0.19	0.19	0.19	0.20	0.22	0.20	0.19	0.20	0.25	0.25
Fe ³⁺ *	0.02	0.02	0.02	0.01	0.02	0.01	0.01	0.02	0.02	0.01	0.02	0.02

Table A1.4 - Spinel in garnet peridotite (F8) and dunite (F7) - continued (4)

Section	F8	F8	F8	F8	F8	F8	F8	F8	F8	F8	F8	F8	F8	F8
Assemblage	M1b (line)	M1b (line)	M1b (line)	M1b (line)	M1b (line)	M1b (line)	M1b (line)	M1b (line)	M1b (core)	M1b (core)	M1b (core)	M1b (rim)	M1b (rim)	M1b (rim)
N°	57	58	59	60	61	62	63	64	65	66	67	68	69	70
SiO2	0.03	0.01	0.00	0.04	0.01	0.02	0.02	0.03	0.04	0.03	0.01	0.02	0.03	0.04
TiO2	0.04	0.03	0.00	0.03	0.03	0.02	0.01	0.03	0.03	0.05	0.02	0.03	0.04	0.15
Al2O3	43.56	48.90	51.03	52.14	52.50	52.28	50.72	45.39	54.49	55.03	51.33	40.52	46.47	40.42
Cr2O3	25.77	20.57	18.51	17.52	16.96	16.88	18.53	23.95	14.50	13.36	16.56	28.46	23.05	28.59
Fe2O3	1.59	1.58	1.59	1.49	1.56	1.64	1.62	1.75	1.83	1.94	2.18	2.09	1.48	1.43
FeO	10.15	8.92	8.51	8.12	7.96	7.88	8.26	9.54	7.77	6.97	7.56	10.58	9.37	10.68
MnO	0.34	0.30	0.25	0.24	0.25	0.25	0.25	0.31	0.20	0.17	0.20	0.40	0.33	0.42
MgO	18.32	19.70	20.22	20.66	20.70	20.61	20.26	18.89	21.12	21.48	20.62	17.63	19.12	17.55
NiO	0.14	0.20	0.21	0.24	0.24	0.25	0.20	0.19	0.29	0.25	0.21	0.20	0.15	0.12
ZnO	0.27	0.30	0.31	0.29	0.33	0.38	0.36	0.31	0.21	0.30	0.19	0.26	0.33	0.31
VO	0.20	0.16	0.14	0.16	0.14	0.17	0.14	0.20	0.15	0.17	0.16	0.20	0.19	0.21
Total	100.40	100.67	100.78	100.92	100.68	100.38	100.36	100.59	100.62	99.76	99.03	100.39	100.55	99.91
Mg*	0.76	0.80	0.81	0.82	0.82	0.82	0.81	0.78	0.83	0.85	0.83	0.75	0.78	0.75
Fe2*	0.24	0.20	0.19	0.18	0.18	0.18	0.19	0.22	0.17	0.15	0.17	0.25	0.22	0.25
Cr*	0.28	0.22	0.20	0.18	0.18	0.18	0.20	0.26	0.15	0.14	0.18	0.32	0.25	0.32
Fe3*	0.02	0.02	0.02	0.01	0.02	0.02	0.02	0.02	0.02	0.02	0.02	0.02	0.01	0.02

Table A1.5 - Amphiboles in garnet peridotite (F8) and dunite (F7)

Section	F8	F8	F8	F8	F8	F8	F8	F8	F8	F8	F8	F8	F8
Assemblage	M2	M2	M2	M2	M2	M2	M2	M2	M2	M2	M2 (in M1 cpx)	M2 (in M1 cpx)	M2 (in M1 cpx)
N°	1	2	3	4	5	6	7	8	9	10	11	12	13
SiO2	44.27	43.95	43.90	43.75	43.63	43.66	44.06	43.69	43.14	43.59	44.34	44.34	43.85
TiO2	1.06	1.04	1.05	1.00	1.91	1.33	1.03	1.20	0.94	0.81	0.99	1.09	1.14
Al2O3	15.08	14.73	14.78	14.92	14.14	14.63	15.16	14.70	13.36	14.05	12.84	12.78	12.84
FeO	2.16	2.25	2.21	2.29	2.36	2.21	2.20	2.17	3.44	3.44	2.78	2.90	2.95
MnO	0.02	0.00	0.01	0.06	0.00	0.03	0.04	0.00	0.09	0.13	0.00	0.05	0.05
MgO	17.33	17.14	17.11	17.06	16.94	17.00	17.44	16.98	17.05	17.30	18.35	18.22	18.27
CaO	11.96	11.90	11.89	11.91	11.75	11.68	11.89	11.90	12.19	12.31	12.06	12.13	11.76
Na2O	2.80	2.67	2.75	2.75	2.82	2.80	2.73	2.61	2.62	2.67	3.16	3.05	3.20
K2O	0.02	0.00	0.02	0.01	0.01	0.03	0.00	0.02	0.03	0.03	0.00	0.00	0.01
total	94.71	93.69	93.73	93.76	93.58	93.37	94.55	93.26	92.85	94.33	94.51	94.55	94.07

Table A1.6 - Garnet line in eclogite (F6)

Section	F6	F6	F6	F6	F6	F6	F6	F6	F6	F6	F6	F6	F6
Assemblage	M1/M2	M1/M2	M1/M2	M1/M2	M1/M2	M1/M2	M1/M2	M1/M2	M1/M2	M1/M2	M1/M2	M1/M2	M1/M2
N°	1	2	3	4	5	6	7	8	9	10	11	12	13
SiO2	41.27	40.88	40.80	41.06	40.98	40.88	40.97	41.07	40.96	40.84	40.78	41.33	41.15
TiO2	0.02	0.02	0.03	0.02	0.04	0.05	0.01	0.03	0.04	0.02	0.02	0.03	0.03
Al2O3	22.66	22.86	22.75	22.89	22.65	22.86	22.77	22.89	22.72	22.74	22.74	22.79	22.75
Cr2O3	0.04	0.09	0.11	0.08	0.11	0.11	0.09	0.10	0.07	0.10	0.07	0.11	0.06
FeO	14.99	12.68	12.59	12.66	12.72	12.74	12.68	12.62	12.64	12.79	12.65	12.73	12.66
MnO	0.40	0.28	0.28	0.28	0.28	0.29	0.31	0.27	0.27	0.30	0.26	0.26	0.27
MgO	12.00	12.89	12.96	12.86	12.97	12.91	13.03	12.96	12.88	12.93	12.63	12.84	12.79
NiO	0.00	0.00	0.00	0.00	0.00	0.00	0.00	0.01	0.00	0.03	0.04	0.02	0.00
CaO	8.92	10.01	10.04	9.89	9.96	9.90	9.68	9.84	9.89	9.91	10.07	9.82	9.88
Total	100.31	99.72	99.56	99.74	99.71	99.74	99.54	99.79	99.48	99.65	99.26	99.94	99.61

Table A1.6 - Garnet line in eclogite (F6) - Continued (1)

Section	F6	F6	F6	F6	F6	F6	F6	F6	F6	F6	F6	F6	F6
Assemblage	M1/M2	M1/M2	M1/M2	M1/M2	M1/M2	M1/M2	M1/M2	M1/M2	M1/M2	M1/M2	M1/M2	M1/M2	M1/M2
N°	14	15	16	17	18	19	20	21	22	23	24	25	25
SiO2	41.05	40.98	41.19	41.14	40.89	40.95	40.96	41.18	40.89	40.63	40.25	40.33	40.33
TiO2	0.03	0.02	0.03	0.02	0.03	0.04	0.02	0.01	0.02	0.02	0.00	0.03	0.03
Al2O3	22.84	22.68	22.76	22.82	22.74	22.87	22.94	22.86	22.62	22.67	22.26	22.62	22.62
Cr2O3	0.10	0.10	0.10	0.06	0.09	0.04	0.10	0.07	0.05	0.09	0.08	0.07	0.07
FeO	12.84	12.91	13.22	12.89	12.87	12.80	12.82	12.67	12.63	13.88	16.41	15.85	15.85
MnO	0.30	0.28	0.30	0.29	0.28	0.26	0.29	0.29	0.29	0.33	0.54	0.42	0.42
MgO	12.77	12.70	12.63	13.01	12.99	12.88	12.99	12.88	12.76	12.29	10.75	11.49	11.49
NiO	0.02	0.00	0.00	0.00	0.00	0.00	0.01	0.00	0.01	0.02	0.03	0.09	0.09
CaO	9.92	9.84	9.64	9.61	9.61	9.75	9.87	9.93	10.15	9.71	9.47	8.68	8.68
Total	99.87	99.53	99.86	99.85	99.50	99.60	100.00	99.89	99.42	99.64	99.80	99.58	99.58

Table A1.7 - Clinopyroxenes, zoisite and dolomite in eclogite (F6)

Section	F6	F6	F6	F6	F6	F6	F6	F6	F6
Assemblage	M2	M2	M2	M2	M2	M2	M2	M2	M2
Phase	Omphacite	Omphacite	Omphacite	Omphacite	Omphacite	Omphacite	Omphacite	zoisite	Dolomite
N°	1	2	3	4	5	6	7	7	8
SiO2	52.12	52.02	52.28	52.13	52.24	51.99	40.56	1.70	1.70
TiO2	0.23	0.23	0.24	0.18	0.15	0.16	0.00	0.01	0.01
Al2O3	7.91	8.07	8.09	7.82	7.98	8.08	30.32	0.24	0.24
Cr2O3	0.12	0.13	0.41	0.12	0.16	0.08	0.02	0.06	0.06
FeO	1.96	2.02	1.70	1.59	1.42	1.82	2.57	1.31	1.31
MnO	0.01	0.02	0.02	0.03	0.02	0.00	0.10	0.13	0.13
MgO	12.99	12.63	12.50	12.84	12.82	12.92	2.89	22.34	22.34
NiO	0.00	0.00	0.02	0.09	0.10	0.00	0.00	0.00	0.00
CaO	20.72	20.11	20.34	20.46	20.95	20.49	15.09	31.36	31.36
Na2O	2.42	2.80	2.73	2.64	2.41	2.62	0.63	0.01	0.01
Totals	98.48	98.03	98.33	97.90	98.25	98.16	92.18	57.17	57.17

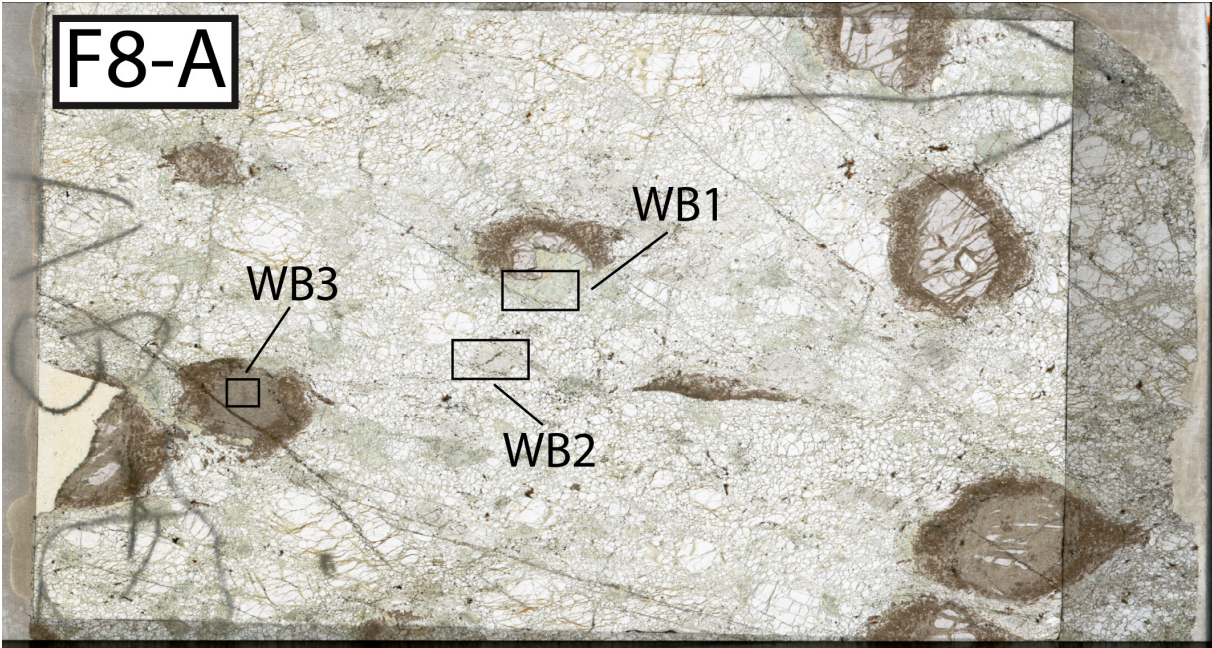


Fig. A1.1 - Thin section F8A. The squares indicate the minerals used for wide beam analyses. WB1: cpx - WB2: opx - WB3: grt.

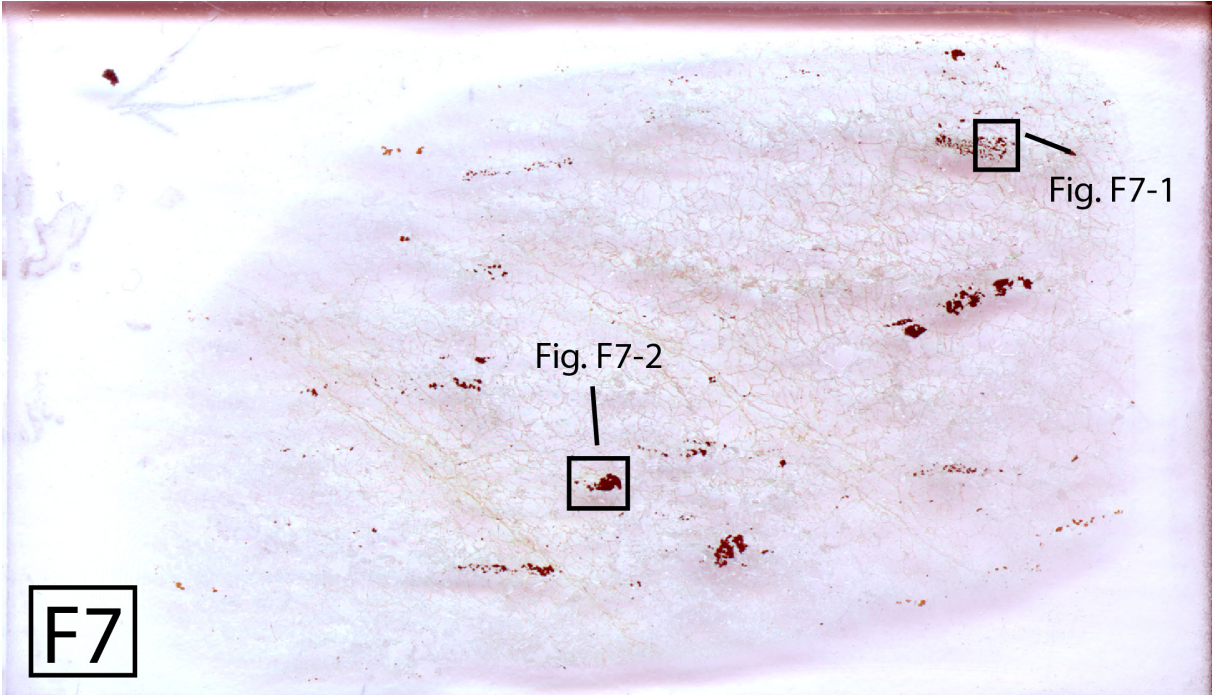


Fig. A1.2 - Thin section F7B. The squares indicate the location of the BS image illustrated below. The name of each picture is in the top-left corner of the BS image.

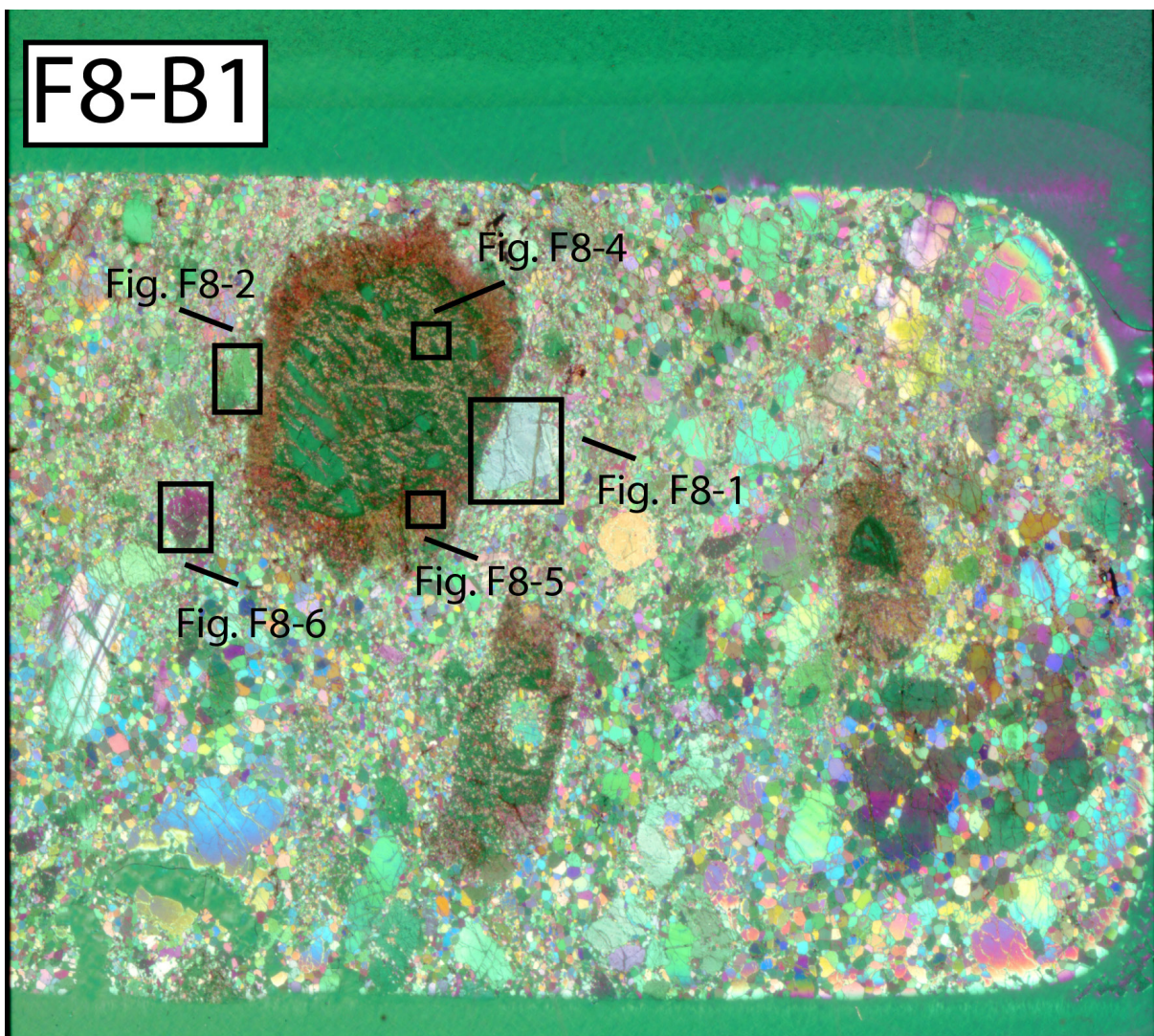
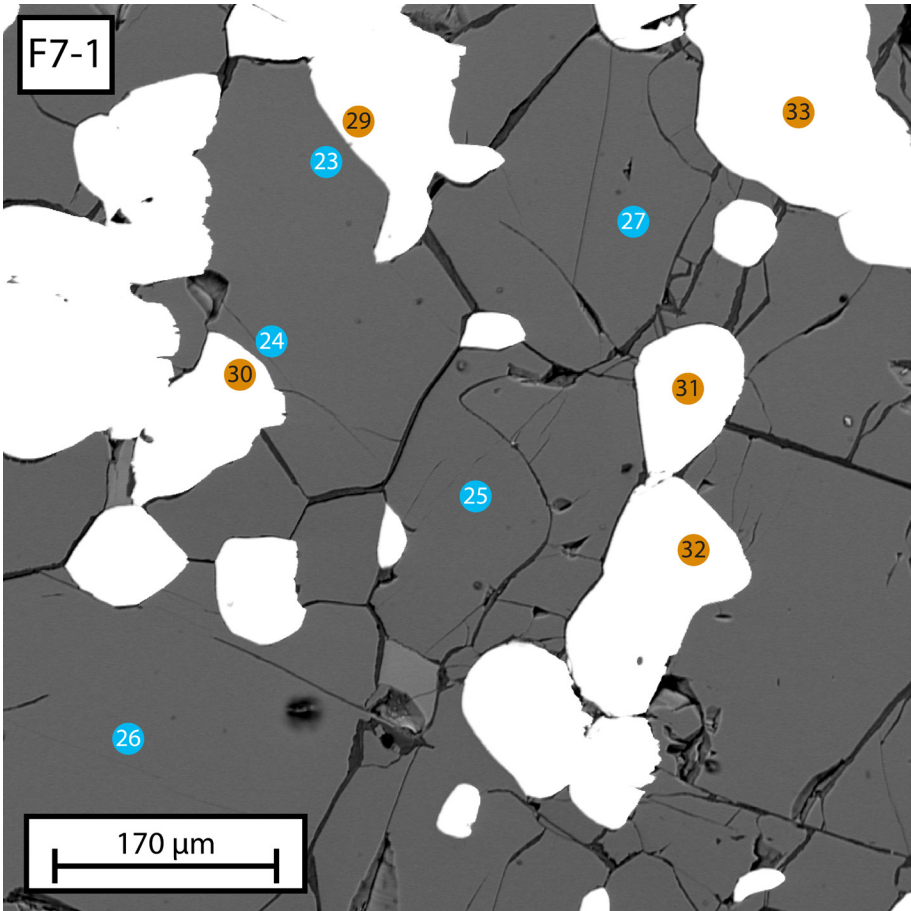
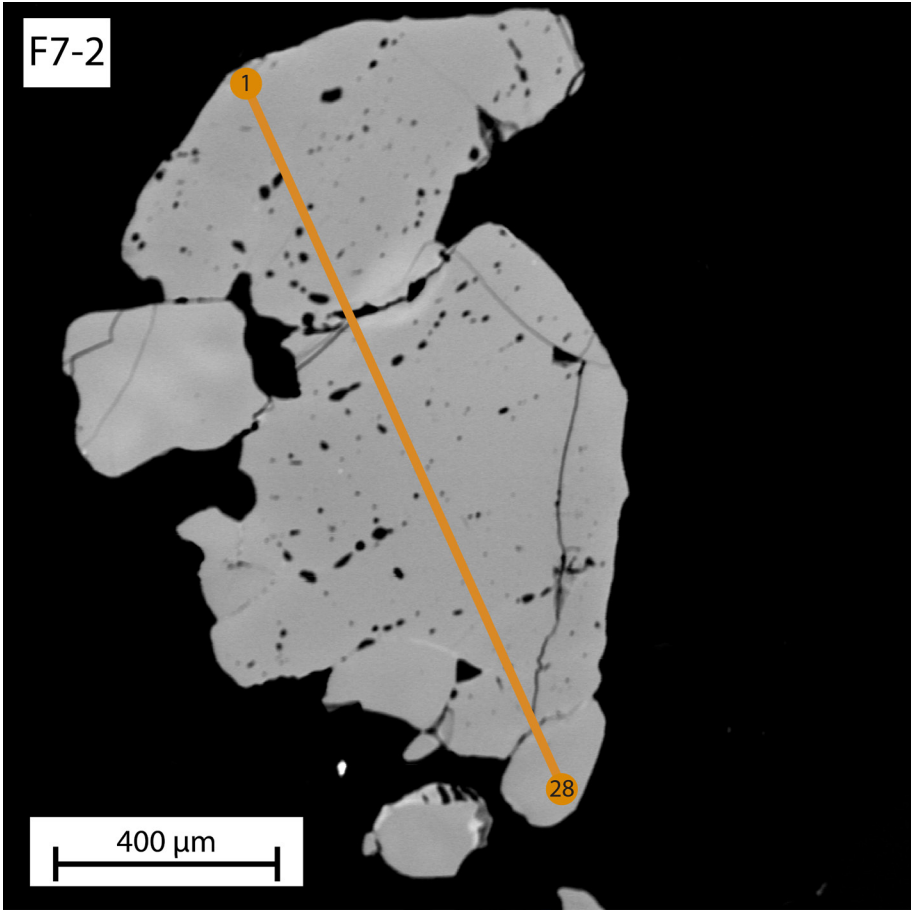
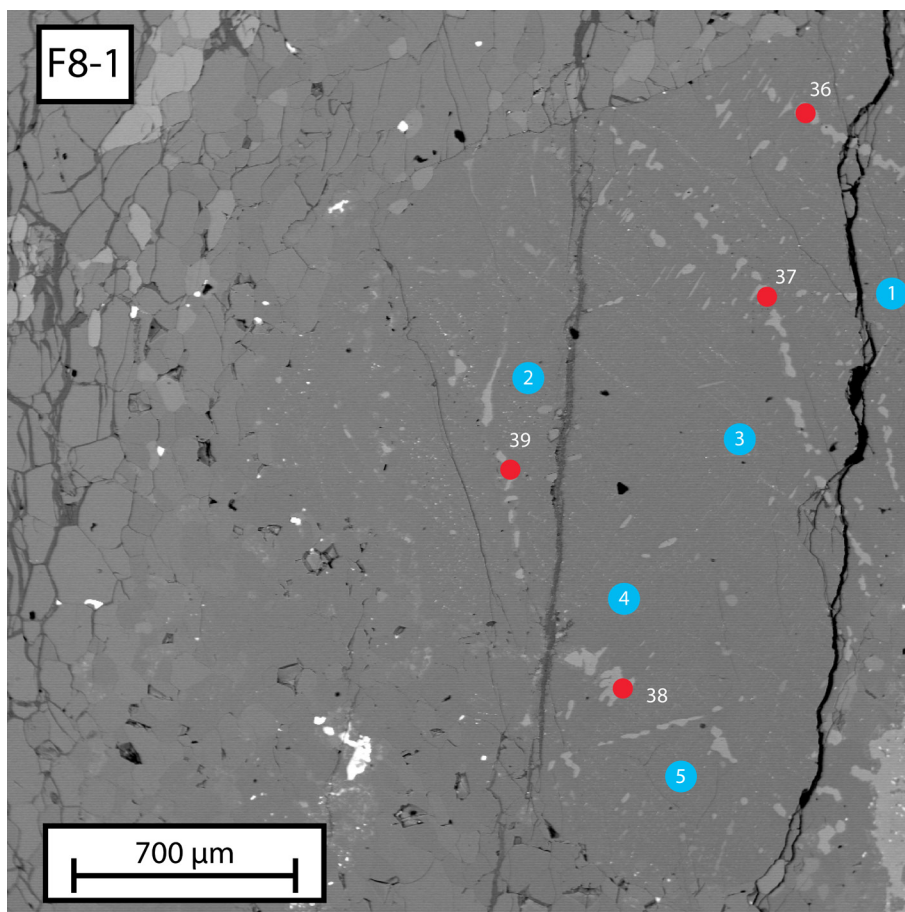


Fig. A1.3 - Thin section F8B-1. The squares indicate the location of the BS image illustrated below. The name of each picture is in the top-left corner of the BS image.

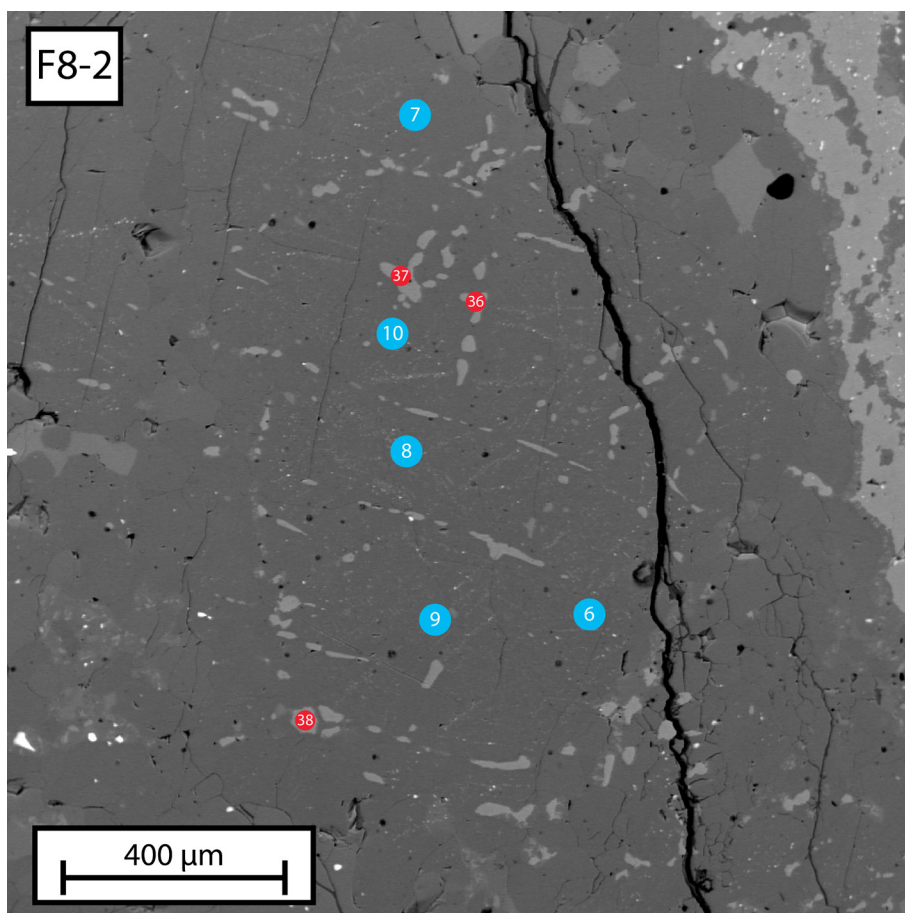


- spl
- am
- opx
- cpx
- grt





- spl
- am
- opx
- cpx
- grt



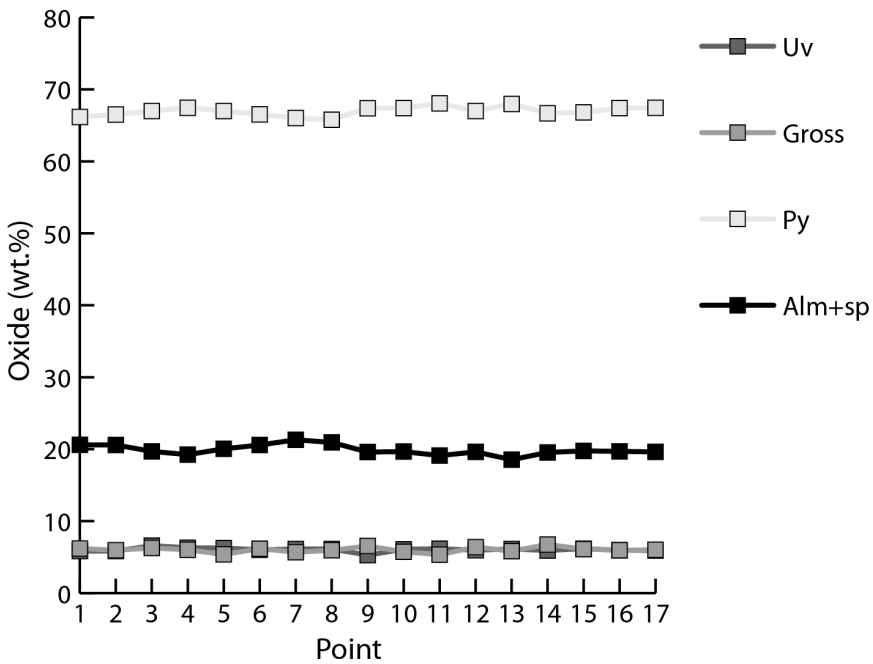
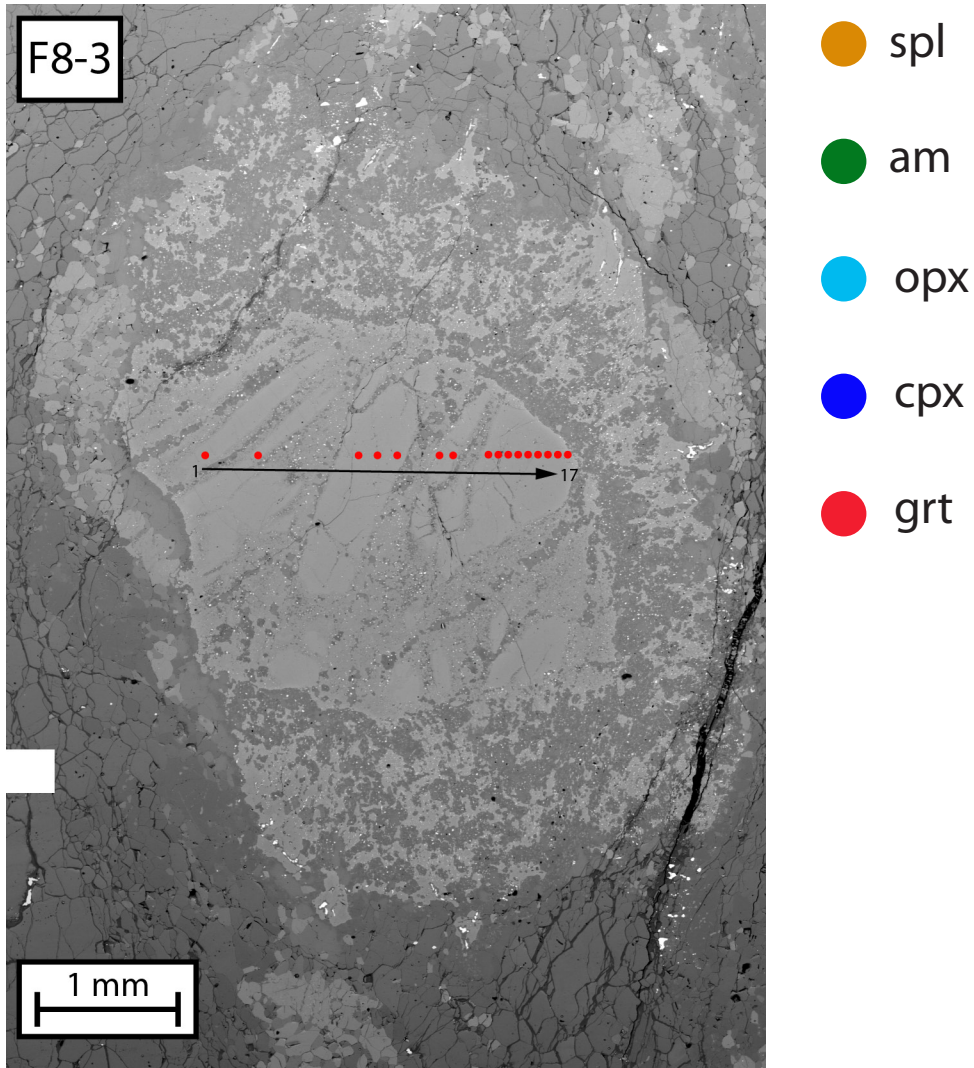
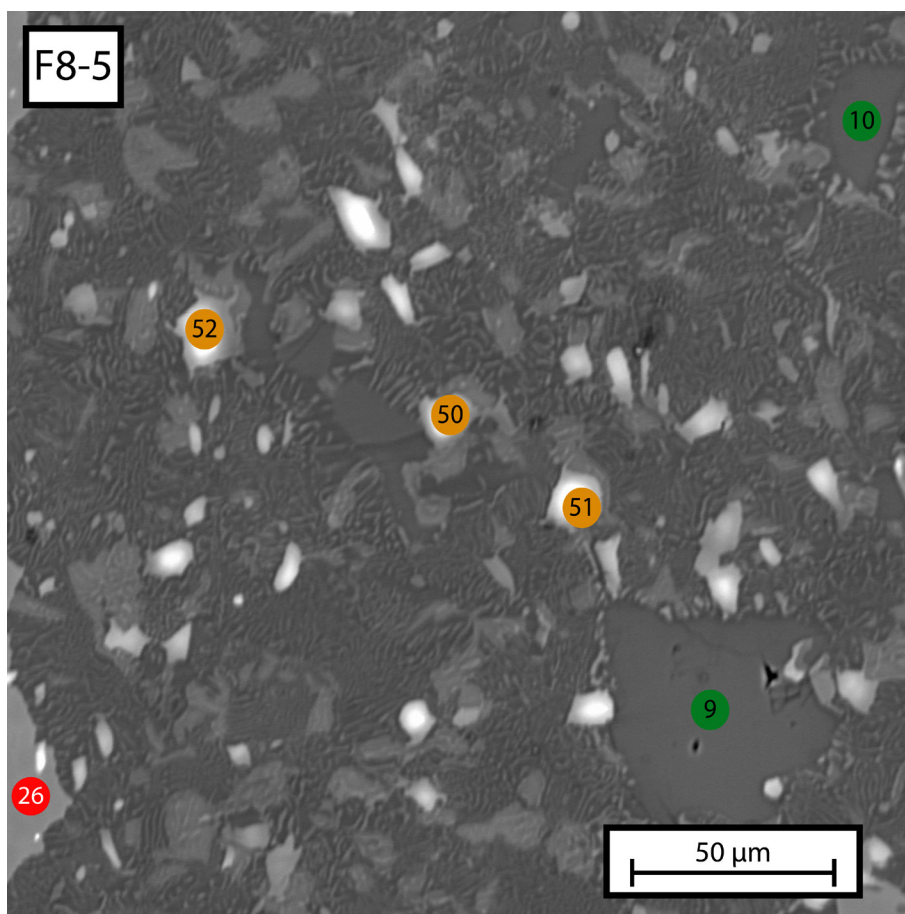
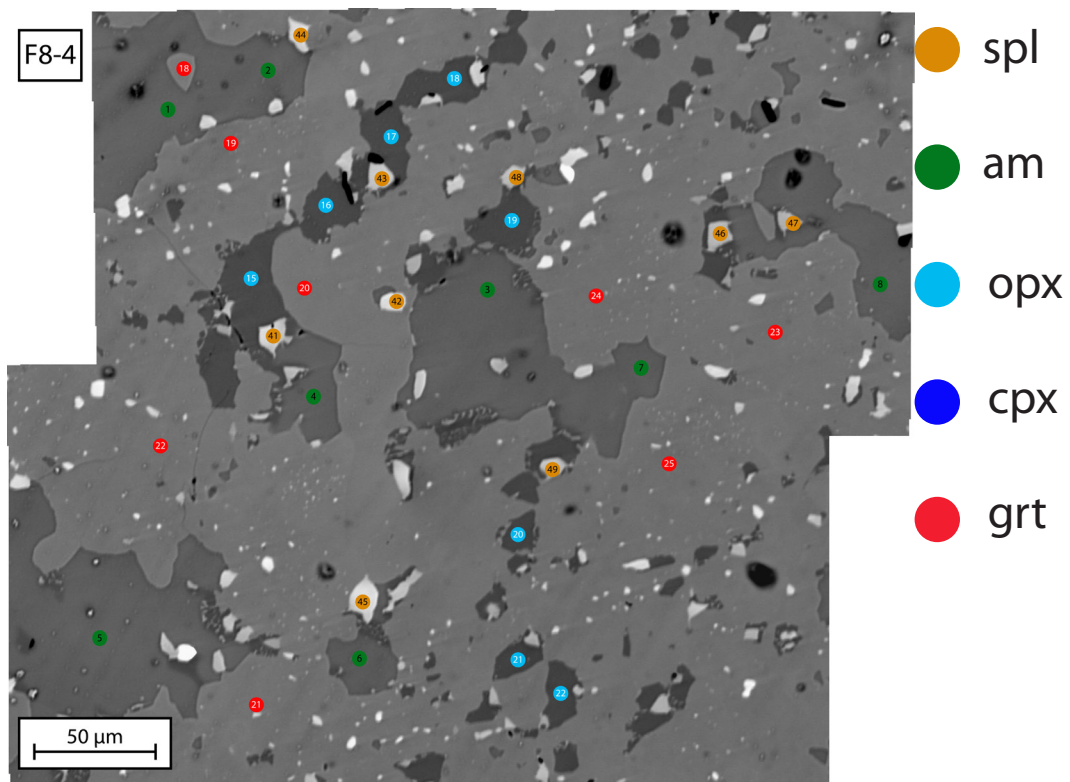
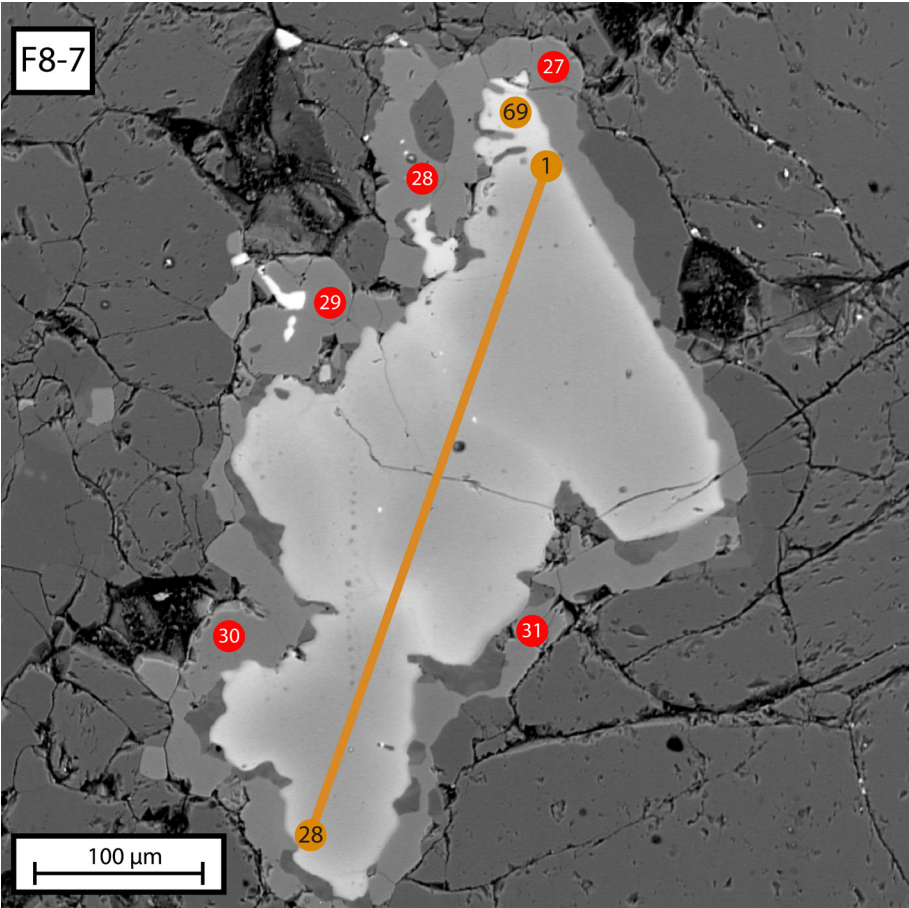
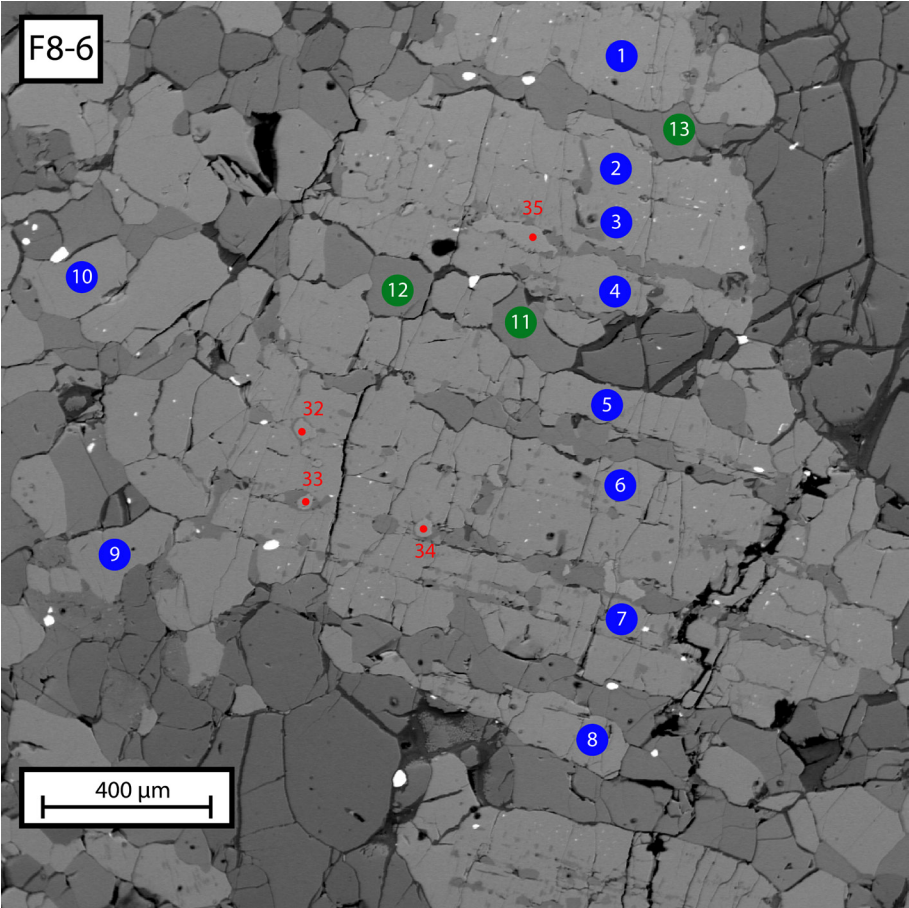
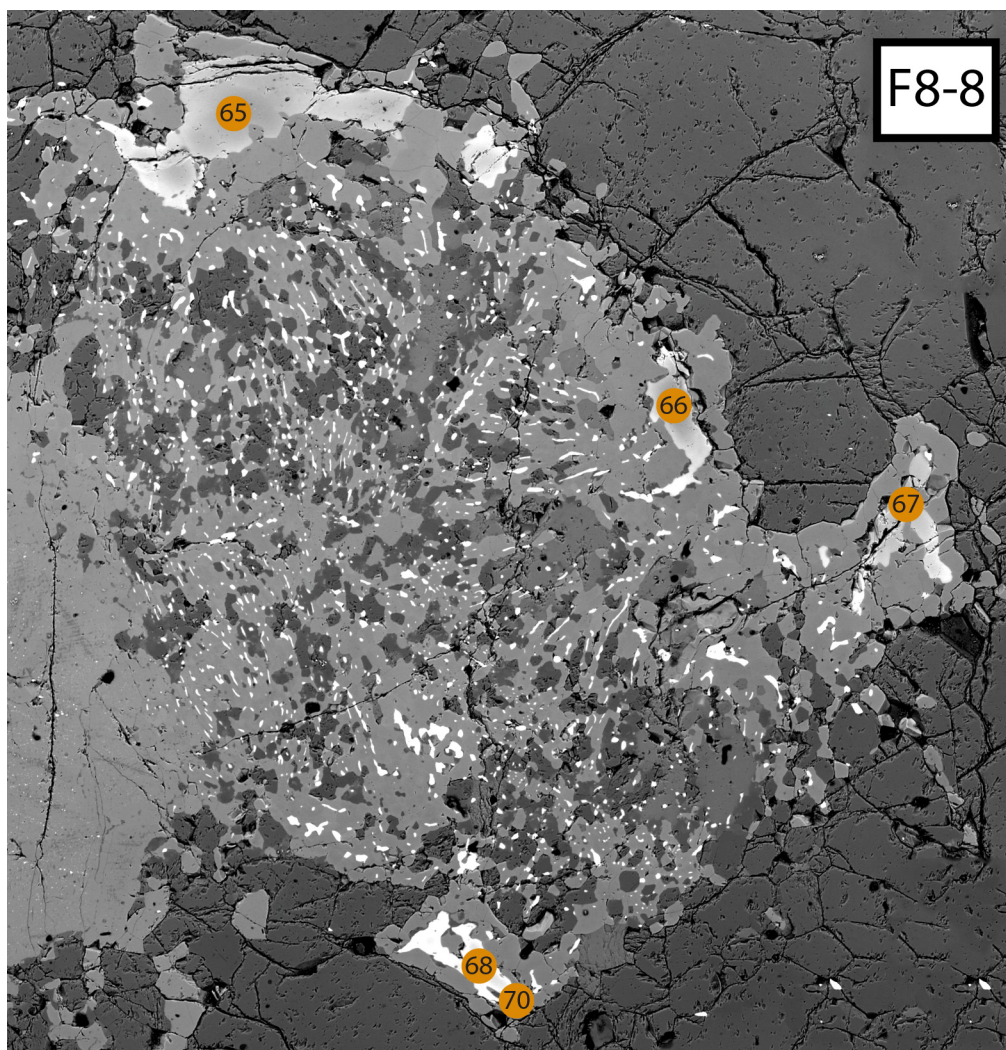


Fig. A1.4 - Line scan of garnet analysis from 1 to 17 (Tab. A1.4).

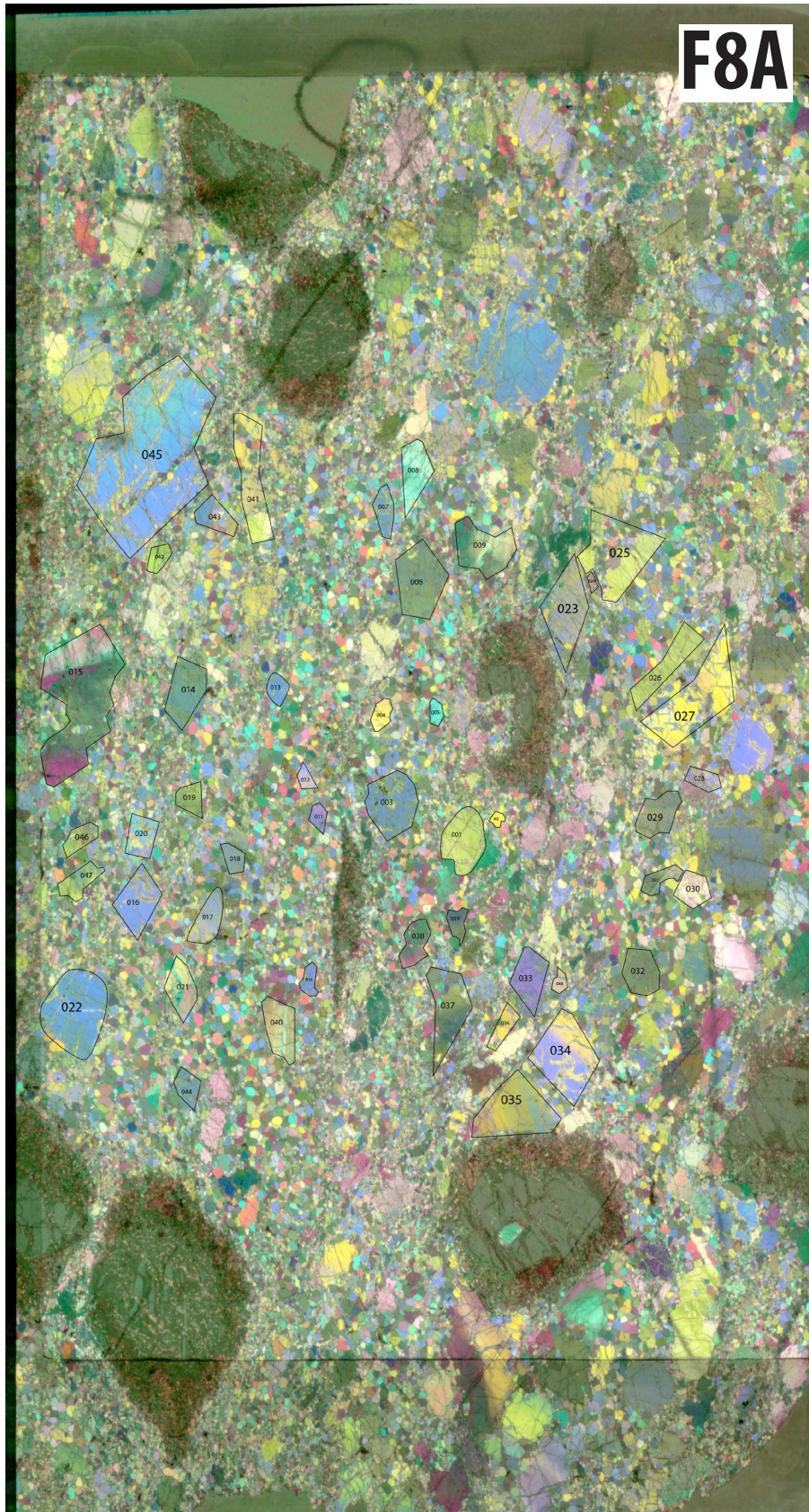






- spl
- am
- opx
- cpx
- grt

APPENDIX 2 - OLIVINE CPO





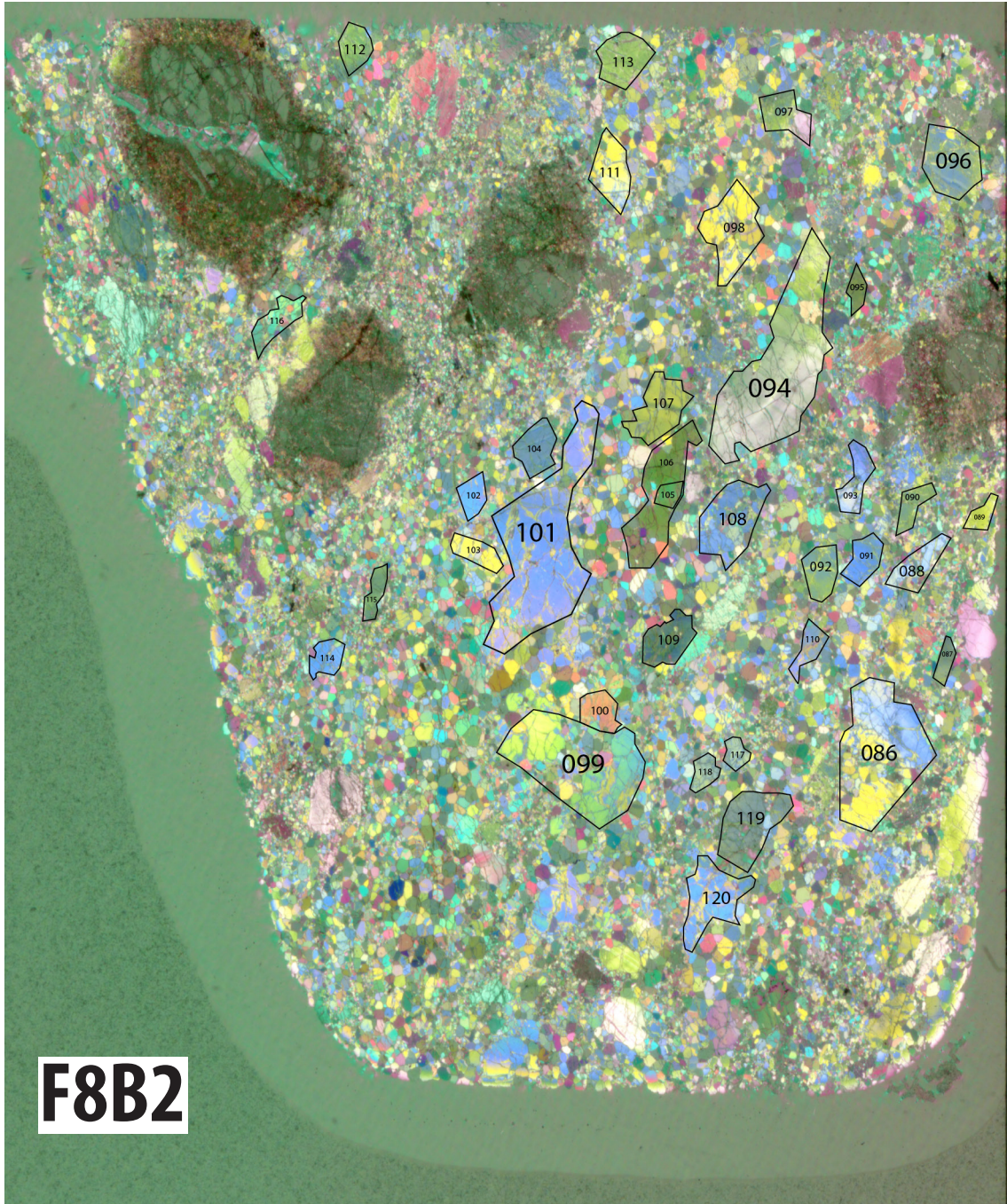


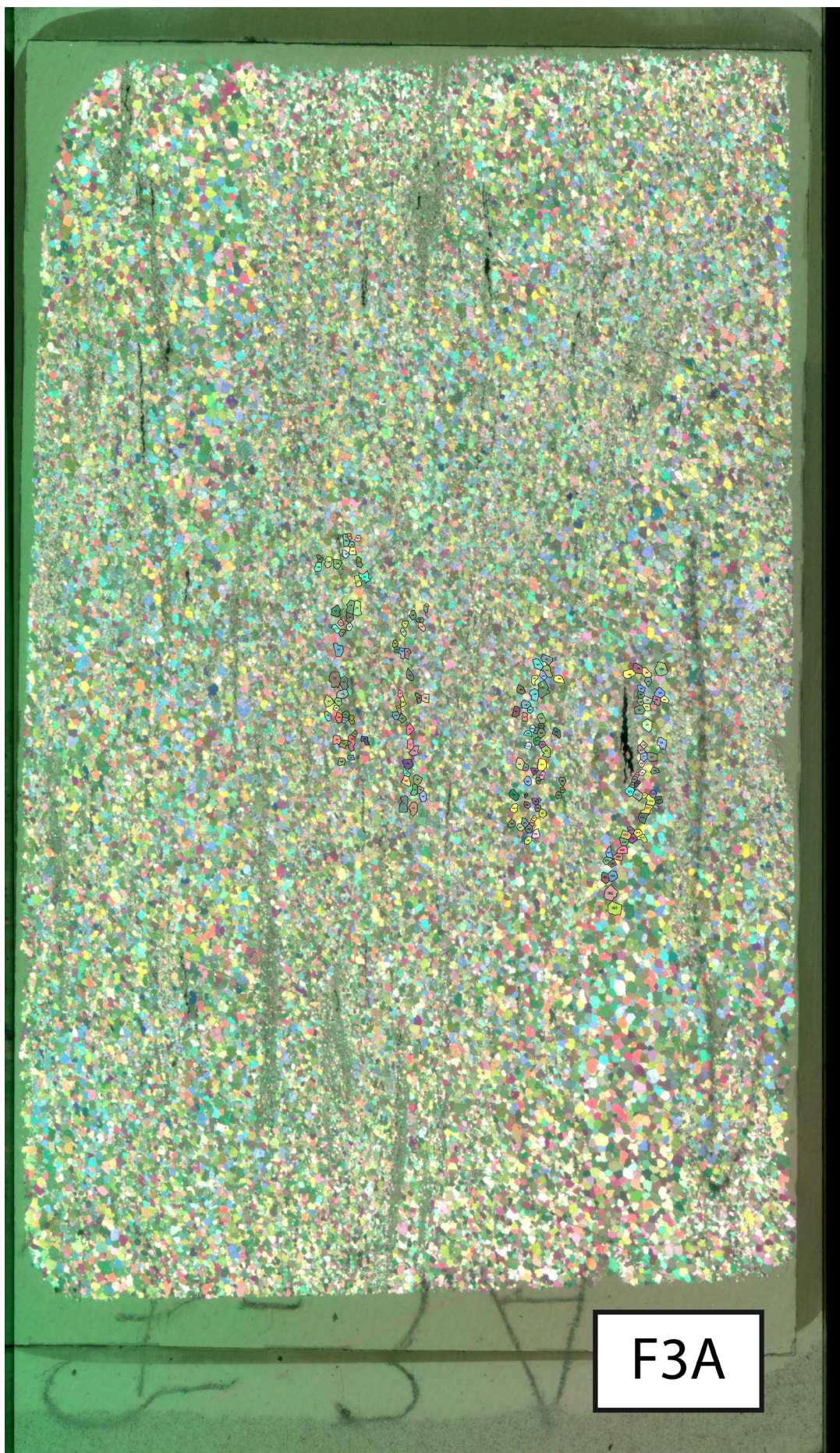
Table A2.1 - Orientation of olivine grains from section F8A, F8B1 and F8B2 (pictures above)

Sample F8				Sample F8				Sample F8			
Grain	α	β	γ	Grain	α	β	γ	Grain	α	β	γ
1	313/35	200/24	358/14	48	115/7	349/2	150/76	95	292/54	226/15	47/14
2	305/30	89/40	330/44	49	311/35	83/53	145/43	96	280/18	160/62	46/15
3	315/49	48/38	290/27	50	324/44	150/35	140/39	97	151/8	300/75	46/9
4	303/19	102/63	263/27	51	171/24	131/50	138/49	98	316/23	36/28	45/22
5	198/3	17/15	256/74	52	180/16	132/51	138/43	99	286/29	20/7	44/17
6	273/41	137/62	252/25	53	262/47	165/7	136/42	100	78/67	301/20	43/0
7	304/27	115/6	248/24	54	94/3	1/35	135/40	101	315/26	36/27	42/4
8	11/64	120/42	240/31	55	115/10	340/76	135/37	102	315/14	35/3	42/13
9	225/15	296/2	229/4	56	320/40	28/36	134/33	103	293/20	28/30	42/10
10	27/21	92/11	228/65	57	330/26	134/61	132/70	104	257/31	240/4	37/5
11	358/22	56/13	227/20	58	314/34	202/28	132/59	105	199/7	99/51	37/0
12	323/12	158/55	226/12	59	291/43	32/4	132/67	106	193/8	255/64	36/25
13	309/27	44/1	224/3	60	244/13	189/36	129/74	107	338/47	254/51	30/29
14	313/46	119/55	222/2	61	321/17	35/33	125/65	108	290/15	48/36	28/40
15	347/5	248/61	221/19	62	303/17	41/14	125/68	109	269/40	150/37	27/17
16	307/2	38/24	221/51	63	316/32	64/27	124/31	110	275/44	7/13	26/8
17	318/37	49/0	220/1	64	312/49	30/28	124/54	111	130/10	18/22	25/14
18	319/42	228/1	220/61	65	306/14	178/62	111/41	112	318/13	163/26	25/17
19	310/38	193/31	218/6	66	327/55	97/32	110/52	113	327/29	71/54	23/17
20	291/21	24/8	218/31	67	291/15	152/70	109/48	114	358/55	93/20	22/24
21	21/53	194/37	216/61	68	280/48	1/26	108/31	115	308/11	164/75	22/44
22	319/42	88/46	214/4	69	283/20	92/68	104/63	116	298/50	126/39	22/10
23	319/35	224/7	213/46	70	287/4	49/80	104/21	117	180/4	146/50	20/20
24	258/77	117/10	212/47	71	305/36	13/31	103/49	118	266/34	203/14	19/9
25	315/16	123/75	212/44	72	267/22	352/1	101/4	119	306/29	199/29	8/24
26	313/36	134/52	211/52	73	43/24	327/55	101/51	120	277/48	79/38	8/3
27	302/21	45/30	208/25	74	299/13	144/75	96/74				
28	120/8	22/44	206/24	75	184/18	265/1	96/45				
29	294/46	88/61	204/55	76	315/47	128/41	90/0				
30	210/55	112/1	204/53	77	315/57	131/30	90/73				
31	328/43	125/43	202/64	78	222/58	144/5	89/39				
32	312/49	130/38	200/42	79	178/15	97/14	85/42				
33	125/6	30/46	199/68	80	315/41	102/50	85/24				
34	298/11	33/24	198/21	81	287/62	126/26	80/35				
35	101/8	8/26	198/22	82	125/26	290/63	79/21				
36	127/4	35/38	197/33	83	316/46	55/2	76/69				
37	260/62	354/2	194/64	84	314/28	137/60	71/50				
38	138/13	260/69	191/64	85	289/28	96/61	71/54				
39	333/46	207/30	190/49	86	299/4	343/13	70/33				
40	171/12	129/38	184/42	87	292/50	301/15	66/45				
41	317/32	109/59	181/62	88	323/19	52/28	62/53				
42	304/39	38/13	179/67	89	302/22	150/64	58/4				
43	143/6	2/31	176/50	90	290/31	131/57	54/7				
44	308/42	44/10	175/34	91	306/30	82/58	54/5				
45	320/20	34/33	166/47	92	299/38	96/52	51/26				
46	139/2	216/65	154/45	93	313/7	6/28	51/55				
47	318/7	195/59	152/30	94	325/25	152/59	51/32				



Table A2.2 - Orientation of olivine grains from section F7A (picture above)

Sample F7				Sample F7				Sample F7				Sample F7			
Grain	α	β	γ	Grain	α	β	γ	Grain	α	β	γ	Grain	α	β	γ
1	166/0	0/90	256/0	51	249/25	54/64	159/7	101	77/29	245/60	347/7	151	346/16	219/64	76/21
2	4/18	129/60	274/25	52	172/15	28/71	262/11	102	334/25	177/63	64/11	152	343/20	253/16	125/65
3	286/22	141/63	16/16	53	316/14	84/67	226/18	103	352/19	206/67	82/13	153	96/3	186/14	354/76
4	18/20	288/8	302/37	54	138/24	274/57	48/23	104	221/3	315/55	131/35	154	344/30	181/59	74/10
5	2/17	143/68	272/14	55	24/8	114/25	277/64	105	321/13	92/70	231/15	155	194/65	336/20	66/16
6	235/15	55/75	145/0	56	340/10	87/59	249/30	106	19/75	157/11	247/10	156	22/65	227/23	137/11
7	315/18	173/67	45/14	57	18/18	108/5	213/71	107	244/34	64/56	154/0	157	178/9	313/77	88/9
8	191/3	290/72	101/18	58	288/5	198/24	106/32	108	64/14	244/76	154/0	158	75/22	310/53	165/30
9	195/10	295/44	107/45	59	168/40	340/49	78/7	109	15/1	284/56	105/34	159	146/8	251/61	56/28
10	235/20	27/67	145/11	60	132/37	301/52	42/8	110	312/11	152/78	42/4	160	6/34	217/50	96/22
11	297/30	114/60	207/2	61	315/40	120/48	225/13	111	327/15	87/61	237/25	161	357/19	202/69	87/9
12	37/7	162/78	307/10	62	340/16	70/16	124/14	112	332/25	198/55	62/26	162	125/20	253/58	35/25
13	10/14	228/72	100/11	63	14/8	104/27	288/40	113	164/19	350/71	254/2	163	40/19	237/70	130/6
14	281/11	149/74	11/12	64	239/7	43/83	149/2	114	18/15	136/59	288/27	164	170/8	299/77	80/10
15	51/20	228/70	321/1	65	12/17	260/50	102/37	115	78/17	193/53	348/33	165	120/28	266/56	30/20
16	49/25	270/57	139/22	66	309/7	88/81	219/6	116	328/18	58/21	16/23	166	101/28	238/53	11/26
17	332/24	148/66	242/2	67	10/9	267/54	100/35	117	341/32	155/58	251/4	167	222/25	312/16	74/61
18	130/29	315/61	220/3	68	120/9	18/52	210/37	118	28/4	282/75	118/14	168	357/11	267/38	101/51
19	22/31	112/4	102/38	69	278/23	57/60	188/20	119	360/5	122/6	32/12	169	42/20	312/31	163/54
20	50/37	252/50	140/17	70	135/30	315/60	225/0	120	15/4	285/25	124/12	170	112/28	275/61	22/9
21	343/16	253/15	52/13	71	163/11	41/70	253/17	121	313/10	107/79	223/5	171	171/5	290/80	81/9
22	22/5	112/0	202/85	72	22/21	248/38	158/7	122	27/28	241/56	117/20	172	331/8	70/47	241/42
23	202/1	112/0	104/0	73	264/15	354/2	262/5	123	321/15	193/66	51/19	173	145/9	259/68	55/20
24	334/10	64/18	216/69	74	344/18	126/67	254/14	124	4/5	110/72	274/17	174	150/17	287/67	60/16
25	1/30	271/3	176/60	75	111/3	4/80	201/10	125	87/81	285/9	195/3	175	337/9	101/74	247/13
26	194/20	320/5	50/17	76	28/29	241/56	122/18	126	10/30	152/52	280/24	176	87/7	189/60	357/29
27	210/11	152/20	242/7	77	348/10	258/0	168/80	127	10/40	280/14	173/48	177	7/66	104/3	194/24
28	354/12	98/49	264/40	78	198/6	58/82	288/5	128	159/16	289/65	69/19	178	35/24	305/11	191/64
29	236/9	8/77	146/10	79	295/10	25/22	332/30	129	168/1	78/25	260/65	179	68/15	183/57	338/30
30	12/10	102/6	320/27	80	348/17	129/68	258/14	130	96/17	308/70	186/11	180	328/31	238/0	148/59
31	340/14	104/66	250/20	81	61/15	220/74	331/6	131	326/17	84/56	236/30	181	217/58	315/5	45/32
32	292/19	171/55	22/30	82	257/7	66/7	156/8	132	122/42	314/47	212/11	182	316/61	151/28	61/8
33	165/7	75/6	327/38	83	27/7	281/66	117/23	133	324/27	148/63	54/2	183	5/16	156/72	275/9
34	325/14	55/11	309/18	84	138/24	279/59	48/20	134	36/14	155/62	306/24	184	53/25	258/62	143/12
35	324/16	234/9	326/21	85	123/0	213/25	33/65	135	357/13	267/11	137/73	185	323/14	98/70	233/14
36	354/20	223/60	84/23	86	208/23	60/63	298/15	136	78/78	223/10	313/7	186	9/31	279/19	159/54
37	157/5	260/68	67/21	87	338/3	82/78	248/12	137	129/35	262/44	19/25	187	32/60	140/10	230/28
38	329/30	117/54	239/20	88	189/15	50/70	279/13	138	346/27	185/61	76/10	188	218/17	81/67	308/16
39	324/16	54/15	89/24	89	327/7	70/61	237/28	139	85/5	341/70	175/19	189	288/61	179/10	89/27
40	200/24	290/2	360/38	90	194/2	293/76	108/13	140	202/0	112/14	292/76	190	348/27	149/61	258/10
41	25/7	275/70	115/19	91	9/42	199/47	99/9	141	285/29	107/61	15/1	191	308/11	83/74	218/11
42	163/7	313/82	73/4	92	341/4	71/29	244/61	142	317/7	219/49	47/40	192	357/23	87/21	219/59
43	334/5	110/83	245/5	93	351/14	119/67	261/18	143	89/81	304/7	214/5	193	90/0	0/90	180/27
44	130/16	310/74	220/0	94	104/10	349/67	194/21	144	48/15	318/24	169/62	194	180/0	270/37	90/53
45	83/8	353/2	121/1	95	37/20	307/9	86/32	145	14/45	282/2	192/45	195	275/32	5/2	98/58
46	357/28	87/7	190/61	96	19/19	143/57	289/27	146	347/5	257/6	117/82	196	300/13	67/69	210/17
47	135/3	229/50	45/40	97	162/3	70/25	312/33	147	146/61	263/14	353/26	197	206/5	110/51	296/39
48	165/0	255/19	327/35	98	4/24	213/62	94/14	148	5/28	185/62	95/0	198	169/24	259/9	9/64
49	297/9	181/70	27/18	99	20/3	225/3	135/9	149	202/17	22/73	112/0	199	208/15	118/3	17/75
50	30/14	210/76	120/0	100	315/10	45/9	177/77	150	295/1	203/63	25/27	200	22/8	141/74	292/14



F3A

Table A2.2 - Orientation of olivine grains from section F3A (picture above)

Sample F3				Sample F3				Sample F3				Sample F3			
Grain	α	β	γ	Grain	α	β	γ	Grain	α	β	γ	Grain	α	β	γ
1	74/63	196/15	286/23	51	313/58	190/18	100/27	101	320/4	185/84	50/4	151	297/27	207/21	80/56
2	58/28	229/62	326/4	52	359/52	126/24	216/31	102	239/30	23/53	149/23	152	141/19	312/71	51/3
3	178/60	81/4	351/30	53	53/12	170/64	323/23	103	122/23	339/61	212/18	153	207/71	355/16	85/10
4	14/84	225/5	135/3	54	210/30	47/59	300/10	104	317/15	227/8	109/73	154	85/70	201/9	291/18
5	87/66	249/23	339/8	55	43/19	223/71	133/0	105	198/15	108/27	316/59	155	150/4	270/82	60/7
6	90/16	296/72	180/8	56	30/3	128/70	300/20	106	246/53	17/25	107/28	156	153/71	25/12	295/15
7	6/68	210/20	120/9	57	94/21	184/9	296/67	107	264/0	354/13	174/77	157	302/15	70/66	212/19
8	176/73	283/5	13/16	58	235/63	113/15	23/23	108	311/3	198/82	41/7	158	222/20	28/69	132/5
9	318/7	183/80	48/7	59	198/59	76/17	346/26	109	41/10	227/80	131/1	159	210/70	79/13	349/15
10	30/55	120/0	210/35	60	54/74	284/10	194/12	110	101/67	2/4	272/23	160	356/21	120/54	266/30
11	100/20	264/69	10/6	61	103/67	319/19	229/14	111	172/29	4/60	262/7	161	156/11	262/54	66/35
12	338/15	143/74	248/4	62	73/63	243/25	163/0	112	188/23	59/54	278/28	162	44/2	303/80	134/10
13	59/67	246/23	156/3	63	247/48	139/15	49/40	113	90/79	315/8	45/8	163	148/13	238/8	359/75
14	200/16	30/74	290/3	64	356/30	266/23	140/53	114	324/55	234/0	144/35	164	241/28	67/62	331/3
15	192/15	282/3	23/75	65	195/59	76/16	346/27	115	20/3	182/87	290/1	165	311/30	102/55	221/18
16	172/25	341/65	82/5	66	57/73	214/16	304/7	116	78/20	296/65	168/16	166	188/25	19/65	278/5
17	47/17	214/73	317/4	67	149/20	353/68	239/9	117	72/5	188/79	342/10	167	121/22	327/66	211/11
18	214/18	124/4	22/72	68	119/72	308/18	218/3	118	227/66	33/23	123/6	168	34/69	179/17	269/12
19	167/5	265/59	77/31	69	357/9	211/79	87/6	119	310/24	99/62	220/15	169	64/13	261/76	154/4
20	275/74	55/12	145/10	70	349/18	226/58	79/27	120	162/18	319/70	72/8	170	67/79	179/4	269/10
21	29/2	125/71	299/19	71	250/17	160/2	63/73	121	158/55	298/27	28/23				
22	191/2	284/58	101/32	72	209/66	33/24	303/2	122	192/0	102/84	282/6				
23	319/5	217/67	49/22	73	333/23	151/67	243/1	123	347/18	257/3	158/72				
24	94/16	284/74	184/3	74	9/22	279/8	170/67	124	359/18	89/7	200/71				
25	350/21	148/67	260/9	75	196/25	27/65	286/5	125	167/70	7/19	277/7				
26	145/60	270/18	360/25	76	49/1	145/81	319/9	126	273/28	108/61	3/8				
27	295/9	97/81	205/3	77	13/3	283/16	113/74	127	190/3	285/57	100/33				
28	34/60	207/30	297/4	78	154/6	47/70	244/19	128	132/20	293/69	42/7				
29	211/5	95/79	301/10	79	118/2	343/87	207/2	129	152/11	322/79	62/2				
30	179/3	44/86	269/3	80	254/74	358/4	88/16	130	160/79	288/7	18/9				
31	60/81	220/8	310/3	81	162/0	72/67	252/23	131	243/14	153/7	37/74				
32	358/6	248/73	88/16	82	208/2	118/26	302/64	132	10/5	151/84	280/4				
33	100/3	333/85	190/4	83	167/2	70/75	257/15	133	163/3	53/81	253/8				
34	197/3	298/75	107/15	84	178/10	65/65	268/23	134	341/25	140/63	251/10				
35	210/12	120/26	324/62	85	176/8	281/62	86/27	135	181/3	82/72	271/18				
36	157/55	306/30	36/19	86	126/55	245/18	335/30	136	36/61	147/11	237/27				
37	217/27	307/24	78/54	87	2/73	214/14	124/9	137	156/83	336/7	246/0				
38	196/26	106/5	6/64	88	247/30	67/60	157/0	138	60/75	307/6	217/14				
39	182/28	272/1	4/62	89	163/18	253/14	21/67	139	2/2	92/26	268/64				
40	152/25	242/3	338/65	90	222/69	353/14	83/16	140	359/2	264/69	89/21				
41	204/17	81/60	294/25	91	28/10	298/6	177/78	141	242/87	62/3	152/0				
42	221/9	131/12	348/75	92	194/4	93/70	284/20	142	319/60	90/20	180/23				
43	190/11	280/25	77/63	93	172/6	32/82	262/5	143	333/65	147/25	237/3				
44	180/69	69/8	339/20	94	168/20	78/17	308/64	144	25/86	142/2	232/4				
45	197/1	101/80	287/10	95	104/24	284/66	194/0	145	247/58	37/28	127/17				
46	151/28	340/62	241/5	96	79/78	193/5	284/11	146	47/20	275/61	137/22				
47	127/32	341/51	217/23	97	22/15	146/64	283/19	147	323/68	133/22	223/4				
48	200/56	316/16	46/30	98	121/13	31/19	245/67	148	360/17	183/73	90/1				
49	26/34	238/50	116/23	99	28/30	138/0	228/54	149	163/18	320/70	73/8				
50	193/5	35/85	283/2	100	193/15	323/67	103/18	150	58/29	243/61	148/3				